

AFRL-AFOSR-UK-TR-2021-0005

Investigation of Energetic Particles in the Sun and Heliosphere at Different Phases of Solar Activity

Valentina Zharkova
Northumbria University
230 W 41ST STREET FL 7
NEW YORK, NY, NE1 8ST
US

03/19/2021
Final Technical Report

DISTRIBUTION A: Distribution approved for public release.

Air Force Research Laboratory
Air Force Office of Scientific Research
European Office of Aerospace Research and Development
Unit 4515 Box 14, APO AE 09421

REPORT DOCUMENTATION PAGE

Form Approved
OMB No. 0704-0188

The public reporting burden for this collection of information is estimated to average 1 hour per response, including the time for reviewing instructions, searching existing data sources, gathering and maintaining the data needed, and completing and reviewing the collection of information. Send comments regarding this burden estimate or any other aspect of this collection of information, including suggestions for reducing the burden, to Department of Defense, Washington Headquarters Services, Directorate for Information Operations and Reports (0704-0188), 1215 Jefferson Davis Highway, Suite 1204, Arlington, VA 22202-4302. Respondents should be aware that notwithstanding any other provision of law, no person shall be subject to any penalty for failing to comply with a collection of information if it does not display a currently valid OMB control number.
PLEASE DO NOT RETURN YOUR FORM TO THE ABOVE ADDRESS.

1. REPORT DATE *(DD-MM-YYYY)*	**2. REPORT TYPE**	**3. DATES COVERED** *(From - To)*
19-03-2021	Final	01 Jun 2017 - 31 Oct 2020

4. TITLE AND SUBTITLE
Investigation of Energetic Particles in the Sun and Heliosphere at Different Phases of Solar Activity

5a. CONTRACT NUMBER

5b. GRANT NUMBER
FA9550-17-1-0139

5c. PROGRAM ELEMENT NUMBER

6. AUTHOR(S)
Valentina Zharkova

5d. PROJECT NUMBER

5e. TASK NUMBER

5f. WORK UNIT NUMBER

7. PERFORMING ORGANIZATION NAME(S) AND ADDRESS(ES)
Northumbria University
230 W 41ST STREET FL 7
NEW YORK, NY NE1 8ST
US

8. PERFORMING ORGANIZATION REPORT NUMBER

9. SPONSORING/MONITORING AGENCY NAME(S) AND ADDRESS(ES)
EOARD
UNIT 4515
APO AE 09421-4515

10. SPONSOR/MONITOR'S ACRONYM(S)
AFRL/AFOSR IOE

11. SPONSOR/MONITOR'S REPORT NUMBER(S)
AFRL-AFOSR-UK-TR-2021-0005

12. DISTRIBUTION/AVAILABILITY STATEMENT
A Distribution Unlimited: PB Public Release

13. SUPPLEMENTARY NOTES

14. ABSTRACT
Final Report

15. SUBJECT TERMS

16. SECURITY CLASSIFICATION OF:			**17. LIMITATION OF ABSTRACT**	**18. NUMBER OF PAGES**	**19a. NAME OF RESPONSIBLE PERSON**
a. REPORT	**b. ABSTRACT**	**c. THIS PAGE**			BARRETT FLAKE
U	U	U	SAR	87	**19b. TELEPHONE NUMBER** *(Include area code)* 314 235 6115

Final report
of the project 16IOE055
Investigation of energetic particles in the Sun and heliosphere at different phases of solar activity
for the period of 1 June 2017- 31 October 2020

Supervised by PI Prof. V.V. Zharkova,
Department of Mathematics, Physics and Electrical Engineering
Northumbria University
NE1 8ST
United Kingdom

Table of contents **Pages**

1. General information 4

1.1. Summary 4

1.2. Project significance 4

1.3. Project objectives 5

2. Introduction 5

2.1. Current sheets as primary energy release sites in the Sun and heliosphere 5

2.2. Simulations of particle acceleration during magnetic reconnection 7

2.3. Transport effects of energetic particles in the solar atmosphere 9

3. Methods, assumptions and procedures 11

3.1. Investigation of particle acceleration in reconnecting current sheets 11

3.2. Investigation of particle and energy transport in flaring loops 15

3.3. Radiative transfer of Hydrogen emission (code HYDRO2GEN) 17

3.4. Generation of seismic emission in the solar interior 19

4. Results and Discussion 21

4.1. Accelerated particles in 3D RCS with single X-nullpoint – TP approach 21

DISTRIBUTION A: Distribution approved for public release. Distribution unlimited

4.1.1. Particle separation effect 21

4.1.2. Transit and bounced particles of the same charge 21

4.2. Acceleration in coalescent and squashed islands - test particle approach 22

4.2.1. Particle trajectories 22

4.1.2. Energy spectra 23

4.3. Acceleration in coronal mass ejections in breakout models – TP approach 24

4.4. Acceleration of particle in magnetic islands – PIC approach 27

4.4.1. Separation of protons from electrons 27

4.4.2. Transit vs bounced particles of the same charge 28

4.4.3. Current sheets with magnetic islands – PIC approach 29

4.4.4. Coalescent magnetic islands 29

4.4.5. Squashed magnetic islands 31

4.4.6. Energy gains in magnetic islands 32

4.5. Generation of turbulence by accelerated particles in current sheets 33

4.5.1. Single X-nullpoint 33

4.5.2. Multiple X and O-nullpoints 34

4.5.3. Phase space distributions 36

4.5.4. Frequency analysis 37

4.5.5. Summary 39

4.6. Pitch angle distributions of accelerated particles probed by observations 39

4.6.1. PIC simulations of PADs in different crossings of RCSs 39

4.6.2. Multi-satellites observations of solar wind particles 41

4.6.3. Further PAD predictions in CSs with a single X-nullpoint 44

4.6.4. Interpretation of observed PAD features in MIs 46

4.7. Particle transport models and their comparison with observations 51

DISTRIBUTION A: Distribution approved for public release. Distribution unlimited

4.7.1. General introduction 51

4.7.2. Observations of the X2.1 flare of 6 September 2011 53

4.7.3. Observations of the X9.3 flare of 6 September 2017 57

4.7.4. Hydrodynamic models of flaring atmospheres 66

4.7.5. Shock propagation in the solar interior 68

4.7.6. Interpretation of the EUV, H-alpha and WL emission 70

4.7.7. Interpretation of seismic emission with the shocks 74

4.7.8. General conclusions on energy/particle transport 76

5. Conclusions 78

6. References 81

7. Dissemination of the results 85

8. List of figures 86

9. List of tables 87

DISTRIBUTION A: Distribution approved for public release. Distribution unlimited

General information

1. 1. Summary

flares, eruption of fast coronal mass ejections (CMEs) and reacceleration in the solar wind. The scenario of particle acceleration and parameters gained by these energetic particles (energy spectra, pitch angle distributions) and links to magnetic field topologies where they were energized. These characteristics are of a great interest for many researchers and space industry as they define space weather in the heliosphere. These energetic particles reveal very peculiar distributions in velocities and pitch angles not anticipated by regular models of stochastic particle acceleration by turbulence or shocks. We carried out a revision of the existing particle acceleration models with the emphasis on their links to magnetic reconnection processes occurring in the Sun and heliosphere and derived particle parameters (energy, directivity, pitch angle distribution) during their passage through reconnecting current sheets occurring in the solar corona (eruptive flares) and in the heliosphere. The investigation of particle acceleration was carried out with a 3D Particle-in-cell PIC approach combined with a 3D test particle (TP) approach. The consequent transport effects of particle propagation in the solar atmosphere were studied by testing flaring atmosphere parameters with simulated hydrodynamic models of flaring atmospheres heated by energetic particles (electrons, protons and their mixture) and resulting seismic signatures on the solar surface caused by these hydrodynamic shocks induced by accelerated particles. This helped us to understand the fundamental properties of accelerated particles after their ejection from reconnecting current sheets and, consequently, to predict the parameters of energetic particles (energy/velocity and pitch angle distributions as well as particle density profiles) passing through the current sheets with low (heliosphere) and high (solar corona) density plasmas and for different types of magnetic field topologies, or scenarios of magnetic reconnection. The predicted parameters of accelerated particles were probed by the multiwave observations of eruptive flares and CMEs in the Sun and associated with them SEP events. We also discovered two populations (low and high energy) of energetic electrons observed in the solar wind which have essentially different pitch angle distributions observed with payload of ACE, WIND and STEREO spacecrafts.

1.2. Project significance

With the increasing significance of space industry and communication satellites around the Earth, as well as the upcoming reality of a future manned mission to Mars, it becomes very important to predict any hazzards in the heliosphere (shocks, high energy particle streams etc), which can affect the health of a human crew or destroy the satellite's solar batteries and payload as happened in 2003 for the 2 satellites during the Halloween flare events. So far this prediction of energetic particles is not very accurate because it is based only on the solar wind particles being produced by the Sun and re-accelerated by the shocks occurred in the passing Interplanetary Coronal Mass Ejections (ICMEs) or Corotating Interplanetary Regions (CIRs). However, observations show that energetic particles (both electrons and ions) can gain much more energy and have much more complex distributions in space than those predicted by shock acceleration caused by ICMEs or SIRs. Moreover, even without any external disturbances like ICMEs or SIRs, the fast solar wind particles (electrons and ions) show very peculiar energy, pitch angle and density distributions at various locations of the heliosphere. These distributions are shown to have strong relation to the magnetic topologies, which the particles are passing through, pointing out to magnetic reconnection process governing these distributions.

DISTRIBUTION A: Distribution approved for public release. Distribution unlimited

A consistent study is required to explore a magnetic reconnection as an acceleration mechanism in 3D approach in the heliosphere where particles can be measured by direct in-situ observations. Based on this study, the more accurate investigation can be carried out for the similar processes in the solar atmosphere to derive the exact conditions of particle dynamics and energy gains during a 3D magnetic reconnection for different magnetic topologies and various physical conditions. This approach will advance the knowledge about energy transfer from a magnetic field to charged particles by establishing when, where and how this energy is transferred to each kind of particles depending on magnitudes and topological properties of magnetic and electric fields. This can be used for prediction of space weather and saving many communication satellites and human lives from harming effects of energetic particles in the heliosphere.

1.2. Project objectives

1. To investigate acceleration of protons and electrons in 3D magnetic field topologies of a single reconnecting current sheet with strong (sun) and weak (heliosphere) magnetic fields:
    - To derive velocity, pitch angle and density profiles of accelerated particles for different magnetic topologies and ambient plasma densities.
    - To investigate transport effects and turbulence generated in different physical conditions.
2. To investigate acceleration of particle in current sheet with magnetic islands:
    - To derive particle velocity, pitch angle and density profiles for given 3D magnetic field topologies and ambient plasmas densities.
    - To modify transport and stability effects in the similar physical conditions as in objective 1.
3. To develop tools for prediction of particle distributions gained after their passage through reconnecting current sheets of a given magnetic topology.

2. Introduction

2.1. Current sheets as primary energy release sites in the Sun and heliosphere

Magnetic reconnection is a fundamental physical process driving the primary release of magnetic field energy in many events in the Sun (Priest & Forbes 2000; Somov 2000; Benz 2017), Earth magnetosphere (Angelopoulos et al. 2008; Chen et al. 2008) and heliosphere (Gosling 2007; Manchester et al. 2014). The magnetic reconnection process converts magnetic energy into the energy of energetic particles (Lin et al. 2003; Zharkova et al. 2011; Zharkova & Khabarova 2012; Muñoz & Büchner 2018), emission generated by particles and associated plasma flows. Observations of hard X-ray (HXR) (Holman et al. 2011) and γ-ray (GR) (Vilmer et al. 2011) emission in solar flares also, to a large extent, supports magnetic reconnection as the main source of energetic particles, from which they gain energy while passing through a diffusion region of magnetic reconnection in current sheets of Harris type (see, for example Zharkova et al. 2011; Egedal et al. 2013, and references therein).

Magnetic reconnection leads to conversion of the free magnetic energy stored in these magnetic structures into other forms of energy (motion, radiation, waves) while accelerating particles to sub-relativistic energies. Moreover, magnetic reconnection is the only process that can link the parameters of accelerated particles to a magnetic field topology of large magnetic loops on the Sun or in the heliosphere.

DISTRIBUTION A: Distribution approved for public release. Distribution unlimited

Magnetic reconnection can occur in several geometries. For example, open magnetic field lines can collapse onto a closed helmet-like magnetic configuration. This leads to a region of high magnetic shear near the top of the closed structure – as evidenced by looptop sources of hard X-rays first ob- served by *Yohkoh* (Masuda et al. 1994) – and in the energization of successive field lines at greater and greater heights, which produces both coronal hard X-ray sources (Krucker et al. 2008a) and a concomitant increase in the separation of the associated hard X-ray and H-a footpoints (Kopp & Pneuman 1976). Magnetic reconnection can also be accompanied by dramatic large-scale changes in the magnetic field configuration, such as in the "breakout" model (Antiochos et al. 1999), in which a filament, previously restrained by the magnetic tension of a set of magnetic field lines exterior to it, is released into interplanetary space as a result of reconnection of the constraining field lines. Reconnection can also result in the formation of magnetohydrodynamic (MHD) shocks, which may be responsible for significant particle acceleration exterior to the region of magnetic reconnection itself. A spatial configuration of reconnection sites can be also presented by more complicated magnetic structures, like tangentially discontinued multiple X-nullpoints (Baumann & Nordlund 2012; Olshevsky et al. 2013), or fan and spine reconnections, or some other shapes of 3D X-nullpoints (see for details Pontin et al, 2011, and references therein).

Whatever the geometry, the fundamental process of magnetic reconnection somehow transfers a significant fraction (e.g., Miller et al. 1997) of the stored magnetic energy into accelerated charged particles, both electrons and ions. Some of the high-energy particles may be trapped in the corona by plasma turbulence (e.g., Petrosian & Liu 2004) and/or by magnetic mirroring (e.g., Melrose & White 1979; Leach 1984; Somov & Kosugi 1997), to produce hard X-ray (HXR) looptop sources (e.g., Masuda et al. 1994; Petrosian et al. 2002; Sui & Holman 2003; Jiang et al. 2006; Battaglia & Benz 2006; Liu 2006). Some particles may escape the acceleration region into interplanetary space and can contribute to solar energetic particle (SEP) events detected at 1 AU (e.g., Krucker et al. 2007a).

Numerous observations of reconnection events in the solar-wind current sheets are obtained by the Advanced Composition Explorer (ACE) and Helios (Gosling et al. 2006; Gosling 2007), WIND (Phan et al. 2010) and Cluster (Chian & Muñoz 2011) spacecraft as well as by combined instruments (see Gosling 2008; Gosling & Phan 2013, and references therein). Many current sheets are found to occur in the heliosphere at the leading edges of interplanetary coronal mass ejections (ICMEs) (see, for example Xu et al. 2011, and references therein). In situ observations by WIND (Phan et al. 2010) have also revealed 34 reconnection sites during continuous observations of high-speed solar-wind data with the flow exhausts embedded within sharp outward-propagating Alfvénic fluctuations. The authors reported the locations of the X-nullpoints, or current sheets, and recorded the local shear angles across their exhausts ranging from 24 to 160° (with the average value about 90°). The width of these exhausts was less than 4×10^4 km, a distance that can be covered by the satellite under 100 s.

Particles are often accelerated during coronal mass ejections (CMEs), which are explosive solar events that involve enormous ejections of plasma and magnetic flux and drive interplanetary dynamics (Gosling 1993, 1994). CMEs are always as- sociated with a filament channel, in the form of a twisted flux rope or sheared arcade, that stores the required free magnetic energy to power the eruption (Gaizauskas 1998; Martin 1998). These structures erupt when destabilized either by reconnection (Antiochos et al. 1999; Moore et al. 2001) or an ideal process, e.g. the torus or kink instability (Amari et al. 2000; Forbes et al. 2006; Titov et al. 2008; Wyper et al. 2017). These eruptions are often accompanied by multi-ribbon flares and solar energetic particles.

In the magnetic breakout model (Antiochos et al. 1994), the energy buildup in the filament channel deforms a coronal nullpoint external to the system to form a current sheet. This current sheet (breakout current sheet) eventually reconnects, removing the flux

DISTRIBUTION A: Distribution approved for public release. Distribution unlimited

overlaying the filament channel, disrupting the force balance, and triggering eruption onset (Antiochos 1998; DeVore & Antiochos 2008; Karpen et al. 2012). A vertical current sheet (flare current sheet) forms beneath the erupting filament and reconnects and drives explosive CME acceleration (Antiochos et al. 1999; Karpen et al. 2012). Plasma heated at the flare current sheet is transferred to post-flare loops, producing flare brightening as well as soft and hard X-ray emission (Gosling 1993; Hudson et al. 1995; Kay et al. 2003; Zharkova et al. 2011). It should be emphasized that the vertical flare current sheet is a generic feature of all CME models, including those that are initiated by a kink or torus instability (e.g. Fan 2010).

Observations of flares show that a significant fraction of the total released magnetic energy is transferred to high-energy electrons and ions (Lin & Hudson 1976; Miller et al. 1997; Lin & Team 2003; Emslie et al. 2005; Vilmer et al. 2011; Emslie et al. 2012). Energetic electrons in flares are observed through bremsstrahlung hard X-ray and gyrosynchrotron microwave emission from the solar corona and chromosphere. There are clear indications of strong particle energization during solar flares (Holman et al. 2011; Vilmer et al. 2011; Zharkova et al. 2011), which may be driven by various mechanisms associated with the magnetic reconnection process producing the energy release (Priest & Forbes 2000; Somov & Oreshina 2000; Zharkova et al. 2011). At the same time, a fraction of energetic particles is shown to escape to interplanetary space as solar energetic particles that can be detected by in-situ observations. By studying particle energization in different breakout and flare current sheets occurring during a CME evolution we aim to understand the energy release by magnetic field restructuring in these events and the energy transfer to energetic particles, and thus determine the properties of the high energy particles produced.

Moreover, in-situ observations in the heliosphere show that the solar wind electrons change their pitch-angles by 180° ('U-turns') when the satellite crosses the heliospheric current sheet (HCS), with a delay (0.5 – 8 hours) from the change of the magnetic field sign and the azimuthal angle (indicates the reconnection site) (Crooker et al. 2004). This U-turn could not be explained by other means than electron acceleration in the HCS with a strong guiding field (Zharkova & Khabarova 2012). Furthermore, anti-parallel beams of energetic electrons, such as bidirectional strahls (Gosling et al. 2004a,b), are often observed in the vicinities of Interplanetary Coronal Mass Ejections (ICMEs) moving perpendicular to the interplanetary magnetic field, and that can be related to magnetic field reconnection in these locations. Hence, particles can not only gain energies but also have their pitch-angle distribution changed while crossing reconnecting current sheets.

Hence, current sheets are widely spread in space plasmas and are accepted to be associated with the locations where magnetic energy is converted into other forms of energy (accelerated particles, waves etc). The observations in hard X-rays and gamma-rays of solar flares (SF) or in-situ observations in the heliospheric current sheet (HCS) imply that the essential part of the released energy has to be converted into the energy of accelerated particles -- electrons and protons/ions.

2.2. Simulations of particle acceleration during magnetic reconnection

Particle acceleration in the complex magnetic structures of a CME and flares could be associated with various reconnection current sheets, which may contain single or multiple X-nullpoints and O-nullpoints, or magnetic islands (Drake et al. 2006; Daughton et al. 2011). The combination of MHD and test- particle methods have been implemented to explore various particle energization mechanisms, such as: super-Dreicer electric field, resistive electric field, turbulence, and collapsing magnetic traps, etc. (see for example, Vilmer 2012; Gordovskyy & Browning 2012; Grady et al. 2012; Borissov, A. et al. 2017; Birn et al. 2017; Isliker et al. 2019, and references therein).

DISTRIBUTION A: Distribution approved for public release. Distribution unlimited

At a fundamental level, of course, charged particles are accelerated by an electric field while magnetic field forms the structure retaining particles in acceleration regions. These include large-scale sub-Dreicer acceleration (see, for example Litvinenko 1996; Zharkova & Gordovskyy 2004; Siversky and Zharkova, 2009; Bessho & Bhattacharjee 2012); super-Dreicer acceleration in a relatively localized 2D current sheet (e.g., Litvinenko & Somov 1993a); stochastic acceleration by MHD turbulence generated in fast plasma reconnection outflows (e.g., Miller et al. 1996; Petrosian 2012) and acceleration by shocks.

Recently Zharkova & Khabarova (2012) (ZH12, thereafter) showed that the passage of solar wind through the heliospheric current sheet (HCS) significantly increases the energy of ions and electrons and their changes pitch angle distributions of energetic particles. A comparison of the observed particle and magnetic field characteristics with the model allowed ZH12 to explain the ion energy distributions across the HCS, their peak velocities and density distributions across the HCS, pitch-angle distributions of energetic electrons, their locations outside the HCS by the plasma feedback due to a presence of accelerated particles. This explanation was extended to the interpretation of solar wind particle parameters passing through the front and tail current sheets of ICMEs (Zharkova and Khabarova, 2015-ZH15).

During a 3D magnetic reconnection with a guiding magnetic field, particles are shown to be first accelerated by a reconnection electric field within a very short sub-millisecond timescale (Zenitani & Hoshino 2001; Zharkova & Gordovskyy 2004; Litvinenko 1996; Bessho & Bhattacharjee 2012; Melzani, Mickaël et al. 2014; Sironi & Spitkovsky 2014). Later the particles can be further accelerated by turbulence (Siversky & Zharkova 2009; Kowal et al. 2012; Lazarian et al. 2012; Muñoz & Büchner 2018; Zhdankin et al. 2019). Particle energization mechanisms include parallel drift (Gordovskyy & Browning 2012), Fermi reflection of particles from the shortening magnetic field line (Hoshino 2012; Dahlin et al. 2014), and betatron acceleration in the perpendicular direction (Fu et al. 2011; Wang et al. 2016a), etc., under the guiding- centre approximation. They could be linked to fluid compression (Zank 2014; Li et al. 2018) and shear effects (le Roux et al. 2015; Li et al. 2018) in the fluid description. Further studies have shown a remarkable consistency between particle energization in 2D and 3D simulations (Hesse et al. 2001; Guo et al. 2014; Dahlin et al. 2017). On the other hand, in 3D models of relativistic reconnection the reconnection rate can drop in comparison to 2D models depending on the specific current sheet parameters (Sironi & Spitkovsky 2014).

Furthermore, highly elongated Harris-type current sheets with a single X-nullpoint are likely to break, owing to tearing mode instabilities, into a chain of magnetic structures of O-type nullpoints, or magnetic islands, surrounded by X-nullpoints as it was shown by magnetohydrodynamic (MHD) (Loureiro et al. 2005; Bárta et al. 2011; Lapenta 2008) and full kinetic (Drake et al. 2006b; Huang & Bhattacharjee 2010; Karimabadi et al. 2011; Markidis et al. 2012; Nishizuka et al. 2015) simulations. Periodic magnetic structures can be indirectly observed from high energy emission in solar flares (Loureiro et al. 2005; Oka et al. 2010; Bárta et al. 2011; Takasao et al. 2012; Nishizuka et al. 2015), by direct observations in the heliosphere (Kurth et al. 1984; Kahler & Lin 1994, 1995; Zharkova & Khabarova 2015; Khabarova et al. 2017) and the magnetotail (Øieroset et al. 2002; Zong et al. 2004; Chen et al. 2008; Wang et al. 2016b). The satellites crossing the heliospheric current sheet (HCS) very often record multiple magnetic structures, which can either merge or contract (Zank et al. 2014; Khabarova et al. 2015). These structures contain a significant amount of energetic ions and electrons with very unique energy and pitch-angle distributions (Kurth et al. 1984; Kahler & Lin 1994, 1995; Zharkova & Khabarova 2012, 2015; Khabarova et al. 2015; Khabarova & Zank 2017).

In the multi-islands phase, particles could be trapped in those magnetic islands and mainly accelerated near X- nullpoints and coalescent regions (Drake et al. 2006a; Oka et al. 2010; Li et al. 2018; Xia & Zharkova 2018). In some cases Fermi processes of converging flows or particle interaction with magnetic islands can become the energization mechanisms, which play a dominant role (Litvinenko 1996; Zharkova & Gordovskyy 2004; E. M. de Gouveia Dal

DISTRIBUTION A: Distribution approved for public release. Distribution unlimited

Pino & Lazarian, A. 2005; Zharkova & Agapitov 2009; Guo et al. 2014; Lapenta et al. 2015; Dahlin et al. 2017). Furthermore, a strong guiding field would introduce the separation, or preferential ejection, of electrons and ions when they escape from a current sheet due to the opposite gyration directions (Zharkova & Gordovskyy 2004; Pritchett & Coroniti 2004; Zharkova & Gordovskyy 2005; Siversky & Zharkova 2009; Zharkova & Agapitov 2009). This separation of the high- energy oppositely charged particles was firstly observed in the solar flare of 23 July 2003 (Lin et al. 2003; Hurford et al. 2003), showing hard X-ray (HXR) sources to be spatially separated from the γ-ray sources. The separation of electrons and protons/ions was later detected in some other flares (Hurford et al. 2006), heliospheric current sheets (Zharkova & Khabarova 2012) and laboratory experiments (Zhong et al. 2016). This separation of oppositely charged particles into the different semiplanes of a current sheet induces an additional polarisation electric field across the midplane (Zenitani & Hoshino 2008; Siversky & Zharkova 2009; Cerutti et al. 2013), as it has been also revealed from observations of the HCS crossing by ions (Zharkova & Khabarova 2012, 2015).

The magnetic topology of reconnecting current sheet even imposes different acceleration rules not only on the oppositely charged particle but also on particles of the same charge. Since electrons and protons are ejected into the different semiplanes, the particles entering from the opposite side of the RCS have different trajectories while reaching the midplane where they become accelerated. The particles that enter the RCS from the side opposite to the side from which they are ejected can be accelerated on their way to the midplane, they thus are classified as “transit” particles. While the particles that enter the RCS from the same side where they are ejected become decelerated while reaching the midplane, are classified as “bounced” particles. It is evident that the transit particles would gain much more energy than the bounced ones (Siversky & Zharkova 2009; Zharkova & Khabarova 2012). Besides, the difference between the energy gains by transit and bounced particle beams would introduce the bump-on-tail distributions, which leads to Buneman instabilities (Buneman 1958) and generates turbulence (see for example Siversky & Zharkova 2009; Drake et al. 2010; Muñoz & Büchner 2018). Fermi-type stochastic acceleration of particles on various type of turbulence can be also considered one of important acceleration mechanisms considered by a number of authors (see for example, Petrosian, 2012, and references therein).

Besides, particles in current sheets gain non-Maxwellian distributions in the phase space due to asymmetric acceleration by reconnection electric field and developed instabilities (Siversky and Zharkova, 2009, JPP). Ng et al, 2011 have found that close to the diffusion region a triangular-shaped distribution in the electron velocity space can be detected, with filamentary structures of different groups of particles, which oscillate across the RCS midplane. However, in the presence of a weak guiding field B_g such the structures would disappear outside the diffusion region (Ng et al, 2012, Wang and Chen, 2016).
Thus, the implementation of a strong B_g in simulations could also help the energetic particle beams to maintain the pressure anisotropy (Le et al, 2013).

Furthermore, we need to consider the anisotropic turbulence occurring along a current sheet from the X-nullpoint to the O-nullpoint in the simulation region because the streaming instabilities can be generated in the separatrices and later extend to the exhaust region (Cattell et al, 2005, Lapenta et al, 2011, Markidis et al, 2012; Zhang et al, 2019b).

2.3. Transport effects of energetic particles in the solar atmosphere

Solar particles accelerated in eruptive flares with helmet-type current sheets are known to be the source of energetic particles ejected into the heliosphere as produced by the breakout model for CME initiation (Antiochos, 1999). This process naturally accounts for a prompt escape of flare-accelerated particles into open interplanetary space producing fast solar wind. From the other hand, the breakout eruption model predicts the occurrences of

DISTRIBUTION A: Distribution approved for public release. Distribution unlimited

magnetic reconnection sites on the both sides from the original polarity inversion line (PIL) prior the main flare onset, e.g. prior the formation above this PIL of vertical reconnecting current sheet of a helmet type causing the main flare (Antiochos, 1999, 2001; Zharkova et al, 2011). This scenario of two-stage magnetic reconnection can explain some puzzling results for some flares when these additional current sheets can cause noticeable particle acceleration with subsequent precipitation as in the interplanetary space [44] so into the loop legs not associated with the locations of main flaring event [45]. For the 15 February 2011 flare these particles produce seismic ripples, or sunquakes, as recently reported by Zharkov et al. 2011 preceding the main flare in HXR emission occurred a few minutes later and eruption of CMEs and Solar Energetic Particles (SEPs) (Krucker et al, 2012). The exact scenarios of particle acceleration in these events are not yet understood and need to be investigated as they shed the light onto the exact scenarios of magnetic processes in the breakout model for flare and CME onset.

Energetic electrons and protons/ions in solar flares are traced from hard X-ray and gamma-ray emission measured by RHESSI and FERMI payload. The RHESSI observations of solar flares often show appearances of two or more footpoints with hard X-ray and gamma-ray emission [46] combined with the coronal HXR sources located well above these footpoints [24,25]. These coronal HXR sources are assumed to be the locations of reconnecting current sheets (RCSs) where magnetic field releases its energy. In addition to HXR footpoint sources, a significant part of the HXR emissions observed in a flare arises from an extended coronal source observed up to 60 keV [25]. These coronal HXR sources were compared with the electric currents in the ribbons [47], which are found to be in a close association with the coronal sources. This lends a support to the models of particle acceleration (both electrons and protons) in reconnecting current sheets during flares (see [3] and references therein).

The accelerated particles in a helmet type current sheets are getting ejected either into the heliosphere (from the top of the helmet) producing solar energetic particles in the solar wind or into a loop legs, or footpoints, producing HXR bremsstrahlung and gamma-ray line and continuous emission after the particles precipitate into a flaring atmosphere in Coloumb collisions [48-51] until they lose their energy completely.

In the recent years, the fundamental role of Ohmic losses was established for beam electrons in the self-induced electric field, in addition to collisions Zharkova and Gordovskyy, 2006, Siversly and Zharkova, 2009b). The inclusion of this electric field helps to resolve **the electron number problem** responsible for observed HXR photon numbers [46,48]. With the inclusions of self-induced electric field the precipitating low energy electrons become returned back to the source in the corona and re-accelerated again and ejected back to the loop leg (or ***recycled***) (Siversky and Zharkova, 2009b) This happens up to 50-100 times per second until the electrons fully looses their energy in collisions, thus reducing by 50-100 times a total number of electrons required to account for observed HXR emission.

These co-spatial currents of precipitating and returning electrons were recently observed by Musset et al. (2012) who studied the magnitudes and changes of vertical electric current densities measured at the photospheric level, during the X2.2 flare on February 15 2011 in AR NOAA 11158. They found for the first time that a X-ray source at 50-100 keV (produced by non-thermal electrons) observed in the course of the flare is co-spatial with a region in which new vertical photospheric currents appeared during the same period. In addition, this electric circuit of precipitating and returning electrons can account for the formation of double power-law HXR photon spectra often observed by RHESSI Zharkova and Gordovskyy, 2006, Siversky and Zharkova, 2009) and the 'soft-hard-soft' pattern of spectral index variations in HXR below 35 keV Zharkova et al, 2010, 2011 and generation of plasma turbulence observed as zebra-patterns in microwave emission (Zharkova et al, 2012).

Moreover, it has been shown that not only electrons deliver energy and momenta to the solar atmosphere and surface and play the important role in plasma heating and

DISTRIBUTION A: Distribution approved for public release. Distribution unlimited

generation of seismic response in the solar interior called sunquakes [58] but also these are often delivered by either pure proton beams [58,59] or by mixed beams of protons and electrons [60]. The locations of sunquakes can either coincide in time and space with flare locations [58-59] or occur well before the main flare onset outside the locations of the main flare as occurred in 15 February flare 2011 (Zharkov et al, 2011) depending on the depth inside the solar interior where the initial impulse is deposited (Zharkova and Zharkov, 2015). Therefore, the conditions for acceleration to high energies of particles of the neutral solar plasma and formation of electron, proton and mixed beams producing these transport effects are very important for understanding the physics of eruptive flares and coronal mass ejections in the Sun. These particles can be also contributing to formation of solar energetic particles (SEPs) in the heliosphere that can be linked to the original magnetic field topologies of reconnecting current sheets in the Sun.

3. Methods, assumptions and procedures

3.1. Investigation of particle acceleration in reconnecting current sheets

Particle acceleration inside a reconnecting current sheet is caused by a drifted electric field, or a reconnection electric field, brought by magnetic diffusion. ***We will combine particle-in-cell (PIC) with test particle (TP) approach,*** in order to derive the full dynamics of accelerated particles.

3.1.1. Test particle approach. Particle trajectories in a 3D magnetic configuration with the guiding field were studied numerically by using a test particle (TP) approach for a constant drift electric field (Zharkova and Gordovskyy, 2004; Zharkova & Agapitov 2009; Xia and Zharkova, 2018) for an electric field enhanced due to particles drag into a diffusion region where reconnection occurs.

3.1.1.a. Magnetic & Electric field topology near a single X-nullpoint

In the simulations with a single X-nullpoint, B_{static} and E_{static} induced by external condition (MHD scale) are described as follows:

$$\begin{aligned} B_{static,x} &= B0\xi_x \cosh^{-1}(x/d), \\ B_{static,y} &= -B0\,\xi_y, \\ B_{static,z} &= -B0 \tanh^{-1}(z/d) \end{aligned} \qquad (1)$$

where d is half the thickness of the RCS in the x direction, a is the length of a whole current sheet along z direction ξ_x and ξ_y are used to define the relative strength of different magnetic components. The parameter ξ_y defines the location of the simulation region along y (guiding field) direction,
, when using test particle (TP) approach (Zharkova & Agapitov 2009). For the PIC simulations, ξ_x remains a constant within the PIC simulation region meaning each simulation is carried for a particular slice of the whole current sheet along z defined in TP models. On the other hand, ξ_y defines the strength of the guiding field. If $\xi_y = 1$, it gives a force-free equilibrium. The initial reconnection electric field E_{static} is assumed to be constant as inside the reconnecting region so outside it. Similar to the previous paper (Xia & Zharkova 2018) this electric field has to be perpendicular to the current sheet plane:

$$E_{static} = \{0, E_0, 0\}, \qquad (2)$$

where the max amplitude of E_0 can be calculated from the plasma inflow into the RCS:

DISTRIBUTION A: Distribution approved for public release. Distribution unlimited

$$E_0 = V_{inflow} B_0. \quad (3)$$

3.1.1.b. Motion equation

$$\frac{d\mathbf{x}}{dt} = \frac{\mathbf{p}}{m\gamma} \quad (4)$$
$$\frac{d\mathbf{p}}{dt} = q\left(\mathbf{E} + \frac{1}{c}\frac{\mathbf{p}}{m\gamma} \times \mathbf{B}\right)$$

where q and m are particle charge and mass, respectively, p=mV is particle momentum, V – velocity, γ is the relativistic factor, B and E are the vectors of magnetic and electric fields described in section above.

The motion equation for a charged particle is solved in 3D magnetic field topology of magnetic field reconnection and a super-Dreicer reconnection electric field brought by these particles.

The relativistic equations of motion for charged particles are calculated in a stander manner with the Boris rotation algorithm (Boris 1970). The numerical timestep is restricted by the Courant-Friedrichs-Lewy (CFL) condition, $\Delta t < c^{-1}(\Delta x^2 + \Delta y^2 + \Delta z^2)^{-1/2}$ where Δx, Δy, Δz are the grid spacings in each direction. Besides, the time step is also restricted by the electron gyro-frequency: $\Delta t < 0.2\omega^{-1}$. The grid size is selected to satisfy the condition $\Delta x < \lambda_D$, where λ_D is the Debye length.

3.1.2. Particle acceleration in magnetic islands

3.1.2.a. Magnetic field topology

Let us consider current sheets with a few 3D O-nullpoints separated by X-nullpoints from both sides of magnetic is- lands, which are initially assumed to have the same shapes and dimensions. The magnetic field in the islands is adopted from Kliem (1994), which is also known as the Fadeev equilibrium model (Fadeev et al. 1965) with added constant out-of-plane guiding field B_y:

$$B_z = -\frac{\sinh\left(\frac{x}{d}\right)}{\cosh\left(\frac{x}{x}\right) + \epsilon\cos\left(\frac{kz}{d}\right\}} B_0$$

$$B_x = -\frac{\epsilon\sin\left(\frac{kz}{d}\right)}{\cosh\left(\frac{x}{x}\right) + \epsilon\cos\left(\frac{kz}{d}\right\}} B_0; \quad (5)$$

$$B_y = B_0\zeta_y$$

where d is again the half thickness of RCS near the O- nullpoint, ξ is the same parameter as in Eq.(1). ε, k are the mathematical parameters controlling the dimension of the periodic islands: $k = L_i/d$ measures the ratio of the distance L_i from the centre of the O-nullpoint to the closest X-nullpoint, or called the half length of the island, to the current sheet half thickness d_i. This model is valid for a series of identical islands periodically occurring along x = 0 m plane. In our simulations k = 1.0,0.03125 are used, where k = 1 is the original value accepted in Kliem (1994) and also used in the continued test particle study of Li & Lin (2012), and k ≈ 0.03125 for the magnetic geometry in Drake et al. (2006a). Meanwhile, ε = 0.3 to keep consistent with Kliem (1994). We consider particles to be uniformly dis- tributed at

DISTRIBUTION A: Distribution approved for public release. Distribution unlimited

both boundaries of the chain and injected into these islands, deriving their trajectories and energy distributions.

3.1.2.b. Reconnection electric field

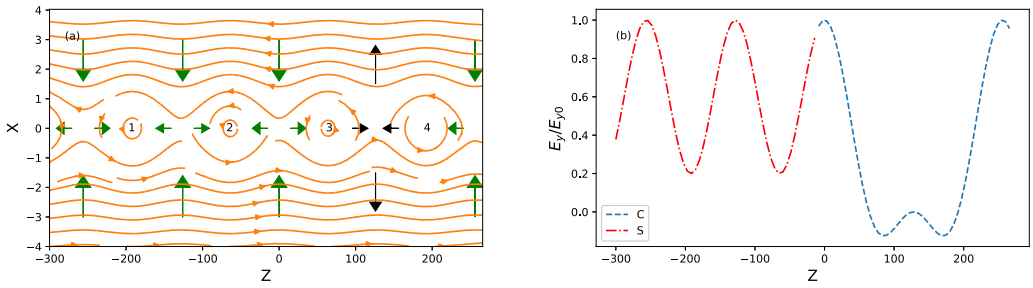


Figure 1. The plasma inflow (green arrows) and outflow (black arrows) directions (left) and polarisation electric field (right) in a magnetic islands chain. Left: The solid orange lines show the magnetic field in the x − z plane. The islands `1' and `2' represent the squashed islands, while islands `3' and `4' represent the coalescent islands. Right: The red dash-dot line shows the Ey from squashed islands on the midplane from Eq.(6). The blue dash line shows the Ey from coalescent islands on the midplane from Eq.(7). Here k = 0.03125.

We introduce two types of magnetic islands: one has plasma inflows at both X-nullpoints of the magnetic island (squashed), and the other one has plasma pushed away at certain X-nullpoints (coalescent).

SQUASHED MAGNETIC ISLANDS

For this type of magnetic island, which have eclipse-type shapes, the plasma is suggested moving into an O-nullpoint from both X-nullpoints. This motion is similar to the plasma inflow coming into the RCS as shown by the green arrows in Fig. 1a. The corresponding electric field in such islands is adopted from Li & Lin (2012):

$$E_y = E_{y0}[0.6+0.4\cos(kz/d)]. \quad (6)$$

It means that the plasma flows into the squashed islands from all the directions, which makes Ey parallel to the re- connection electric field everywhere. Hence, the particles in squashed islands are only affected by $E_y > 0$ as shown by the red line in Fig.1b.

COALESCENT MAGNETIC ISLANDS:

In contrast, the electric field for coalescent islands where the two islands move towards each other is suggested by Kliem (1994) as:

$$E_y = E_{y0}\cos(kz/2d)\cos^2(kz/4d), \quad (7)$$

This electric field is not symmetric about the centre of the island. Although this type of magnetic island could have the same dimension as the squashed one, the direction of the plasma flow at certain regions is different. As shown by the black arrows in Fig.7a, the coalescent structure described by Eq.(6) means that two islands(e.g., island `3' and `4') on each sides of the X-nullpoint are merging into a single one. In this case, the magnetic islands

DISTRIBUTION A: Distribution approved for public release. Distribution unlimited

centred at z = 64 m and 192 m are moving towards each other (shown by horizontal black arrows) and merging into a single island. The plasma between the islands is, thus, pushed outwards as shown by the vertical black arrows. In this contracting (outfow) region, the electric field $E_y < 0$ is anti-parallel to the reconnection electric field at the boundary as shown in Fig.1b. Hence, the coalescent islands described by Eq.(7) actually contain both a contracting region (with outflow, $E_y < 0$) and squeezing region (with inflow, $E_y > 0$), while the squashed islands only have $E_y > 0$.

Now, in order to match with our previous studies near the X-nullpoints, the simulations would start with the parameters close to the corona environment: n = 10^{15} m^{-3}, d=2m, T =100eV,E_0 =100V/m, $B_0 \approx 10^2$ G and ε = 0.3, leaving k as a free parameter.

3.1.3. Particle-in-cell approach.

The test particle approach considers only motion of charged particles in 3D electro-magnetic fields which existed prior particles were dragged into a diffusion region of the reconnecting current sheet. These particles carry large charges and induce strong polarisation electric and magnetic fields across the current sheet (Zharkova and Agapitov, 2009). These induced electric and magnetic fields and their effects on particle parameters and reconnection scenarios can be only investigated with the ***self-consistent full kinetic (or particle-in-cell –PIC) 2.5D-3D simulations*** (Verboncoeur et al., 1995), Bower et al, 2008; Siversky and Zharkova, 2009).

3.1. 3. a. Updated motion equation

In order to evaluate particle acceleration during a magnetic reconnection, and to separate the electromagnetic fields of the original configuration from that induced additionally by accelerated particles, we consider the original electromagnetic field topology of the magnetic reconnection to be static, with **B**$_{\mathbf{static}}$ and **E**$_{\mathbf{static}}$ are the relevant fields described in section 3.1.1. The static field coming from large-scale plasma flow is the starting point, in which particles start their motion inside a diffusion region.

While there is also new electromagnetic fields induced by accelerated particles during their motion inside the current sheet, which are called the variable electric $\tilde{\mathbf{E}}$ and magnetic fields $\tilde{\mathbf{B}}$ as described below in section 3.1.3.b. The resulting electro-magnetic fields are

$$\mathbf{E} = \mathbf{E}_{\mathbf{static}} + \tilde{\mathbf{E}}, \qquad (8)$$

$$\mathbf{B} = \mathbf{B}_{\mathbf{static}} + \tilde{\mathbf{B}}.$$

3.1.3. b. The plasma feedback

In this project, we adopted a 2D3V or 2.5D (3D by velocity and 2D by coordinate) PIC simulation code, called XOOPIC developed by Verboncoeur et al. (1995), and also used a full 3D code VPIC code (Bower et al, 2008), to benchmark the previous PIC study (Siversky & Zharkova 2009) and 3D test-particle approach (Zharkova & Agapitov 2009; Xia & Zharkova 2018).

A useful feature of this PIC code is that it can split the electromagnetic field E and B to two components, the background E_{static} and B_{static} (used in TP approach), and the local self-

DISTRIBUTION A: Distribution approved for public release. Distribution unlimited

consistent $\tilde{E}$ and $\tilde{B}$ induced by the particle motions (can be only evaluated in PIC approach): $B = B_{static} + \tilde{B}$, and $E = E_{static} + \tilde{E}$. Then the fluctuation electric and magnetic field fields are calculated from the Maxwell's equations:

$$\partial \tilde{E}/\partial t = c\nabla\times\tilde{B} - 1/\varepsilon(j_e+j_p), \quad (9)$$

$$\partial \tilde{B}/\partial t = -\nabla\times\tilde{E}, \quad (10)$$

where c is a speed of light, j_e and j_p are the current densities of electrons and protons, updated by the particle solver. The Maxwell's equations are solved numerically by standard finite-difference time-domain method (FDTD). This approach can help us to identify the effect of the ambient particles that are drifted into a current sheet by the magnetic diffusion process of reconnection.

The RCS thickness in the simulations starts at the gyroradius of proton $d = 1(\rho_i)$. The simulation region is $L_x \times L_z = 20 \times 1024$. In full 3D simulations with the VPIC code (Bowers et al. 2008), the simulation domain is changed to $L_x \times L_y \times L_z = 20 \times 20 \times 1024$, where L_y is along the out-of-plane direction. The boundary conditions for the particles and fields are chosen to be periodic along y. Along x− and z−directions, conducting boundaries are imposed for the electromagnetic fields, and open boundaries are set for the particles (particles are free to leave and will not come back). In order to avoid the problem with a small Debye length, we start PIC simulations with only a small fraction of the plasma particles (with an ambient density n_a of $10^{10} - 10^{12}$ m^{-3}), with an average of 100 particles per grid cell.

Depending on the simulations required, we assume the static electric and magnetic fields come either from the heliosphere or from the coronal plasma with the relevant physical parameters. The mass p-e ratio will be accepted to be equal to 100-500, the speed of light is standard, plasma density is varying from 1-10 (heliosphere) to 10^6-10^7 cm^{-3} (solar corona). For the coronal plasma with $T = 10^6$ K, $n = 10^{12-16}$ m^{-3} (Battaglia & Kontar 2012), which has the Alfvén speed $V_A = 2 \times 10^6$ m/s, and the average thermal velocity of the proton and electrons $v_{Tp} = 10^5$ m/s, $v_{Te} = 6\times10^6$ m/s. The plasma inflow velocity is typically $0.01-0.1V_A$ (Priest 1984), which is much smaller than the thermal velocity v_{Tp}. This leads in the coronal plasma to the reconnection electric field of $E_y \approx 100 - 650$ V /m. The simulation length is measured in the units of proton gyro-radius ρ_i for the magnetic field magnitude of B_0. Because in the given flare condition, the mean free path $\lambda_{mfp} \geq 10^5$ m is much larger than the typical thickness of the current sheets ($\sim 10\rho_i \leq 100$ m), the simulations in this paper omit any collision operators (Poletto et al. 1975). The simulations generally run over a long time $t \approx 1200\Omega^{-1}$, where Ω_{ci} is the ion cyclotron frequency. For simulations for the solar wind particles during their passage of the sector boundary, or HCS we use a very low plasma density and magnetic field magnitudes of 1-10 nT relevant to those measured in the heliosphere.

3.2. Investigation of particle transport in flaring loops

3.2.1. Flaring atmosphere heating by particle beams

Energetic electron or proton beams, which are ejected from the diffusion region formed by the interacting magnetic loops engaged in magnetic reconnection and

DISTRIBUTION A: Distribution approved for public release. Distribution unlimited

precipitating towards their footpoints, cause essential heating of the ambient plasma via a hydrodynamic response. The precipitating particle beams are shown sweeping the ambient plasma from the QS chromosphere towards deeper atmospheric levels, thus, converting the QS chromosphere into a flaring atmosphere with its own corona, transition region and chromosphere (Somov et al, 1981; Zharkova and Zharkov, 2007; 2015).
The parameters of an injected beam are usually selected close to the range of parameters of HXR or gamma-ray emission derived from observations with a single power-law energy spectrum with a spectral indices gamma based on a comparison of spectral indices using Fokker-Planck approach and a lower cut-off energy was accepted to be 10 KeV.

The energy deposition functions, or heating rates, for these particles are calculated using distribution functions found from the full kinetic approach by solving the Fokker-Planck equation for electrons losing their energy in collisions and Ohmic heating (Zharkova & Gordovskyy 2005b) and protons in the generation of kinetic Alfven waves (KAWs) and their dissipation via Cherenkov resonance (Gordovskyy 2005; Gordovskyy et al. 2005).. We do not include the energy losses by slow electrons, since these are negligible compared to the other particles (Gordovskyy et al. 2005).

3.2.2. Hydrodynamic response of flaring atmosphere

For physical conditions in a flaring atmosphere we used a 1D hydrodynamic response of the ambient plasma heated by a power law electron or proton beams, simulated by Zharkova & Zharkov, 2007; Druett and Zharkova, 2018. This is similar to the model by Somov et al. 1981 updated with added hydrogen radiative losses (Kobylinsky and Zharkova, 1996).

We consider a limited region of the quiet Sun (QS) chromosphere with column depths $\xi_{min} \le \xi \le \xi_{max}$, with $\xi_{min} = 10^{17}$ cm^{-2} corresponding to the QS transition region, followed by the chromosphere and at $\xi_{max} = 10^{22}$ cm^{-2} corresponding to the upper photosphere.

3.2.2.a. Hydrodynamic equations

$$\partial n/\partial t + n^2\, \partial v/\partial \xi = 0;$$

$$\partial V/\partial t + 1/\mu(n k_b[T_i+T_e)] = 4/3\mu\, \partial/\partial\xi[\eta_i n\, \partial v/\partial\xi] + g_{sun}. \quad (11)$$

$$n k_b\, /(\gamma-1)\partial T_i/\partial t - k_b T_i\, \partial n/\partial t = 4/3\eta_i n^2(\partial v/\partial\xi)^2 + Q(n,T_i,T_e)$$

$$n k_b\, /(\gamma-1)\partial(xT_e)/\partial t - x k_b T_e\, \partial n/\partial t + n\kappa\, \partial x/\partial t =$$

$$= n\partial/\partial\xi(k_b\, n\, \partial T_e/\partial\xi) + P(n,\xi) - L(n,T_e) - Q(n,T_i,T_e)$$

where n is an ambient density, Te and Ti – an ambient temperature of electrons and ions, v – an ambient plasma macrovelocity, ξ is a column density, P(n,ξ) is a heating function by particle beams (Syrovatsky and Shmeleva, 1972), $L(n,T_e)$ - is a radiative cooling function (Cox and Tucker, 1969), $Q(n,T_i,T_e)$ – the ion viscosity (Somov et al, 1981).

3.2.2.b. Initial and boundary conditions

The initial QS chromosphere is assumed to be in hydrostatic equilibrium and the temperature is constant, e.g.

DISTRIBUTION A: Distribution approved for public release. Distribution unlimited

$$v(0, \xi) = 0, \quad (12)$$
$$T_e(0, \xi) = T_i(0, \xi) = T_0 = \text{const}, \quad (13)$$

where the initial temperature T_0 was derived from the semi-empirical simulations equal to 6700 K.

The initial plasma density of the QS chromosphere is defined as follows
$$n(0, \xi) = n + h^{-1}(\xi - \xi), \quad (14)$$

where $n_{min} = 10^{10}$ cm^{-3} and h_0 is the height scale in a flaring loop:

$$h_0 = [k(1+x)T_0]/mg_s, \quad (15)$$

where k is Boltzmann's constant, x is the ionisation degree, g_s is the solar acceleration of gravity, $\mu = 1.44m_H$ is the average atom mass of the ambient plasma, m_H is the mass of hydrogen atom.

Let us neglect any heating fluxes at the top and bottom boundaries, e.g.
$$\partial T_{e,i}/\partial \xi\ (i, \xi_{min}) = \partial T_{e,i}/\partial \xi\ (i, \xi_{max}) = 0, \quad (16)$$

Let us also consider the upper boundary at the initial time to be a free surface at the presence of the external pressure p_{cor} described as:

$$p_{cor}(0, \xi_{min}) = n_{min}k[1 + x(T_0)]T_0. \quad (17)$$

The plasma velocity at the lower boundary is defined by the equation

$$\partial v/\partial \xi\ (t, \xi_{max}) = 0. \quad (18)$$

The plasma is heated by an electron beam precipitating from the top boundary with the heating function derived from continuity equation. Plasma cooling is caused by the motion between electrons and ions and radiative cooling updated with the hydrogen radiative losses.

After solving this system of four partial differential equations (11) with the initial and boundary conditions (12-18) for precipitating electron beam with given parameters (initial energy flux F_0 and spectral index γ) we obtain time- dependent distributions of electron T_e and ion T_i temperatures, ambient plasma density n and macrovelocities, V.

3.3. Radiative transfer of Hydrogen emission (code HYDRO2GEN)

For the interpretation of hydrogen emission, a full non-LTE approach is used for a 5 level plus continuum hydrogen model atom. Both radiative and collisional mechanisms of hydrogen activation and deactivation are considered for thermal and beam electrons, external and internal diffusive radiation, and three-body recombination. Here we consider hydrogen excitation and ionisation by beam electrons in addition to thermal ones, because only the non-thermal rates can explain the rapid (one second or so) increase of Hα line emission in the core and wings. Thermal electrons, even with higher temperatures, cannot account for timing and shape of the observed Hα line emission.

For non-thermal hydrogen excitation and ionisation rates by beam electrons the analytical formulae by Zharkova & Kobylinskii (1993) were used, with the beam electron densities calculated from the continuity equation. Stimulated photo-excitation, de-

DISTRIBUTION A: Distribution approved for public release. Distribution unlimited

excitation, and ionisation rates by external sources were taken from Zharkova & Kobylinskii (1993).

Nonthermal excitation and ionisation rate

$$C_{nn'} = N_e B_{nn'} \ \text{sec}^{-1}, \qquad (1)$$

$$B_{nn'} = \sqrt{\frac{2}{m}} \int_{E_0}^{\infty} \sqrt{E}\, f(E)\, \sigma_{nn'}(E)\, dE \ \text{cm}^3/\text{sec}, \qquad (2)$$

$$N_e^F(\xi) \approx \frac{F_0 \left(\frac{m}{2}\right)^{1/2}}{(E_2^{2-\gamma} - E_1^{2-\gamma})} \frac{2-\gamma}{2} (2a\xi)^{\frac{1-2\gamma}{4}} \frac{\Gamma\left(\frac{3}{4}\right)\Gamma\left(\frac{2\gamma-1}{4}\right)}{\Gamma\left(\frac{\gamma+1}{2}\right)}, \qquad (4)$$

The absorption profiles in the lines, α(x), were taken in the form of a Voigt function, where x is a dimensionless wavelength measured in Doppler half widths from the line central wavelength. The effective Doppler half widths of spectral lines, $\Delta\nu_D$, defined by thermal motion of hydrogen atoms are calculated for the temperature profiles from the hydrodynamic model for every instant of beam injection by considering the contribution of the relevant Doppler widths from each layer weighed by the layer thickness. Turbulent velocities were included in the calculation of the Doppler half widths, and were around 1 km·s^{-1} in the flaring chromosphere. At all depths this produced only a very small additional contribution to the Doppler half widths due to thermal velocities. For the Balmer lines Stark's effect, due to strong electric fields caused by ionisation of the ambient plasma, was also considered.

TABLE I. Comparison of Excitation and Ionization Rates ($B_{nn'}$, B_{nc}) of a Hydrogen Atom for Beam Electrons with γ = 3 (first row) with Analogous Rates for "Thermal" Electrons

n	n'=2	3	4	5	6	c
1	0.162−07 *	0.389−08	0.138−08	0.655−09	0.364−09	0.615−08
	0.206−12	0.611−14	0.108−14	0.371−15	0.173−15	0.709−15
	0.941−16	0.634−18	0.682−19	0.185−19	0.765−20	0.150−19
2		0.326−06	0.714−07	0.262−07	0.128−07	0.484−07
		0.635−07	0.646−08	0.170−08	0.702−09	0.166−08
		0.131−07	0.927−09	0.200−09	0.740−10	0.764−10
3			0.189−05	0.413−06	0.149−06	0.164−06
			0.117−05	0.157−06	0.724−07	0.609−07
			0.594−06	0.641−07	0.290−07	0.125−07
4				0.636−05	0.146−05	0.393−06
				0.541−05	0.819−06	0.335−06
				0.341−05	0.471−06	0.120−06
5					0.159−04	0.774−06
						0.950−06
						0.449−06

*Read as $0.162 \cdot 10^{-7}$.

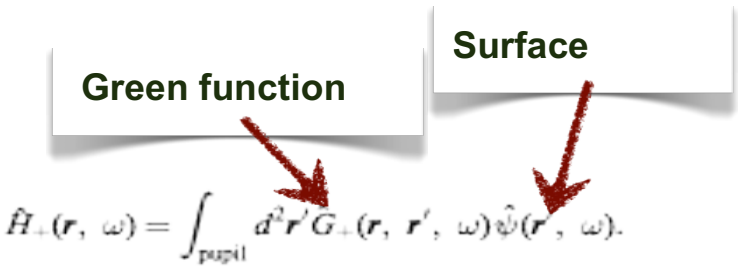
DISTRIBUTION A: Distribution approved for public release. Distribution unlimited

The joint solution of radiative transfer and statistical equilibrium equations for 5 level plus continuum hydrogen atoms were used to define source functions in each atomic transition, intensities of hydrogen lines in Lyman, Balmer and Paschen series and ionisation degree of hydrogen atoms in the atmosphere at any given instant of a hydrodynamic response to particle beam injection. For the lines and Lyman continuum, which are optically thick, the radiative transfer equations are solved in the integral form (Druett and Zharkova, 2018, 2019). The integral was calculated over all the optical depths up to its maximum value for each different wavelength, $\tau 0$. The kernel functions, $K1$, in the lines and Lyman continuum are given separately as described by Druett and Zharkova, 2018, 2019. T is the kinetic temperature of the plasma, v is the frequency of the radiation and $v1c$ the frequency in the Lyman continuum head. $E1(x)$ is the exponential integral of the first kind.

3.4. Generation of seismic emission in the solar interior

3.4.1. Acoustic holography for measuring sunquakes

Helioseismic holography is the phase-coherent computational reconstruction of the acoustic field into the solar interior, in order to produce stigmatic images of the subsurface sources generating the disturbance (Braun & Lindsey, 2000). Central to calculating egression is the Green's function, which de- scribes acoustic wave propagation from a point source in or- der to backtrack the observed surface signal. Generally, these functions can be constructed through ray theory (Lindsey & Braun, 2000; Zharkov et al., 2011a) for a monochromatic point source, as used in this work, or through wave theory (Lindsey & Braun, 2004). Egression is calculated from the Green's func- tion, $G+(|r - r'|,v)$, as such in the temporal Fourier domain (Zharkov et al., 2013)



(19)

where $\hat{\psi}(r',v)$ represents the surface signal obtained from the HMI data, r and θ are polar coordinates around the sources. Egression power is then calculated by integrating the modulus squared over time as such:

$$P(z,\mathbf{r}) = \int dt |H_+(\mathbf{r},z,t)|^2 dt \qquad \textbf{(20)}$$

Sunquakes are usually identified as localised enhanced emission coincident with the flare spatially and temporally, with the acoustic egression kernels usually identified on egression power snapshots around the time of the flare, $P(r, t_{flare})$, via a suitable threshold.

3.4.2. Time distance diagram for measuring sunquakes

Time-distance diagrams (Kosovichev & Zharkova, 1998; Zharkov et al., 2013) aim to measure and to interpret travel times of acoustic waves on the solar surface. They are com- puted by

DISTRIBUTION A: Distribution approved for public release. Distribution unlimited

choosing a central point source location, then rewriting the observed velocity signal at the surface into polar co- ordinates, and applying an azimuthal transformation as follows:

$$V_m(r, t) = \int_{\alpha}^{\beta} v(r, \theta, t)\, e^{im\theta} d\theta, \qquad (21)$$

over a full circle or over a selected arc alpha-beta (if the ripples are directional). After about 20 seconds from a flare onset the surface wavefront can be seen as ripples travelling with an increasing speed from the flare site. In the time-distance diagram the loca- tions of ripples are plotted versus the times that is presented as a ridge describing the ripple travel, which can be compared with a theoretical ray path. This ridge can be extrapolated back in time allowing for more precise determination of the onset time of the acoustic source. Not all flares show discernible ripples despite some of them still having seismic signatures detected with a helioseismic holography.

3.4.3. Hydrodynamic response of the solar interior

Hydrodynamic shocks from the flaring atmosphere above the solar interior can be used as the initial condition for another hydrodynamic model developed for the acoustic wave propagation in the solar interior (Zharkov, 2013). As the initial hy- drodynamic shock terminates within relatively shallow depths and with strongly supersonic velocities, the generated waves are formed at the point of deposition as a closed cone around the velocity vector in the solar interior, which, in accordance to Fermat's principle, propagates deeper into the interior refracting due to the increasing temperature and reflecting back to the photosphere.

Using sound speed and Lamb's acoustic cut-off frequency from the solar interior model, one can solve the equation for acoustic wave propagation in the interior either analytically for a polytrope (Zharkov, 2013) or numerically (Shelyag et al., 2009) for the Christensen-Dalsgaard numeric model S (Christensen-Dalsgaard et al., 1996). Thus, using the analytic solution for a polytrope model (Zharkov, 2013) we can evaluate the parameters of acoustic wave packets generated in the inte- rior and the condition of their detection from Doppler observations on the solar surface, while the numeric model can help to obtain more realistic acoustic signatures. As shown by Zharkov (2013), the vertical shock perturbation moving with a super- sonic velocity can generate a set of multiple acoustic waves, or rays, from which only the waves with the phase speed exceeding a certain threshold (see equation (5.8) in Zharkov, 2013) can reproduce the observed signatures of acoustic waves.

An individual ray, characterised by a constant frequency, ω, and horizontal wavenumber, k_h, initialised at a given depth, propagates into the solar interior and, generally will have, at least, two, upper and lower, turning points (see Fig. 1 in Zharkov, 2013). The lower turning point indicates where the wave moving to the interior is reflected back to the surface by changing its direction of its motion because of Fermat's principle. The first upper turning point along the ray defines the first surface appearance of the acoustic wave (as a first ripple), or the first bounce. Then the propagating ripples correspond to a sequence of the first bounces of the source-generated acoustic rays from the packet reaching in succession their first upper turning points. This reflection of acoustic waves from the solar surface creates a visible motion of ripples on this surface from the flare site.

The source of the deposited impulse, depending on its properties, generates a family of the rays that provides a solution to the ray equations in the phase space and defines the generated wave front. As the source is located in the interior, the first ray (out of all generated by the source) to reach its upper turning point defines the minimal distance where the ripple is formed. This distance will depend on the momentum deposited by the source.

DISTRIBUTION A: Distribution approved for public release. Distribution unlimited

4. Results and discussion

In this project we have studied particle acceleration in magnetic islands with a test-particle (TP) approach (Xia & Zharkova 2018, Xia et al, 2020) and PIC approach (Xia and Zharkova, 2020, 2021, Khabarova et al, 2020) exploring the energy distributions of transit and bounced particles in coalescent and squashed magnetic islands. PIC approach did consider the ambient plasma feedback to a presence of accelerated particles via induced electric and magnetic fields. The PIC approach served us to understand the observed characteristics of particle accelerated in magnetic islands.

4.1. Accelerated particles in 3D RCS with single X-nullpoint – test particle approach

4.1.1. Particle separation effect

The particle trajectories (Fig.2) are plotted for electrons and protons accelerated in an RCS with 3D magnetic field components for a current sheet thickness d = 1 m, a magnitude of magnetic field B_0 = 100 G, and reconnection electric field E_y = 100 V/m. Our simulation results

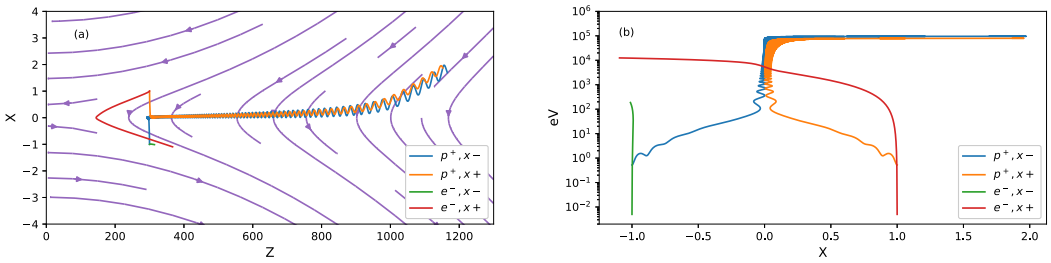


Figure 2. The trajectories of selected electrons (`E1', `E2'), and protons (`P1', and `P2') in different locations of current sheets (Xia and Zharkova, 2018) are plotted for the same RCS parameters as in Fig.1 (with a guiding ?eld $B_y = \xi B_0$ and $\xi = 0.1$): left - the trajectories on the Z − X plane with a magnetic field lines plotted in magenta as the background; right - the energy gains by the particles versus the x− coordinate at ejection. All the particles start from x = ±1 m, z = 300 m.

confirm the previous findings (Zharkova & Gordovskyy 2004; Siversky & Zharkova 2009) that the particles of a different charge reveal strongly asymmetric trajectories and different directions of ejection into the opposite midplanes with respect to the RCS midplane. Because of their opposite charges, and the directions of gyration about B_y, protons and electrons, become ejected into the opposite semiplanes from the mid- plane X=0 (Zharkova & Gordovskyy 2004), thus, moving into the opposite directions of B_x component (Zharkova & Gordovskyy 2004; Zharkova & Agapitov 2009). In Fig.2a, both electrons are ejected to the `x-' half space. On the other hands, in the same magnetic topology, protons are ejected to the `x +' branch.

As indicated in the discussion, this separation effect was observed in the 23 July 2002 solar flare showing hard X- ray sources spatially separated from the gamma-ray sources (Lin et al. 2003; Hurford et al. 2003), then for the flare of 28 October 2003 (Hurford et al. 2006) and recently confirmed by the laboratory experiments (Zhong et al. 2016).

4.1.2. Transit and bounced particles of the same charge

Particle trajectories are shown in Fig. 2. The particle entering an RCS from the same side, where it is to be ejected to, is classified as a `***bounced***' particle (red proton trajectories in Fig.2, right plot), while the particle entering from the side opposite to that where it is to be ejected

DISTRIBUTION A: Distribution approved for public release. Distribution unlimited

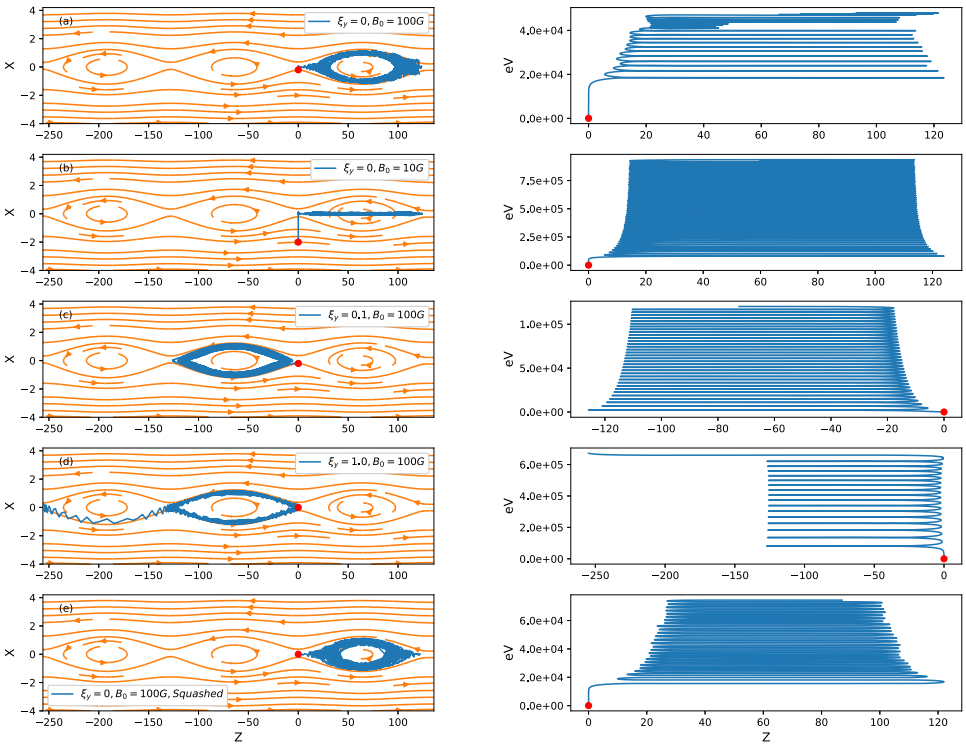
to is classified as a `***transit***' particle (blue proton trajectory in Fig. 2 right plot) (Siversky & Zharkova 2009). While travelling to the midplane, the `transit' particle gains energy while the `bounced' particle loses energy (Siversky & Zharkova 2009). This is demonstrated in Fig.2a, b where the `transit' electron (labelled as particle `E1' in the plot) is found to gain more energy than the `bounced' one (labelled as particle `E2').

Additionally, by comparing trajectories for protons in Fig. 2 (right) one can notice that the `transit' electron gains sufficient energy and leaves the current sheet faster than the `transit' proton. On the other hand, the `bounced' electron is reflected back from RCS even before it could reach the midplane in Fig.2 (left) while the `bounced' proton could move into the midplane in Fig.2 (right).

4.2. Acceleration in coalescent and squashed islands - test particle approach

4.2.1. Particle trajectories

Similar to an RCS with a single X-nullpoint shown in Fig.2, in the multiple O-nullpoints unmagnetized electron moves away from the X-line and crosses the magnetic field lines along the midplane (x = 0) as shown in Fig.3b. On the other hand, if the particle is magnetized, it circles inside the O-nullpoint following the magnetic field lines as shown in Fig.3a. The trajectory of the magnetized electron is similar to those reported by the other papers (Kliem 1994; Drake et al. 2006a; Li & Lin 2012; Dahlin et al. 2015). In both cases, magnetized or unmagnetized, accelerated electrons go back and forth inside a magnetic island between the two X-nullpoints. The acceleration mechanism here is identical to the previous studies in the RCS with a single X-nullpoint, occurring due to the out-of-plane reconnection electric field. Naturally, following Eq.(6) the energy gained by particles is larger when B_X is weaker if the other parameters are identical.



DISTRIBUTION A: Distribution approved for public release. Distribution unlimited

Figure 3. The test particle orbits (left column) and energy gains (right column) versus z-coordinate (in blue lines) obtained during the same running simulation time, $\Delta t = 8 \times 10^{-5}$ s for: (a) a magnetized electron in the magnetic island described by Eq. (5) and (6) with $B_0 = 100$ G. The guiding field $B_y = 0$. (b) a unmagnetized electron in the magnetic island with the same dimension as (a) and $B_0 = 10$ G. (c) a magnetized electron in the magnetic island which has the same B_x and B_z components as (a) with added guiding field $B_y = B_{z0}\xi$, where $\xi_y = 0.1$. (d) a magnetized electron in the magnetic island which has the same B_x and B_z components as (a) and (c) with a stronger guiding field , $\xi_y = 1.0$. (e) an electron in the magnetic island which has the same magnetic field topology as panel (a) for the electric field following Eq.(6) representing squashed islands. The magnetic field lines of B_x, B_z are plotted in orange lines for all the cases. Here $k = 0.03125$, $\varepsilon = 0.3$.

Similar to an RCS with a single X-nullpoint, the presence of a guiding field B_y in the O-type reconnection region leads to particles gaining more energy than without guiding field (see Stanier et al. 2017, for details, and references therein). For the simulation times of $12\Omega^{-1}$ ($\Omega^{-1} = 6.56 \times 10$ s) there are three cases presented: no guiding field (Fig.3a), weak guiding field (Fig. 3c) and strong guiding feld (Fig. 3d).

Energy gains by particles in coalescent and squashed islands are also different. The electric field in coalescent islands (see Eq. 7) shown in Fig.3a between 0 and 240 m has a squeezing region with $E_y > 0$ at $z \in (0,50$ m) and a contracting region where $E_y < 0$ as shown by the blue dash line in Fig.1b at $z \in (80m,120m)$ and at $z \in (120m,180m)$, while the two islands are moving towards each other. The electron is shown in Fig.3a to gain energy only in the squeezing region.

On the other hand, the electric field of a squashed magnetic island in Fig.3e, which is described by Eq.(7), has two squeezing regions ($E_y > 0$) located near $z = -120$ m and 0 m as shown as the red dash-dot line in Fig.1b. Therefore, the electrons become accelerated at both X-nullpoints of the island, that during the same simulation running time results in the particle gaining more energy in this island compared to the coalescent one (Fig.3a).

By comparing the results above with those for electron acceleration in a single X-nullpoint, it can be found that the travelling distance of accelerated particles along the mid-plane is much shorter in the multiple X- and O-nullpoints (as shown in Fig.2). For example, in highly magnetized cases, the particle would either be trapped in multiple magnetic islands and become accelerated again and again (e.g., Fig.10c), or can be trapped within a single island until it reaches a very high energy allowing it to break from an RCS. While the particles still gain energy when they move close to the other X-nullpoints, very often the first trapping island can be sufficient for electrons to gain sub-relativistic energy and to break from an RCS. This effect significantly reduces the restrictions on a current sheet length, required to produce high energy (relativistic) electrons, thus, making current sheets with magnetic islands the efficient primary accelerators of particles.

4.1.2. Energy spectra

Firstly, it is found that when the guiding field is stronger, a particle spends more time cycling in the island before it gains sufficient energy to escape the trapped island. These energy thresholds of the ejected electrons are measured when the particles leave the first islands as shown in Fig.3ae,f. For this type of magnetic topology, the energy gain ΔE_{es} is slightly proportional to a guiding field magnitude, e.g. $\Delta E \propto \xi^{0.1}$. This dependence is not as strong as for the X-nullpoint type acceleration defined by Eq. (7), thus suggesting that the electrons in these simulations are not fully magnetized.

DISTRIBUTION A: Distribution approved for public release. Distribution unlimited

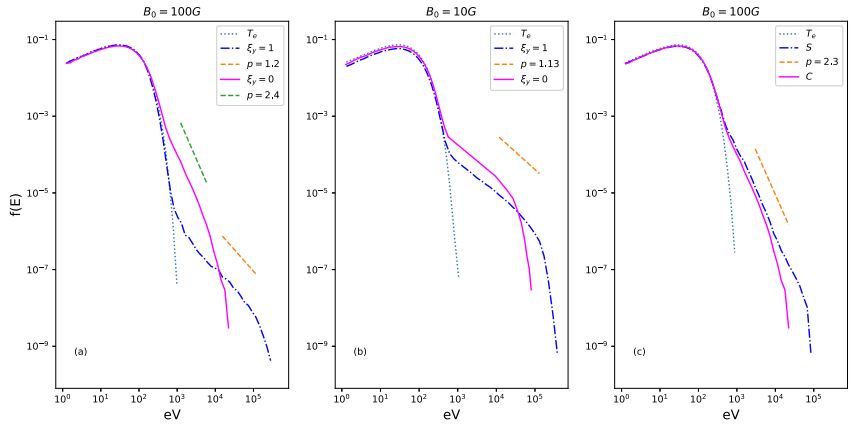


Figure 4. The energy spectra of electrons accelerated during t = 8×10^{-5} s in the coalescent islands with magnetic field magnitudes: (a) B_0 = 100 G, and (b) B_0 = 10 G: Both ξ_y = 0 (the blue dash-dotted line) and ξ_y = 1 (red lines) cases are compared in the same plot. (c) The energy spectrum of electrons in squashed (`S') islands (blue dash-dotted line) with $\xi_y$ = 0. For comparison, the spectrum of the $\xi_y$ = 0 case in (a) from coalescent islands (`C') in is also plotted as a background. The green dotted lines indicate the initial thermal distribution with T_0 = 100 eV. The other parameters are as follows: E_{y0} = 100 V/m, ε = 0.3, k = 0.03125, d = 2 m. Note that the dash lines show only the referral power-law indexes in different cases and do not represent the whole fitting range of energies gained (up to three orders of magnitude on the plots)).

Secondly, by increasing the length of the magnetic island L_i to make them larger, we discovered that the larger is a magnetic island, the higher is the energy gained by the accelerated particles as shown in Fig.4. This is because near the X-nullpoint the amplitude of the fluctuation of $B_x(z)$ is smaller, while the amplitude of E_y drops slower when L_i/d is larger as shown in Fig.1b. It was shown by Zharkova & Gordovskyy (2005a) that in the X-nullpoint acceleration, the increase of E_y/B_x would strongly enhance the energy gain. By decreasing k in Fadeev's model (Eq. 16), L_i could be elongated in the midplane. Therefore, the energy gains of particles at ejection from the first island increases when the ratio L_i/d of the island is larger, even when B_{z0}, E_{y0}, and d are the same outside of the RCS as presented in Fig. 4.

4.3. Acceleration during coronal mass ejections in breakout models – TP approach

In this part we investigated particle energization and transport during a large CME by directly simulating the orbits of test particles in an MHD simulation. We examine both the impulsive and gradual phase of flare reconnection in an ultra-high resolution 2.5D MHD simulation (Karpen et al. 2012) (see Fig. 5), for which the main differences between the two phases are the decaying strength of the reconnection guide field and the slackening of the reconnection rate. The guide field decrease is associated with a reduction in shear of post-flare loops (Fletcher et al. 2011). Particle acceleration results obtained for 2.5D MHD models with plasmoids in the breakout sheet are compared with those for a 3D MHD simulation, in which plasmoids are generated in the flare current sheet instead.

DISTRIBUTION A: Distribution approved for public release. Distribution unlimited

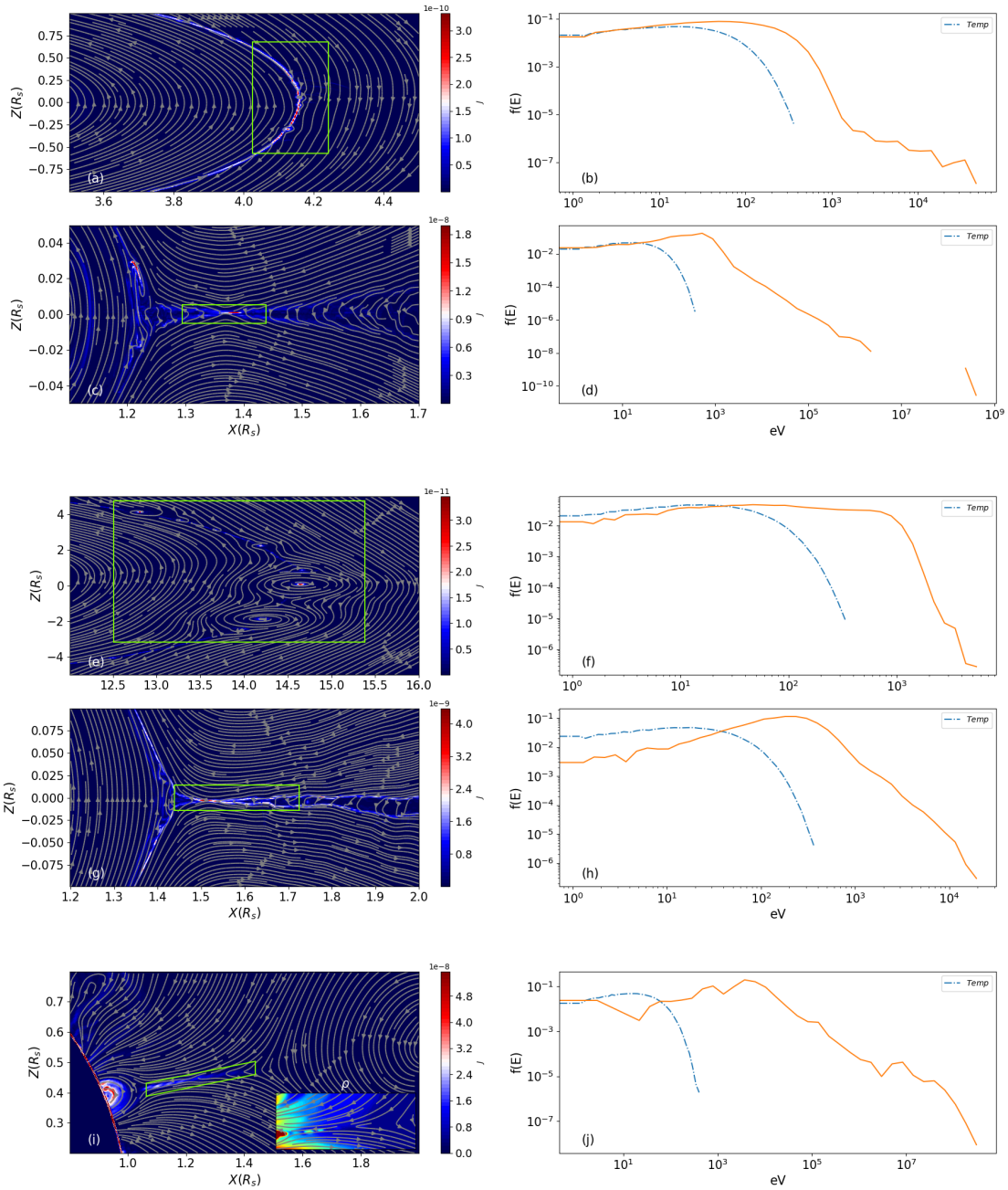


Figure 5. Particle acceleration in a breakout CME. The left column contains the current densities in five different MHD simulation regions (the in-plane magnetic field lines are in grey; the green boxes indicate where the test particles are initialized). The right column shows the corresponding energy spectra of protons at the end of the simulations (blue dashed-dotted lines benchmark the initial status). From top to bottom: (a) the breakout CS and (c) flare CS from the same 2.5D MHD simulation with a strong guiding field; (e) the breakout CS and (g) flare CS from another 2.5D simulation with a weak guiding field; (i) the flare CS in the plane of a 3D simulation with a strong guiding field, in which the plasma density distribution shows the magnetic islands in the CS more clearly at the right corner.

We selected three distinct frames from the MHD simulations as background electromagnetic fields for the test- particle simulations (see Fig. 5). These include the two main reconnection sites in the breakout model as well as cases with strong/weak guide fields and plasmoids in the flare CS. The first two cases represent, respectively, the impulsive and gradual phases of the same 2.5D CME simulation: (case 1) Fig. 5(a) and 5(c) are snapshots of the breakout and flare CSs at the same time during the impulsive phase, during which the flare

DISTRIBUTION A: Distribution approved for public release. Distribution unlimited

CS has a strong guide field; (case 2) Figs. 5(e) and 5(g) are taken during the gradual phase, during which the flare CS has a weak guide field and there are several large plasmoids in the breakout CS. The last example, (case 3) Fig. 5(i) is the flare CS during the impulsive phase from a 3D simulation. This case represents reconnection with a strong guide field and with several small magnetic islands near the primary X-point.

For every CS, 10^5 test particles were initialized in the green regions in the left column of Fig. 5. At the conclusion of the simulations, we obtained the energy spectrum as shown in the right column of Figure 5, which included both the escaped particles and the ones still in the MHD domain. A comparison between Figs. 5(b) and 5(d), and Figures 5(f) and 5(h) reveals that particle acceleration in the flare CS region is more efficient than in the breakout CS, with or without a significant guide field.

We further note that particles gain more energy in the impulsive phase CSs with a stronger guide field. The energy spectra show that the highest energy protons achieve 5×10^4 eV (Fig. 5b) to 3×10^6 eV (Fig. 5d) while the maximum energy is only near $6 \times 10^3 - 2 \times 10^4$ eV in Figs. 5(f) and 5(h). Particle acceleration is much weaker in those CSs with a weak guide field, even when there are several X-nullpoints (Figure 1g) and magnetic islands (Fig. 5e). In many kinetic simulations of magnetic reconnection, particles are strongly accelerated near the X-nullpoints, magnetic islands, etc., within a few hundreds of ion inertial length (Drake et al. 2005, 2006; Siversky & Zharkova 2009; Oka et al. 2010; Egedal et al. 2012). Our results indicate that breakout reconnection, even with plasmoids, and gradual phase flare reconnection are less effective at accelerating particles than the flare reconnection during an impulsive phase.

Our analysis of the particle transport equations and comparison with TP simulations of particle accelerations shows that the drift motion of particles along the perpendicular electric field provides strong particle energization. The curvature drift accelerates particles parallel to the magnetic field, and is important in the magnetic islands and the outflow regions close to the X-nullpoints. In contrast, Betatron acceleration plays an important role further downstream, e.g. at the flare loop top, and. Preferentially, accelerates the particles in the perpendicular direction (also reflected in the pitch-angle distributions). The magnetic energy evolution in the simulation domain suggests that the change of magnetic energy related to flow compression becomes most important in the flare reconnection downstream in the flare loop. The amplitudes of the energization terms in different scenarios are generally consistent with their maximum energy gains of the test particles.

In summary, we have identified particle acceleration processes on large-scale magnetic structures related to explosive CMEs that extend far beyond the small-scale regions where the flux-breaking occurs. The produced energetic particle distribution is not symmetric with respect to the X-nullpoints in the RCSs. Reasons for this behaviour include the preferential ejection due to the guiding field Bg, and the magnetic confinement structures, e.g., magnetic islands and helmet-like flare loop tops. These structures could change the transport of energetic particles and even produce a secondary acceleration in the reconnection downstream, or reinject particles into the reconnection CS from the exhaust. The enhancement of hard X-ray emission during the impulsive phase of the flare is due primarily to the highly sheared magnetic field near the polarity inversion line driving explosive guide-field reconnection. Our results suggest that the combined MHD and test-particle simulations could be used to predict the maximum energy gain of particles in different observed magnetic configurations, which may have a critical application to space weather models.

DISTRIBUTION A: Distribution approved for public release. Distribution unlimited

4.4. Acceleration of particle in magnetic islands – PIC approach

4.4.1. Separation of protons from electrons

The PIC simulations of particle acceleration in a low-density current sheet reproduce the similar results obtained from test-particle simulations, as the asymmetry of electrons and protons at ejection from a current sheet is clear in the velocity phase space (Fig.6) (Siversky & Zharkova 2009; Xia & Zharkova 2020). The PIC simulations for higher ambient plasma density reveal the noticeable differences from the test-particle approach where the asymmetry of ejected protons and electrons is more distinguishable in the energy distributions (Fig.6c,d) rather than in the density distributions (Fig.6a,b). In the current 3D PIC simulations we also show the particle density and energy distributions over each side of the midplane, which was not available in 3D TP (Xia & Zharkova 2018).

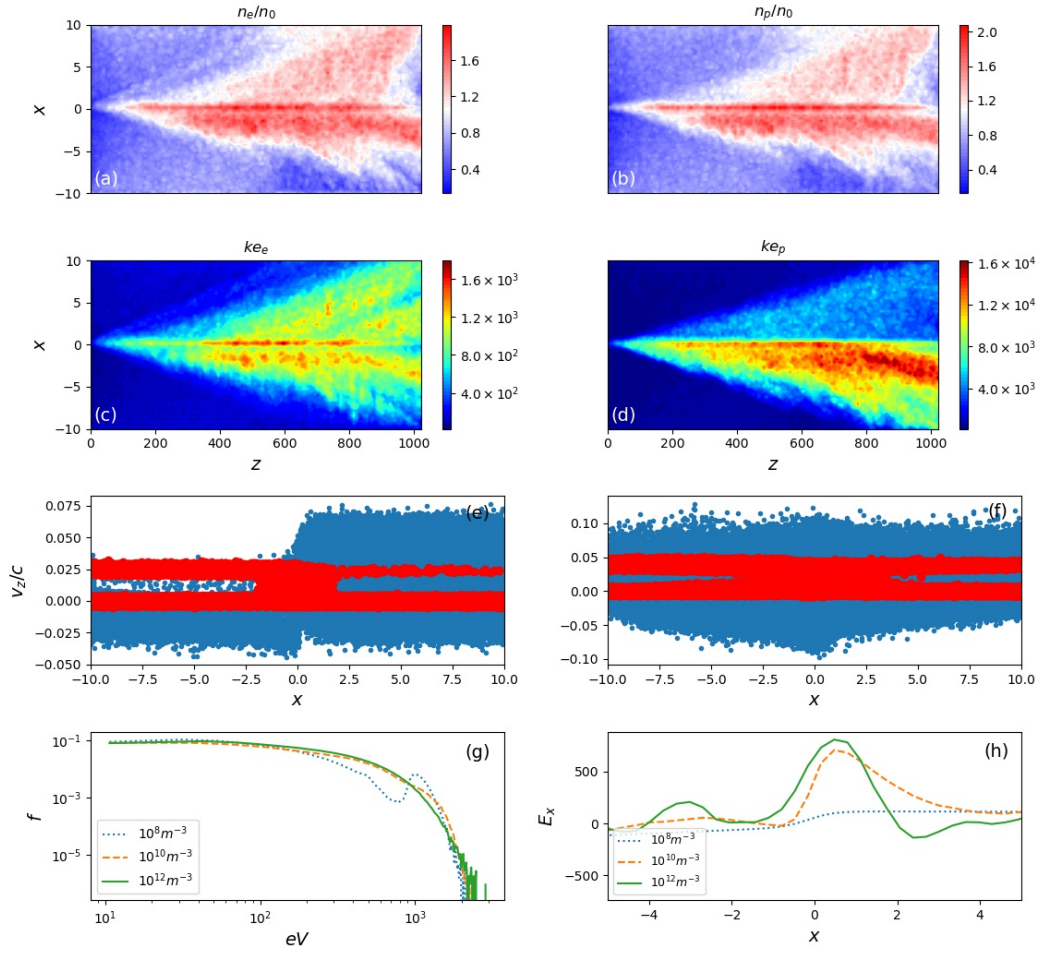


Figure 6. The upper half: the density and energy (in eV) distributions of electrons (a, c) and protons (b, d) at t = $140\Omega^{-1}$ for m_i/m_e = 100, $n_0 = 10^{12}$ m^{-3}. The magnetic field $B_0 = 10^{-3}$ T, B_y/B_0 = 0.1, B_x/B_0 = 0.02, and electric field E_0 = 250 V/m. The lower half: the V_z vs x distributions in the velocity phase space for (e) $n_0 = 10^8$ m^{-3} and (f) 10^{12} m^{-3}. (g) and (h) compare the energy spectra and the polarization electric field E_x vs. x at t = $50\Omega^{-1}$ among the simulations with different densities.

DISTRIBUTION A: Distribution approved for public release. Distribution unlimited

Another important outcome of this charge separation of particles at acceleration in current sheet is the induction of the polarization electric fields $\tilde{E}_x$ and additional varying magnetic fields in PIC simulations. The induced $\tilde{E}_x$ is mainly perpendicular to the RCS midplane and it becomes larger when the ambient plasma density increases (Fig.6h). It is larger than $\tilde{E}_y$ and $\tilde{E}_z$ by an order of magnitude that is close to the previous estimations (see also Zharkova & Gordovskyy 2004; Zenitani & Hoshino 2008; Cerutti et al. 2013)

4.4.2. Transit vs bounced particles of the same charge

There is also seen a distinction between the dynamics of particles of the same charge entering a reconnecting current sheet from the opposite edges. Namely, the particles entering the current sheet from the same side, to which they are to be ejected, are classified as bounced particles; the particles entering the CS from the opposite side, to which they are to be ejected, are classified as transit particles.

The 'transit' particles gain much higher energies and form the power-law tail of energy spectra while the 'bounced' particles gain much smaller energies and often have a quasi-thermal wide spectra (Xia and Zharkova, 2020). In fact, accelerated electrons passing through a reconnecting current sheet are split into two distinct groups in energy: the low-energy 'bounced' electrons (with the energies < 300–600 eV) and 'high-energy' transit electrons (with energies of KeVs). The value of the threshold depends on the magnetic field magnitudes being higher at larger magnetic fields and lower at smaller magnetic fields.

This is caused by transit, or bounced, electrons gaining, or losing, their energy while reaching the midplane where the main acceleration occurs. The uneven distributions of transit and bounced particles across the midplane, well distinguishable in TP approach, are harder to notice in the velocity phase space for PIC simulations if a guiding field is small (Fig.6f) and more noticeable for a larger guiding field (Fig.6e). This is caused by the action of polarisation electric field (Fig.6h).

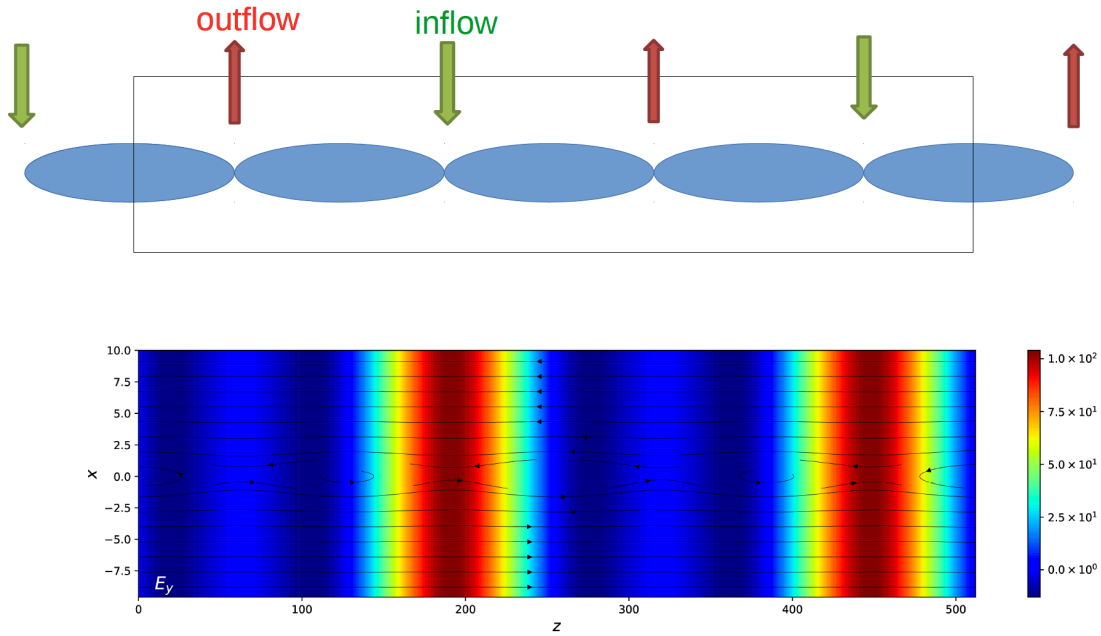


Figure 7. The upper plot: The scheme of coalescent magnetic islands and the plasma flow direction. The bottom plot: The amplitude of $E_{y,c}$ (V/m in the colour bar) from Eq.(11) in the magnetic field topology. The parameters for $E_{y,c}$ are k = 0.0325, ε = 0.3, d = 2, and E_0 = 100 V/m.

DISTRIBUTION A: Distribution approved for public release. Distribution unlimited

4.4.3. Current sheets with magnetic islands – PIC approach

Similar to the TP studies in section 4.1.2 (Xia & Zharkova 2018), we explore the two types of magnetic islands: squashed, or contracting, magnetic islands, where the plasma flows into the islands from all directions (see Fig. 7) and coalescent magnetic islands, or merging islands, that the two islands move towards one another (Xia and Zharkova, 2020). The current sheets with magnetic islands have a similar thickness of d_{CS} = 2 as considered for RCSs with a single X-nullpoint.

The electrons and protons are injected into the simulation domain from both X-boundaries, which are located at a distance L = ±10 m away from the midplane of an RCS. We compared the resulting magnetic and electric fields generated during a magnetic reconnection with single and multiple X-nullpoints (magnetic islands) in 2.5D and 3D PIC simulations providing the ambient plasma feedback inside a CS, particle energies, densities and pitch angles obtained for different magnetic topologies (Xia and Zharkova, 2020).

In general, the particle energy gains in the islands obtained with the current PIC simulations are higher and achieved on shorter spatial scales than those in the single X-nullpoint PIC and TP simulations. Considering that the magnetic topologies for single and multiple X nullpoints have the similar electric and magnetic field parameters and overall sizes of current sheet, this suggests that within the current sheets of similar dimensions the particles are accelerated more efficiently in the magnetic islands than near a single X-nullpoint.

As the simulation evolves in time, the magnetic field topology is changed significantly since the magnetic islands are merging, so the magnetic field lines evolve around the merging magnetic islands (similar to that shown in Fig.1 in Pritchett 2008). As result, at later times of simulations, there is a decrease of high-energy particle numbers in the islands with open boundaries indicating that high-energy particles escaped the magnetic islands through these boundaries.

4.4.4. Coalescent magnetic islands

The simulation carried with 2.5D PIC approach for the coalescent magnetic islands is shown in Fig.8 (top plot) with relevant reconnection magnetic field shown in Fig.8 (bottom plot). The particle density and energy distributions in two coalescent islands are plotted in Fig.8 at the time t = 560 Ω^{-1}, when the maximal particle energies are achieved and in Fig. 9 at the time t = 1120 Ω^{-1}.

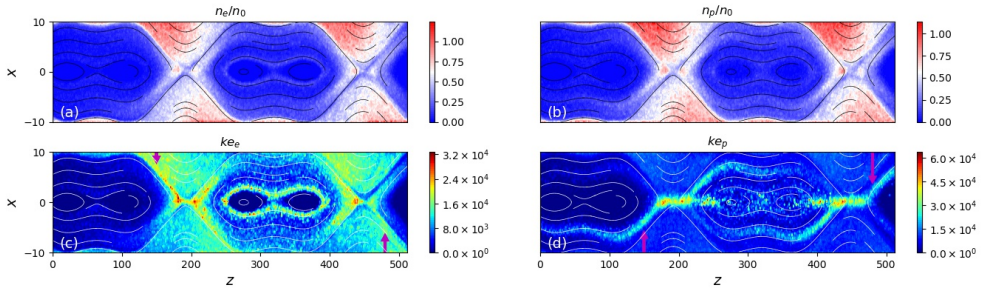


Figure 8. The density and energy distributions of particles in the coalescent magnetic islands at t = 560 Ω^{-1}. The arrows indicate the open regions with asymmetrical energy distributions between electrons and protons. The other simulation parameters are k=0.0325,ε=0.3,d=2,E_0 =100V/m,B_Y/B_0 =0.1,B_0 =10^{-3} T, and n_0 =10^{12} m^{-3}.

DISTRIBUTION A: Distribution approved for public release. Distribution unlimited

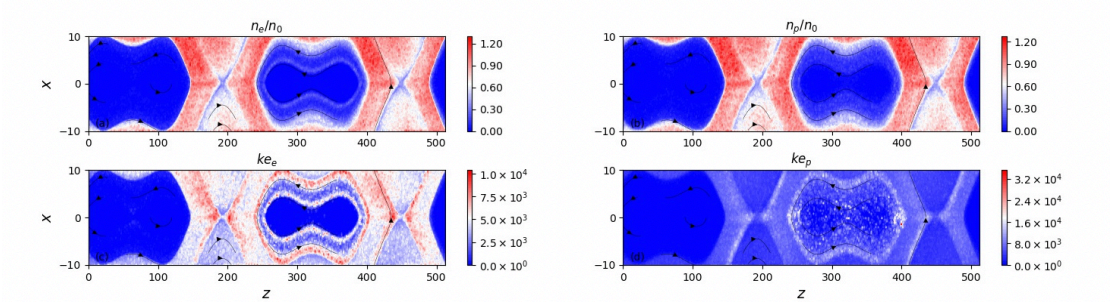


Fig. 9. The density and energy distributions of particles in the coalescent magnetic islands at a later time t = 1120 Ω^{-1} in the same simulation as presented in Fig.8.

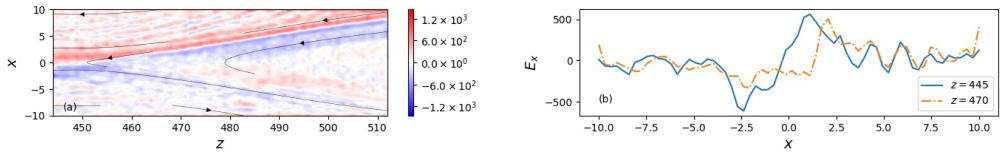


Fig. 10. The polarization electric field E_X from the simulations previously presented in Fig.8: (a) the map of E_X in the open field region z > 445 and (b) the values of E_X across the midplane for different z in the left contour.

The particle density and energy distributions show a clear asymmetry with respect to the midplane (indicated by the arrows in Fig.8,9) due to the guiding field B_Y, which is similar to that reported for particles moving about a single X-nullpoint in section 4.4.1.

For example, in the fully open the magnetic island boundaries in z below 130 m and above 480 m marked by black arrows, the high energy electrons are moving to the upper (x > 0) half plane (see Fig.8,9a) and (b)) while the high-energy protons tend to move to the lower (x < 0) half plane see Fig.8,9(c) and (d)). Hence, the particles are ejected into the diagonally opposite quarters from the islands, thus, verifying the preferential ejection phenomenon being valid for coalescent islands.

Fig.10 depicts the local electric field component $\tilde{E}_X$ in the open magnetic field region in Fig.8. Similar to the $\tilde{E}_X$ component in Fig.6, the amplitude of $\tilde{E}_X$ in magnetic islands is larger than the reconnecting electric field E_0 (100 V/m). On the other hand, $\tilde{E}_X$ switches the sign near the midplane in Fig.10 (b) in the single X-nullpoint geometry. While in magnetic islands this polarisation electric field does not always flip the sign near the midplane, as indicated by the edge between blue and red colors in Fig.10(a). In the open field region, $\tilde{E}_X$ switches the sign along the separatrix of the magnetic field lines. More specifically, Fig.10(b) shows that $\tilde{E}_X$ changes sign near x = 0 in the z = 445 plane, then in the downstream at z = 470, $\tilde{E}_X$ changes sign near x = 2.0 in this case. Thus, the polarization electric field extends beyond the X-nullpoint diffusion region.

4.4.4a. Particle energy gains in coalescent islands

Guiding field:

In the previous simulations with a single 3D X-nullpoint, section 4.2, it was shown that electron acceleration is boosted by the presence of a guiding field. The similar effect happens in magnetic islands when the guiding field increased from B_Y/B_0 = 0.1 (Fig.8) to 1.0

DISTRIBUTION A: Distribution approved for public release. Distribution unlimited

as shown in Fig.11. The maximum energy gain of electrons in the magnetic topology with By is increased by ~ 37% (3.2×10^4 eV to 4.4×10^4 eV), while the proton energy is only increased by ~ 3%.

4.4.4b. Aspect ratio of the length-to-thickness of magnetic islands:

By keeping identical the outer-scale electro-magnetic fields of RCS, let us explore the effects of island dimensions on particle acceleration, e.g., the length and thickness of magnetic islands, which are controlled by the parameters k, ε, and d in Eq.(7) and Eq.(8), respectively. If we decrease k = 0.03125 to 0.015625 while keeping the other parameters constant, it would double the length of the magnetic island L_i (because $L_i = d/k$) in Fig.12. In this elongated coalescent magnetic island, particles are accelerated to higher energies as shown in the bottom panel. This happens due to the fact that with smaller k the ratio $|E_y/B|$ near the X-nullpoint is increased from Eq.(11) and Eq.(8), which leads to higher energy gains as it was derived from the test-particle approach (Xia & Zharkova 2018).

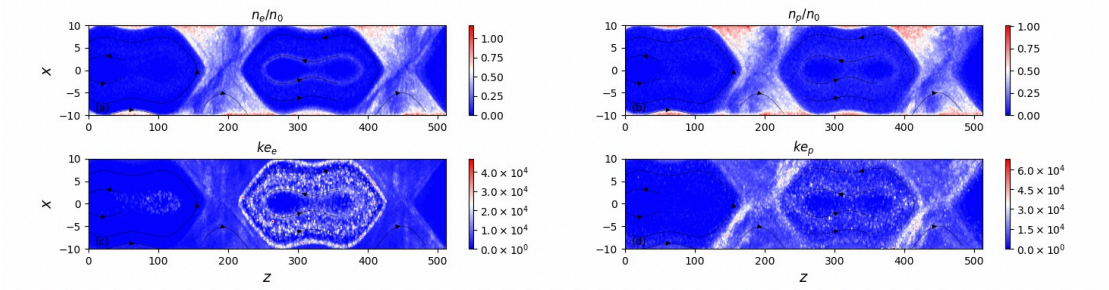


Fig. 11. The density (top panel) and energy (bottom panel) distributions of particles in the coalescent magnetic islands at t = 560 Ω^{-1} when B_y/B_0 is increased to 1.0 from the simulation in Fig.9.

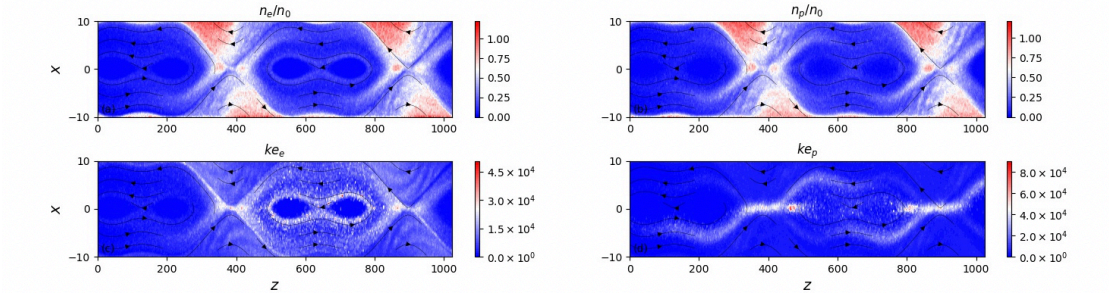


Fig. 12. The density (top) and energy (bottom) distributions of particles in the coalescent magnetic islands at t = 560 Ω^{-1} with k = 0.015625. The other parameters match with the ones used in Fig.9.

4.4.5. Squashed magnetic islands

Let us consider another type of magnetic islands, squashed ones, by replacing the electric field of coalescent magnetic islands described in section 4.4.2a,b with the one representing squashed magnetic islands. We should mention that preferential ejection and induced polarisation electric field by the guiding magnetic field are also presented in the open magnetic field region of squashed magnetic islands, similar to the coalescent ones in

DISTRIBUTION A: Distribution approved for public release. Distribution unlimited

Fig.11-12. This is visually hard to see the asymmetric energy distribution in the open field region in Fig.13(c) and Fig.13(d) because the amplitudes of the distributions in the exhaust are relatively lower than the ones in the middle of the islands.

By comparing the current results shown in Fig.13 with those obtained after the same simulation time for coalescent magnetic islands shown in Fig.11 and 12, it can be observed that the energy gains by particles are noticeably higher (by factor six or larger) in the squashed islands as can be derived from the units in the colour bars (Xia and Zharkova, 2020). This can be explained by the difference between the resulting reconnection electric field of the squashed and coalescent islands (see the model descriptions). Namely, the merging area of coalescent islands has Ey < 0, which is anti-parallel to the reconnecting electric field, while the resulting reconnection electric field remains all positive across the whole domain when a magnetic island becomes squashed.

Therefore, the energy gains of particles in the squashed island are much higher than in the coalescent island that has the same initial magnetic field geometry. This is close to the result reported for the test-particle study (Xia & Zharkova 2018) with a difference that in the PIC simulations the maximal energies are higher than in the TP approach because they stay longer inside the squashed islands where the particles gain the bulk of energy in Fermi acceleration. Furthermore, we notice that the energetic particles are confined in the centre & midplane of the squashed islands, while they circle about the X-nullpoints in the coalescent islands.

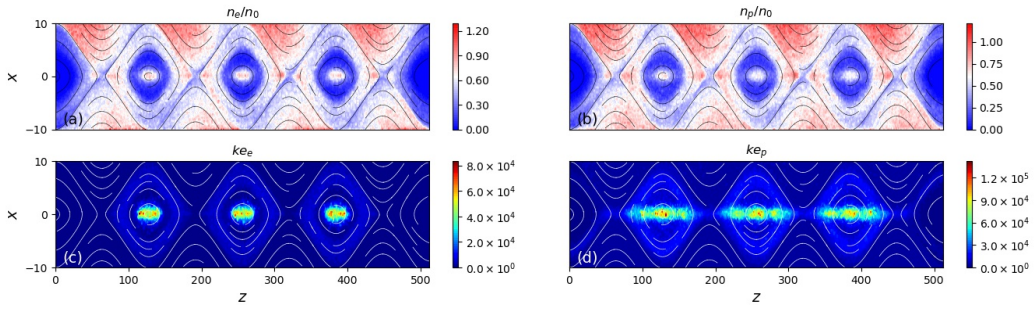


Figure 13. The energy distribution of particles in squashed magnetic islands at t = 560 Ω^{-1}. The initial electric field comes from Eq.(8). The other physical parameters are identical to the simulation in Fig.8. The ambient plasma density was equal to 10^{10} m^{-3}.

4.4.6. Energy gains in magnetic islands

The energy spectra shown in Fig.14 are affected by variations of the parameters in magnetic islands, such as a guiding field strength and the aspect ratio of the length- to-thickness changes. The energy gains by electrons are enhanced in the elongated magnetic islands (the curve 'C_{k2}': k = 0.015625), and when the guiding magnetic field increases (the curve 'C_{By}': By/B0 = 1). The variations of the proton-to-electron mass ratio does not change much the energy spectra of accelerated electrons for the same magnetic field topology, only affecting the maximum energy gains (compare the curves '$C_m{}'_1$, 'C', '$C_m{}'_2$ in Fig.14). Besides, there are more energetic electrons produced in the squashed magnetic islands ('S') than in the coalescent magnetic islands ('C') that makes the spectra in squashed islands harder.

Furthermore, energy gains by transit electrons are much higher than by bounced ones, dividing the populations of energetic electrons by the threshold energy of 300 − 500 eV

DISTRIBUTION A: Distribution approved for public release. Distribution unlimited

for bounced and up to hundred keV energies for transit electrons. This leads to a bump-on-tail energy distribution of accelerated particles ('C_{By}'), which is similar to the electron

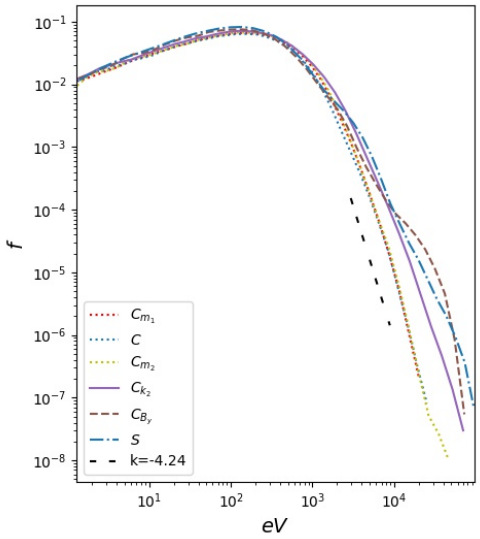


Figure 14. The energy spectra of electrons in the simulations which have been presented in Fig.8 ('C'), Fig.12 ('C_{k2}'), Fig.11 ('C_{By}'), and Fig.13 ('S'). 'C_{m1}' and 'C_{m2}' come from the 2.5D simulations with m_i/m_e = 10.0 and m_i/m_e = 200.0 using the same RCS parameters as the one in Fig.10. The dashed line represents a referential spectral line $\sim E^{-4.2}$.

spectrum in the single X-nullpoint simulation shown in Fig.1(d) for the same particle inflow density of 10^{12} m^{-3}. As a result, this would lead again to Buneman instability and formation of turbulence within a short time between the neighbouring magnetic islands (see section 4.5), thus, partially obscuring their periodic structure as reported in 3D simulations by Daughton et al. (2011).

Our results somehow different from some other PIC simulations because we use the open boundary condition for particles allows the most energetic particles to leave the simulation domain. While in the other PIC studies periodic or reflecting boundary conditions are applied (Drake et al. 2006a; Guo et al. 2014). This introduces additional energy mechanisms, which would change the energy spectrum (Zenitani & Hoshino 2001; Drake et al. 2010; Drake et al. 2012; Guo et al. 2014).

One can also note that the spectra of electrons found in the PIC simulations are much softer than those derived for the same conditions in the test-particles studies (Xia & Zharkova 2018). This is because in spite of the static background electromagnetic fields are applied to simulate particle motion magnetic islands, the variable electric fields induced by accelerated particles, like the polarisation one, still change the magnetic field inside the diffusion region, thus affecting the time and energy gains while the particles are confined within the islands.

4.5. Turbulence generated in reconnecting current sheets by accelerated particles

4.5.1. Single X-nullpoint

The trajectories of electron and protons calculated in the RCS near a single X-nullpoint for a strong guiding field B_y reveal a significant difference between the acceleration paths of the

DISTRIBUTION A: Distribution approved for public release. Distribution unlimited

particles with the opposite charges. The particles with different charges are shown separated into the opposite sides from the RCS midplane and then ejected to the opposite semi-planes (Siversky & Zharkova 2009, Xia and Zharkova, 2020, 2021). For a given magnetic topology, energetic electrons can primarily be ejected to the x>0 semi-plane, while protons to the x<0 semi-plane (see Fig. 6).

One important outcome of this separation is the polarization electric fields induced by the separated particles with the opposite charges across the current sheets. This polarisation electric field E_x shown in Fig. 6h is perpendicular to the RCS midplane, and it is much larger than the reconnecting electric field E_{y0} induced by magnetic reconnection process.

As result of this different particle dynamics while moving though a current sheet, the overall distributions of accelerated electrons/protons would have two maxima in energy, or the energy distribution with a 'bump-on-tail' for transit electrons, which can generate turbulence owing to Buneman instability (Buneman 1958). This leads to Langmuir turbulence is produced by transit and bounced electrons in vicinity to a single X-nullpoint in electric (left column) and magnetic (right column) fields (see Fig. 15). It was show for the magnetic field topologies of solar corona the turbulence are, in fact, plasma (Langmuir or Bernstein) waves with the wavelengths of about 2 m and frequency close to the electron plasma frequency for the plasma density of 10^{12} m^2 accepted in the simulations (Drake et al. 2003; Siversky & Zharkova 2009, Xia and Zharkova, 2020, 2021).

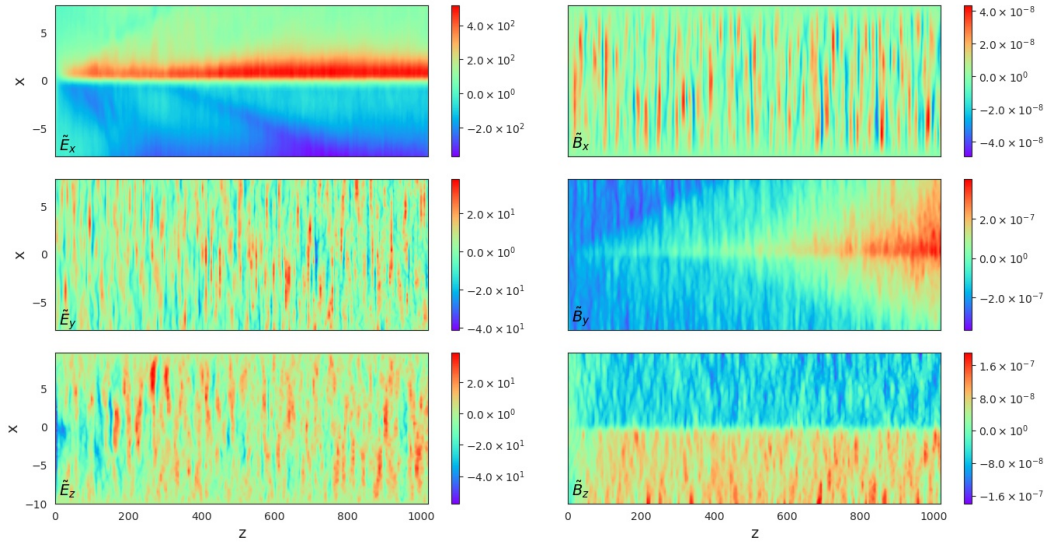


Figure 15. The changes of electric and magnetic fields in the simulation ($n0 = 10^{10}$ m^{-3}): the left column shows the x, y, z components of $\tilde{E}$ (in the unit of V/m), and the right column is for $\tilde{B}$ (in T) at t = $70\Omega^{-1}$.

4.5.2. Multiple X and O-nullpoints

While running PIC simulation for magnetic reconnection we detect multiple small magnetic islands, which are later merged into the island across the periodic boundary. (Zharkova and Xia, 2021b). Due to the periodic boundary conditions at both ends of the z-axis, the

DISTRIBUTION A: Distribution approved for public release. Distribution unlimited

simulation domain represents the RCSs with a chain of magnetic islands, rather than a single X-nullpoint geometry with open exhausts.

In Figure. 16, the power spectra of electric (magnetic) fields of the whole box are measured at t = $32\Omega^{-1}$ as $|E|^2(k)$ ($|B|^2(k)$) in the Fourier space, where k stands for the wavenumber in the reconnection plane (Xia and Zharkova, 2021; Zharkova and Xia, 2021b). The power spectrum of the electric field drops significantly at the spatial scale close to the electron inertial scale (the solid line, $k_{d_e}(n_0)$, and dashed line, k_{d_e} (n_b) , on the right side of the spectra are calculated from the RCS density and background density). It suggests that during the selected time the large-scale waves are quasi-stable. Meanwhile, the spectra show that the electromagnetic energy is strongly damped at the electron characteristic spatial scale.

In this model, the wave-number spectrum of the magnetic field formed a quasi-stable range from $kd_i = 1$ down to above $kd_e = 1$. A least square fitting of $|B|^2(k) \propto k^{\alpha}$ over this range indicates the slope $\alpha \approx -2.7$. The power spectrum of electric field drops significantly at the spatial scale close to the electron inertial scale (the solid line, k_{de} (n0), and dashed line, k_{de} (n_b), on the right side of the spectra are calculated from the RCS density and background density). This suggests that during the selected times the large-scale waves are quasi-stable. Meanwhile, the spectra show that the electromagnetic energy is strongly damped at the characteristic electron spatial scale.

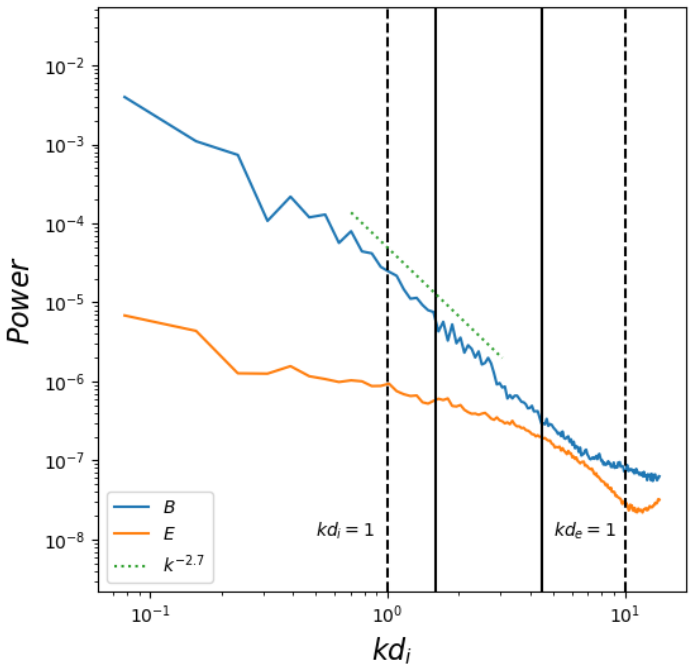


Figure 16. Power spectra of the electric (normalized by $B_0^2V_A^2$) and magnetic fields (normalized by B^2). The wave vector is normalized to d^{-1} of n0. The corresponding k_d (n0), k_d (n0) are marked in dash lines. The solid lines indicate the ion gyroscale k^{-1} (left) and electron inertial scale calculated by the background density k_{de} $(n_b)^{-1}$ (right).

DISTRIBUTION A: Distribution approved for public release. Distribution unlimited

4.5.3. Phase space distributions

As we have shown above, the beams of the same charge gain the `bump-on-tail' energy distributions due to the difference in energy gains between the transit and bounced particles. These beams with two-peak energy distributions can naturally trigger two-stream instabilities leading to the formation of either Langmuir or Bernstein waves depending on the locations where they are generated (Siversky and Zharkova, 2009, Zharkova and Xia, 2021b). Moreover, highly anisotropic energy distributions in the beams, and the presence of a large density gradient between the beams and ambient plasma would introduce other instabilities and generate further plasma turbulence.

We examined the changes in the x-V_y phase space for both ions and electrons along the direction perpendicular to the reconnection midplane at different distances away from the X-nullpoint as shown in Fig. 17.

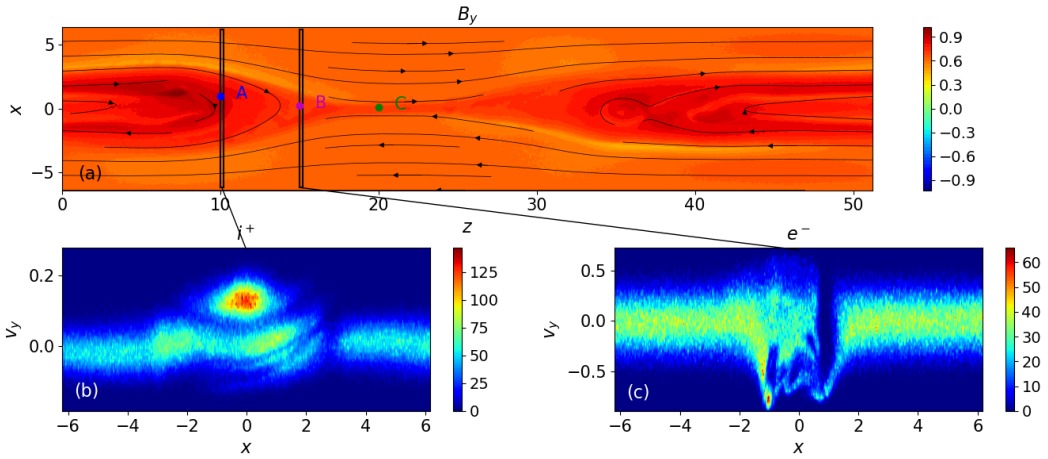


Figure 17. Phase-space distribution functions of the (b) ions and (c) electrons at difference locations at t = $36\Omega^{-1}$. The out-of-plane magnetic field component B_y at y = 0 is coloured in panel (a) with the in-plane magnetic field topology (black solid lines). The electromagnetic fields at A, B, and C are recorded for further analysis. The phase space structures in (b) and (c) are captured in the vertically elongated boxes with a width of $\Delta y = 0.2 d_i$. The main X-nullpoint is located at z = 22, x = 0. This simulation started with a strong guiding field ($b_g = 1$).

The non-Maxwellian feature first showed up in Figure 17c: at z= 15 (or $\Delta z \sim 7$ away from the main X-nullpoint), electron holes are formed in the phase space near x= -1.5 to 1.0, which is triggered by the beam-driven lower hybrid instability.

Then as the inspecting plane moves deeper into the magnetic island, the perturbation in the ion phase space was found at z= 10 (or $\Delta z \sim 12$ away from the X-nullpoint) in Fig.17b, where the arcs in the x= 0 to 2 region represent different groups of ion beams.
We did not find any clear ion holes in the phase space, but those arcs disappear quickly further in the downstream, which suggest the ion beams were scattered by plasma turbulence. Therefore, it suggests that several instabilities dominate different regions as ion beam moves away from the X-nullpoint.

DISTRIBUTION A: Distribution approved for public release. Distribution unlimited

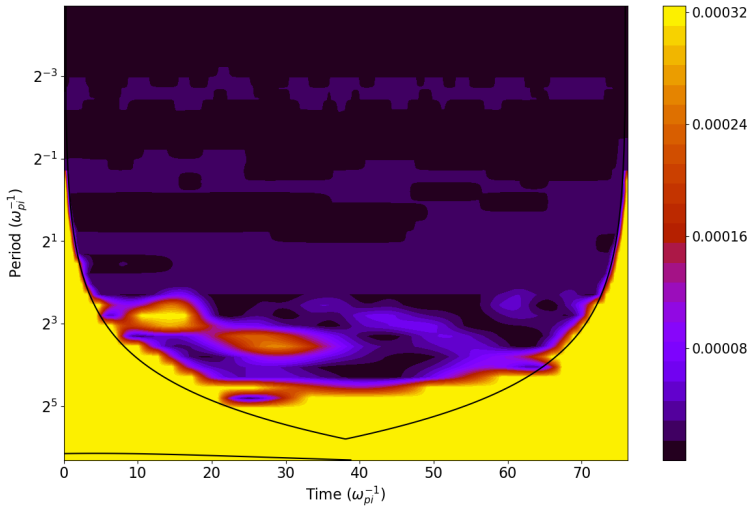


Figure 18. Local wavelet power spectrum of B_x (the purple point B at z = 15, x = 0.25 in Fig. 17) of the time series of B_x components, using Morlet wavelet. The solid dark curve encloses the regions of > 95% confidence.

4.5.4. Frequency analysis

The plasma turbulence introduced by beam instabilities can also be studied using electric and magnetic fluctuations in the frequency domain. After we identified the instability signals in the particle phase space, (Xia and Zharkova, 2021) utilized the discrete wavelet transform (Fig. 18), which is a powerful tool to analyse time-series data collected by a pinpoint in the domain Farge (1992). The wavelet power spectra of both electric and magnetic field components are found to share the similar features with the electron plasma frequency as expected from the results presented in Fig. 17.

Furthermore, by splitting the electric and magnetic fields to the parallel and perpendicular components based on the local mean magnetic field $\mathrm{B_{m0}}$ allows us to distinguish the turbulence in these directions. This local mean magnetic field was averaged over both the space and the time: the surveyed box size was $\Delta L_x(= 0.2d_i) \times L_y \times \Delta L_z(= 0.2d_i)$ surrounding the selected points in Fig. 17; the values were also averaged over $5\Omega^{-1}$. Then the B and E components on every grid are projected to this B_{m0} to get the parallel and perpendicular components. The results are shown in Fig. 19, which were averaged over the Fourier spectra of the electric and magnetic field components from the surveyed grid points.

The surveyed virtual spacecraft was placed at three different locations: A, B, and C in Fig. 9. The selected points C → A are further away from the X-nullpoint. Note that the distributions presented in Fig. 17 are taken from the left-hand side of the X-nullpoint. They are the same as those found at similar distances on the right-hand side because the model is symmetric with respect to the X-nullpoint.

The most obvious changes are in the low-frequency part: right below Ω_{ce}, we found a large enhancement in the amplitude of $B_\perp$ (and a spike in $E_\parallel$), which could attribute to the generation of whistler waves in the region near points A and B. Further down in the lower frequency region, the amplitudes of $B_\parallel$, $B_\perp$, and $E_\perp$ are much larger over a large range. The

DISTRIBUTION A: Distribution approved for public release. Distribution unlimited

small bump near ω_{lh} (especially in the electric fields near point A at z = 10, x = 1. ω_{lh} is the lower hybrid frequency) represents the lower hybrid waves.

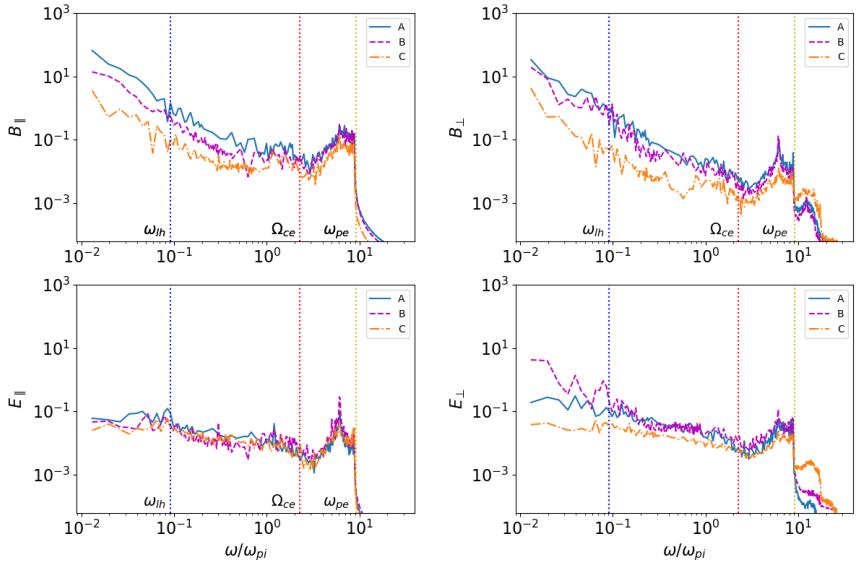


Figure 19. The spectra of different E and B components at selected points (marked in corresponding colours in Fig. 8) as functions of the frequency (normalized to ω_{pi}): $B_\parallel$, $E_\parallel$, $B_\perp$, $E_\perp$ with respect to the local mean magnetic field in 3D. The characteristic lower-hybrid frequency ω_{lh}, electron gyro-frequency Ω_{ce}, and electron plasma frequency ω_{pe} are labelled as vertical dotted lines.

In the very-high-frequency part ($\geq \omega_{pe}$), we first noticed that the perpendicular electric field $E_\perp$ at $f > \omega_{pe}$ is damped significantly as it moves away from the X-nullpoint. In other words, these waves represented by $E_\perp$ are only observable near X-nullpoints. Furthermore, both high-frequency fluctuations of δE and δB are mainly perpendicular to B_{m0}. Further analysis of the fluctuations on the perpendicular plane showed that $E_\perp$, $B_\perp$ are right-hand polarized, which are consistent with electron circular direction in the plane.

In the sub-high-frequency region, $\Omega_{ce} < f < \omega_{pe}$, we found several distinct spikes in all the fields at three locations. Considering that the periodic boundary condition along z−axis stands for simulating a chain of magnetic islands, it suggests that the magnetic island pool is fulfilled with these electromagnetic fluctuations above Ω_{ce}. We will further discuss these signals in the next section. Besides, the enhancement near $f \approx \omega_{lh}$, $f < \Omega_{ce}$, and $\Omega_{ce} < f < \omega_{pe}$ are consistent with the dark horizontal stripes in the wavelet power spectrum (see Fig. 5 in Xia & Zharkova, 2021). Evidently, by splitting the electromagnetic fluctuations into the parallel and perpendicular direction, we managed to identify the differences between these striped signals, which were also appeared in the wavelet analysis in Fig. 10 (Xia & Zharkova, 2021, Zharkova et al, 2021b).

The frequency spectra of electric and magnetic fields obtained at different locations also revealed that turbulence was changing in the outflow from the X-nullpoint to O-nullpoint. The enhanced ultra-high frequency fluctuations in the $E_\perp$ component, e.g. the high harmonics of electron Bernstein waves (Bernstein, 1958; Gusakov & Surkov, 2007), were found to only exist near the X-nullpoint. This is consistent with the MMS observations mentioned above. As the observer moved away from the X-nullpoint, the whistler waves were developing into peaks near the sub-Ω_{ce} (Fujimoto & Sydora, 2008; Muñoz & Büchner,

DISTRIBUTION A: Distribution approved for public release. Distribution unlimited

2016; Graham et al., 2016). These waves could be generated by the temperature anisotropic instabilities (Gary & Karimabadi, 2006) and were also consistent with the electron holes in the phase space (Goldman et al., 2014).

Meanwhile, low-frequency waves dominated the regions further in the outflow. The amplitudes of the fluctuations increased near the lower-hybrid frequency (Rogers et al., 2000). The lower-hybrid waves could be generated by two-stream instabilities as shown in the energy distribution of Figure. 15 (Papadopoulos & Palmadesso, 1976; Siversky & Zharkova, 2009; Zhou et al., 2014; Xia & Zharkova, 2021, Zharkova and Xia, 2021b), or due to the strong density gradient near the separatrices and in the outflow (Scholeret al., 2003; Divin et al., 2015).

4.5.5. Summary

In summary, we have identified the plasma turbulence in the RCS with magnetic islands and linked the characteristic fluctuations to the non-Maxwellian distributions of particles in phase space. The observed waves vary as a function of the distance away from the X-nullpoint. The high-frequency perpendicular fluctuations damp quickly out of the electron diffusion region, and the lower-frequency whistler and lower-hybrid waves are developing because of the streaming instabilities and the strong plasma temperature anisotropy and density gradient.

Identifying these characteristic signals in the observation could indicate the existing scenarios of local particle acceleration during their passage through magnetic reconnection regions in the solar wind (Xia and Zharkova, 2021, Zharkova and Xia, 2021b). This research can be potentially beneficial for the in-situ observations of RCSs near the Sun obtained with the Parker Solar Probe, which has already detected some local reconnection sites during its first encounter (Phan et al., 2020).

4.6. Pitch-angle distributions of accelerated particles

4.6.1. PIC simulations of PADs in different crossings of RCSs

The dual effect of magnetic field topology on particles of the same charge entering reconnecting current sheets from the opposite sides leads not only to very different energy gains by transit and bounced particles but also to different locations where these particles are ejected from the current sheet, or different pitch-angle distributions at ejection.

In the magnetic topology without any guiding field, the plot of V_z vs x and the pitch-angle distributions shown in Fig.20 (a1)-(a4) are quite symmetric with respect to the midplane, x = 0, because the magnetic field topology does not impose any separation by charge. When the low-energy electrons drifting along the midplane, they tend to move along the magnetic field component B_z and, thus, form the pitch-angle distribution towards 0° in $x > 0$ and 180° in $x < 0$ semi plane as shown in Fig.20(a2) due to the magnetization. Note that B is along −z axis for $x > 0$ and along +z axis for $x < 0$). After acceleration, low-energy particles will turn away from the midplane and move anti-parallel to the drifting-in particles (see Fig.1). Thus, the pitch-angle distributions of low energetic electrons peak near 180° in $x > 0$ and 0° in $x < 0$ semi plane in Fig.20(a3). While high-energy particles would move across the midplane in the parallel direction to drift-in particles, e.g. they will have pitch angles peaking at 0°. Therefore, the bidirectional flows of highly energetic particles seen in the heliosphere (Zharkova &

DISTRIBUTION A: Distribution approved for public release. Distribution unlimited

Khabarova 2015) can be these distributions of high-energetic electrons ejected from the different quarters of an RCS occurred at the front of ICME.

With the addition of a noticeable guiding field By, the asymmetry of accelerated particles about the midplane is increased as revealed by their pitch-angle distributions. The transit electrons (protons) become more dominant in the x > 0 (x < 0) semi planes in Fig.20(b3),(c3) (and (b4), (c4) for protons) in the low-energy channel near 180° (0° for protons). Correspondingly, the dispersion of pitch-angle distribution decreases in another semiplane, the high energy particles become focused about particular directions. Furthermore, in moderate guiding field high-energy transit electrons are also shown in the low-energy channel near 180° shown in Fig.20(c2) as they are ejected from the midplane similar to the bounced low-energetic electrons as demonstrated in Fig.6. When the guiding field is very strong, e.g. By/B0 = 1.0, the accelerated electrons and protons are fully separated, the pitch-angle distributions of the oppositely charged particles show a strong asymmetry that can be seen from Fig.20(c2) and (c3).

When a current sheet becomes thicker, the transit electrons gain more energy during acceleration as shown for d = 10 in Fig.20 (d1-d4). On the other hand, when the magnetic field becomes weaker and the current sheet becomes thicker, like in the heliospheric current sheet (HCS), the bounced electrons cannot reach the midplane at all. This is because they become fully magnetized by a strong guiding field and, thus, turn around by 180° well before they reach the midplane.

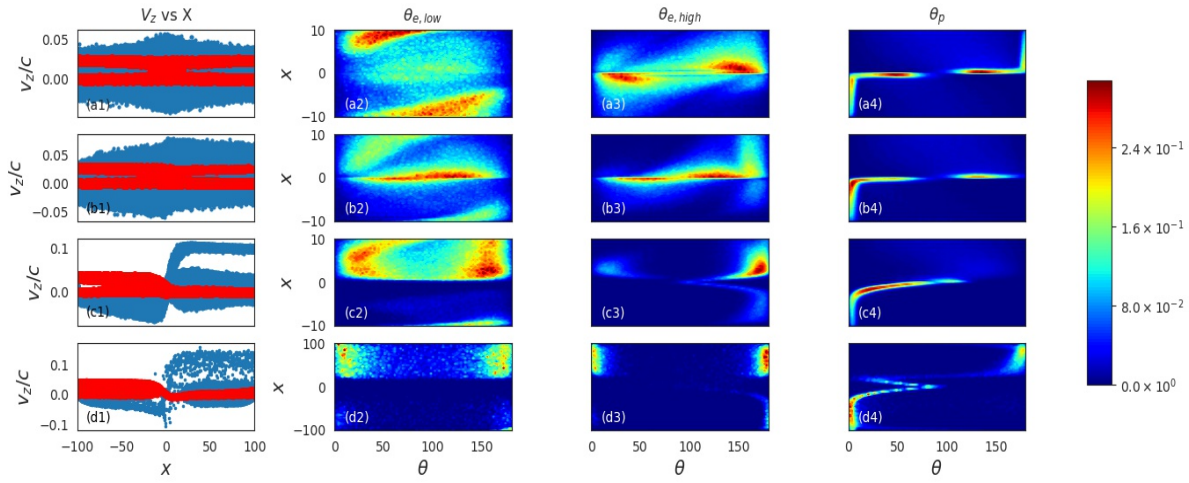


Figure 20. The V_Z vs x distributions in phase space and the pitch-angle distributions for B_Y/B_0 = 0(a-first row), 0.1(b-second row), 1.0(c-third row), and 1.0 with d = 10 (d-fourth row): In each row, V_Z vs x of electrons (blue dots) and protons (red dots) (first column), the pitch-angle distribution of low-energy electrons (second column), the pitch-angle distribution of high-energy electrons (third column), and the pitch-angle distribution of protons (fourth column) are presented from left to right for each individual B_Y/B_0 ratio. The current sheet parameters are $B_0 = 10^{-3}$ T, E_0 = 250 V/m, and d = 1 for (a-c). The magnetic field topology in the reconnection plane is similar to Fig.6.

This property of accelerated particles and their pitch-angles during passing through reconnecting HCS can explain some unusual pitch-angle observations of energetic particles turning away well before the magnetic field reversals in the sector boundaries (Crooker et al. 2004). Fig.20 demonstrates that the electrons with lower energies are turned away from well

DISTRIBUTION A: Distribution approved for public release. Distribution unlimited

before the RCS midplane because of large guiding field magnitudes as it was suggested by Zharkova & Khabarova (2012).

4.6.2. Multi-satellites observations of solar wind particles (WIND, STEREO)

In this project, we show multi-spacecraft observations of suprathermal electrons in a region filled with CSs and MIs and compare the observed PAD features with theoretical predictions made for similar IMF/plasma configurations, using test particle (TP) and particle-in-cell (PIC) approaches proposed by Xia and Zharkova (2018, 2020).

Figure 21 shows the corresponding observations of the key solar wind parameters at ~1 AU. The stream interaction region (SIR) was detected by the L1 spacecraft practically simultaneously with STEREO A (Khabarova et al, 2020), and then the plasma reached STEREO B (Figure 21b). This feature indicates a strong twist of the SIR front with respect to the Parker spiral, since normally it is observed by STEREO B first (Gomez-Herrero et al. 2011). The MI-containing region observed on 2007 May 28-31was characterized by very similar profiles of the key parameters detected by all the spacecraft with an unusually minimal time-shift. Therefore, plasma samples under current study from the centre of the region (May 29, 2007) correspond to the same parameters as reported by Khabarova et al. (2016).

The upper five panels in Figure 22 represent measurements of PADs of suprathermal electrons from the electron electrostatic analyzer (EESA-low), which is a part of the WIND 3DP instrument (http://sprg.ssl.berkeley.edu/wind3dp/). The energies range from middle ~540 eV of undoubtedly suprathermal electrons to low ~29 eV of electrons at the edge between the core and halo electron populations (mainly core). The electron total flux intensities are given by color. MIs can be seen in Figure 12 as intense anticorrelated variations in the IMF components, not stochastic as usually seen in simple turbulent regions, but appearing as humps of approximately an hour in length (more about signatures of MIs can be found in Khabarova et al. 2015, 2016; Khabarova & Zank, 2017). The vertical dashed lines indicate borders of MIs, and each border represents a current sheet. Analyzing the lower (black and white) panels of Figure 12 with IMF and density parameters, one can note that the MIs with the largest IMF strength and the slightly elevated density are observed from ~8 UT. Such conditions lead to intensification of magnetic reconnection in the region. The largest MIs are observed from 13 UT to 22 UT. Overall, the IMF patterns show the presence of smaller-scale dynamic MIs in the left part of Figure 12, the main reconnecting relatively large MIs in the middle, and the larger but more stable MIs in the right part.

The first noteworthy feature is that electrons of different energies behave differently. It is known that usually PAD patterns vary rather slowly from channel to channel even in the disturbed solar wind (e.g., see Kajdič et al. (2013) and Figure 21 of Khabarova et al. 2016), but in this case, the following different features are seen in different channels in Figure 22:

- Electrons in the lowest energy 11 channel closely follow the magnetic topology of smallest and dynamical MIs (see the up-and-down variations occurring in accordance with most intense variations in the IMF).
- The PAD of channel 9 shows a dramatic change in the behaviour of electrons in comparison with lower-energy electrons. Electrons do not orbit the MIs, and the direction of the electron motion shows a clear anticorrelation of variations of pitch angles with respect to the patterns seen in higher-energy channels 7 and 5.

DISTRIBUTION A: Distribution approved for public release. Distribution unlimited

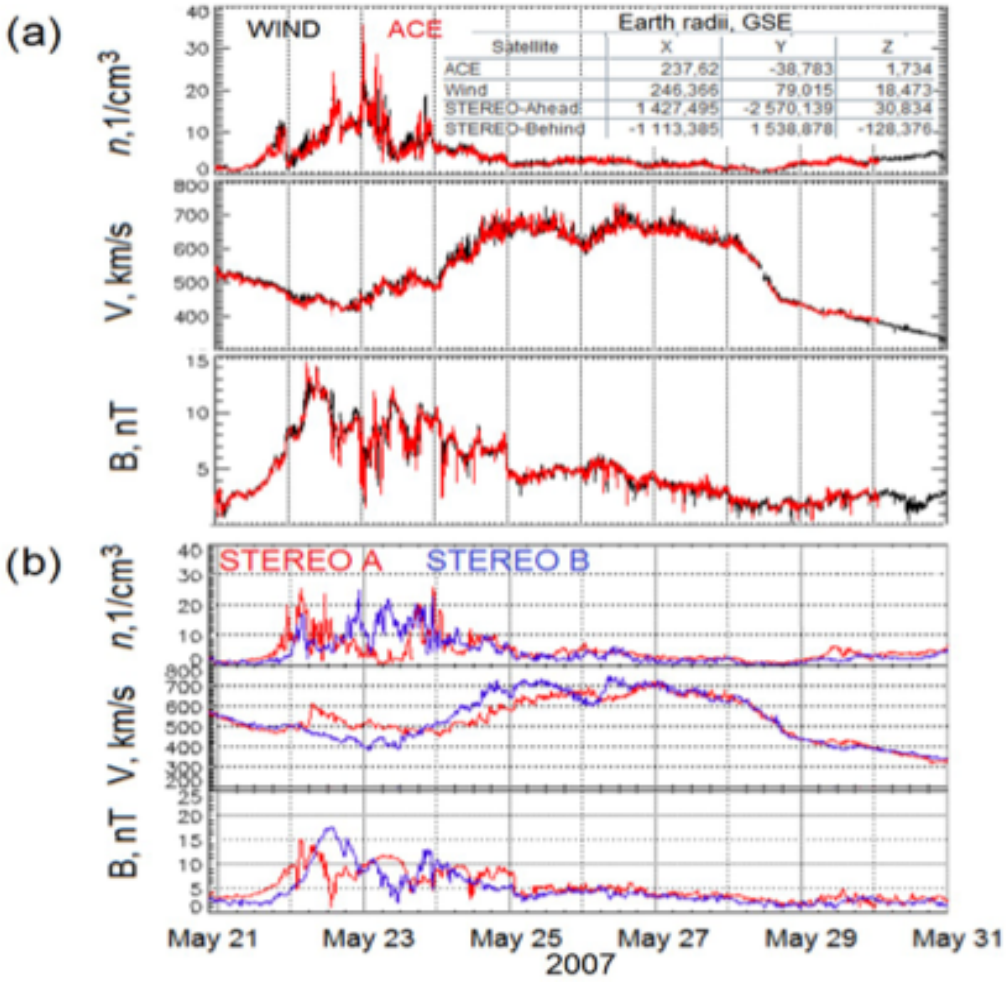


Figure 21. The key solar wind parameters observed by different spacecraft during the passage of the SIR interrupted by the swirl (see Figure 8 of Khabarova et al., 2016) with most magneetic islands observed inside the remnants of the swirl on 2007 May 28–31. Three panels (from top to bottom) show are the solar wind density, the solar wind speed and the IMF strength obtained from the L1 (ACE and WIND) spacecraft (a) and the STEREO A and STEREO B spacecraft (b). The MI-containing region is characterized by very similar profiles of all the parameters observed by the spacecraft with an unusually minimal time-shift. ACE and WIND observations are practically identical, but since ACE have some data gaps, we will use below the WIND measurements to analyse how electrons of different energies behave at crossings of MIs.

DISTRIBUTION A: Distribution approved for public release. Distribution unlimited

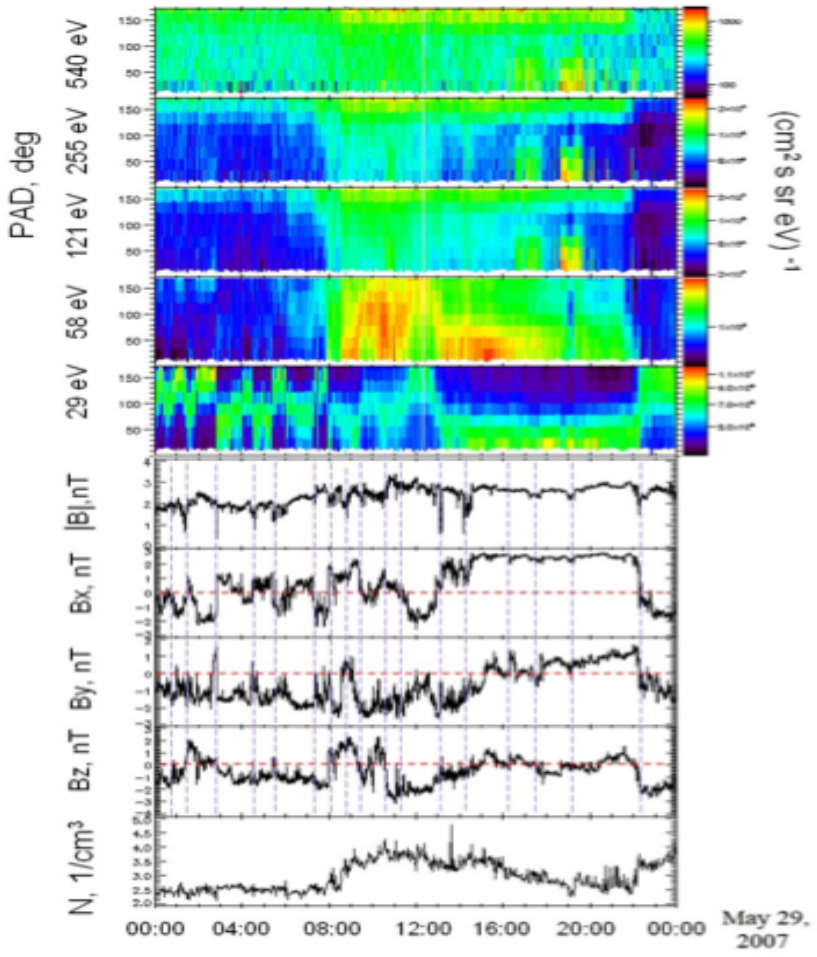


Figure 22. Electron PADs at different energies, the IMF, and the ambient density in the region filled with MIs of variable sizes as observed by the WIND spacecraft on 2007 May 29. From top to bottom: PADs of electrons measured with ~24 s resolution in the following channels: Channel 3 (often ~540 eV); Channel 5 (often ~255 eV); Channel 7 (often ~121 eV); Channel 9 (often ~58 eV); Channel 11 (often ~29 eV); the IMF strength; the three IMF components in the GSE system; and the solar wind density. Crossings of CSs separating MIs are shown by vertical dashed purple lines.

- The PAD of channel 9 shows a dramatic change in the behaviour of electrons in comparison with lower-energy electrons. Electrons do not orbit the MIs, and the direction of the electron motion shows a clear anticorrelation of variations of pitch angles with respect to the patterns seen in higher-energy channels 7 and 5.
- Furthermore, the most intense flux follows the position of the most intensely reconnecting MIs in the middle of Figure 22 (compare the bird-like red PAD pattern and large-scale variations in B_X).
- The channel 5 PAD indicates uninterrupted/smooth strahl flowing in the sunward direction (the colour stripe at the top of the PAD in the left part of the panel) until the approach to the region of the strongest and largest reconnecting MIs in the middle of Figure 2. From ~8 UT, the intense dispersionless vertical feature is seen in the 5-9 channel PADs (green vertical region), and in the area of large and rather undisturbed

DISTRIBUTION A: Distribution approved for public release. Distribution unlimited

MIs there are features of bi-directionality seen in the higher-energy 3-7 channel PADs. The PAD for channel 5 looks similar to channel 7.

- The PAD of suprathermal electrons in channel 3 shows signatures of counter-streaming strahls (red and yellow stripes at 0° and 180°) in the background of the intense dispersionless halo (green).

Observations of higher-energy electrons with the EESA-high instrument were not at as good a level as those provided by EESA-low, which are shown in Figure 22, and higher-energy PAD features were poorly recognizable. Fortunately, obtaining the IMPACT/MAG Magnetic Field and PLASTIC Solar Wind Plasma data from the other spacecraft, the STEREO pair (http://sprg.ssl.berkeley.edu/impact/), allows us to extend the study up to higher possible energies, comparing the available STEREO measurements of the energetic electron direction with WIND observations.

The behaviour of suprathermal electrons in both the lower PAD 73-194 eV panels in Figures 21(b) (STEREO A) and (STEREO B) generally reflects the PAD features seen in the 58-121 eV WIND energy channels in Figure 22 with a corresponding short time-shift. STEREO PAD patterns in the 246.6 eV channel (the middle PAD panels of Figure 23) are consistent with WIND 255 eV PAD in Figure 22 in which the formation of sunward-directed strahl stripe can be observed. The highest-energy 650.7 eV STEREO PAD in Figure 23 is completely different from the other PADs. It shows signatures of intermittent bi- directionality, following the location of MIs and CSs, very similar to the lower-energy PADs of WIND (Figure 22), especially in the region with the largest MIs and the local density increase (see Figure 23b).

Note that the IMF variations observed by the three spacecraft do not coincide with each other since the size of plasmoids produced by the fragmented swirl at 1 AU is too small, and the direction of propagation is too radial to trace each magnetic island with the three spacecrafts. The size of MIs observed by STEREO A (Figure 23a) is generally smaller than that observed by WIND and STEREO B, which is understandable because the main part of the swirl with the smallest-size flux ropes was directed toward the STEREO A position. At the same time, the behaviour of the total IMF observed by STEREO B is rather similar to that seen at L1 because STEREO B is closer to WIND than STEREO A.

4.6.3. Further PAD predictions in CSs with a single X-nullpoint

We trace particles in the vicinity of a 3D current sheet with a half-width of one gyroradius ($d=1.0\rho_i$ along X) extended along Z. B is the static magnetic field induced by magnetic reconnection. B_0 is the maximal magnitude of the magnetic field, and the reconnection electric field E_y accelerating particles is perpendicular to the reconnection plane. Particles from the ambient neutral plasma are dragged into the reconnection region from both sides by the magnetic diffusion process, leaving the RCS only after those gain the critical energy required to break from the magnetic field topology shown in Figure 14a (see details Xia & Zharkova 2018, 2020). After that, particles with opposite charges (electrons versus protons/ions) are ejected into the opposite semiplanes as explained in section 4.2.2.

Particles of the same charge form two distinct groups ('transit' and 'bounced') with very different energies and trajectories (Figure 14a). The maximal energy reached by each population depends on B_y. (Siversky & Zharkova, 2009; Xia & Zharkova, 2018). If B_y/B_0 varies from 0 to 1, bounced electrons (lower-energy electrons, bottom panels in Figure 14b) can be accelerated to energies with the upper threshold from 20eV to 500eV, respectively, while transit electrons gain energies approaching hundreds of keV (higher-energy electrons, upper panels in Figure 24b).

DISTRIBUTION A: Distribution approved for public release. Distribution unlimited

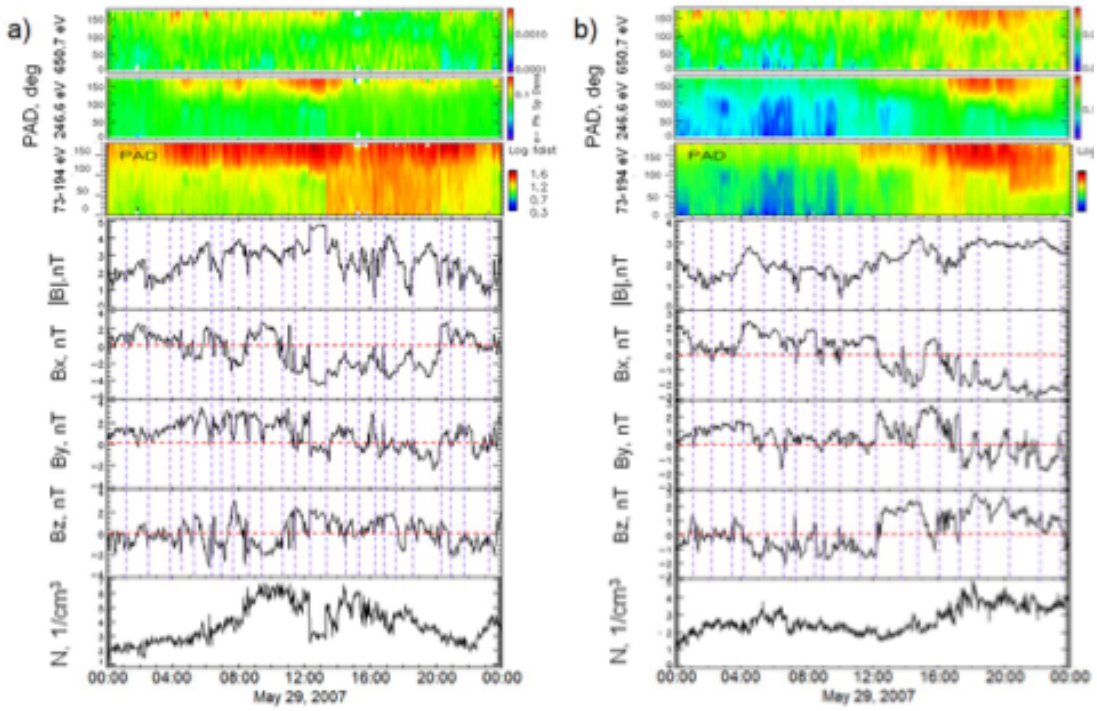


Figure 23. Observations of particle parameters similar to Figure 22, but for STEREO A (a) and STEREO B (b). The upper PAD panels are for the 650.7, 246.6, and 73-194 eV energy channels.

Figure 24b shows that the both populations behave very differently, forming different PAD patterns, which are sensitive to B_y and d. PADs of electrons accelerated in CSs without the guide field $B_y/B_0=0$ are quite symmetric with respect to the midplane, but when B_y increases, asymmetry increases respectively.

If there are dynamical MIs occurring in an RCS, more complex PADs are observed compared to those shown in Figure 24b. Xia and Zharkova (2020) modelled particle acceleration in squashed (contracting) and coalescent (merging) MIs formed in RCSs. The model of a current sheet with multiple X- and O-nullpoints (MIs) is adopted from Kliem (1994) and described in detail by Xia and Zharkova (2020). Here we show an example of a PAD observed by a virtual spacecraft crossing the system of two merging MIs and CSs surrounding them (Figure 25). A complex PAD with a clear signature of bi-directionality is observed within the MIs in the higher-energy channel (the same feature is seen in squashed MIs in a narrower area centered in the middle of an MI – not shown). At the same time, at edges of dynamical MIs, PAD patterns may vary from dispersionless to completely defocused. Lower-energy electrons do not leave MIs showing the most intense PAD profiles at their edges.

DISTRIBUTION A: Distribution approved for public release. Distribution unlimited

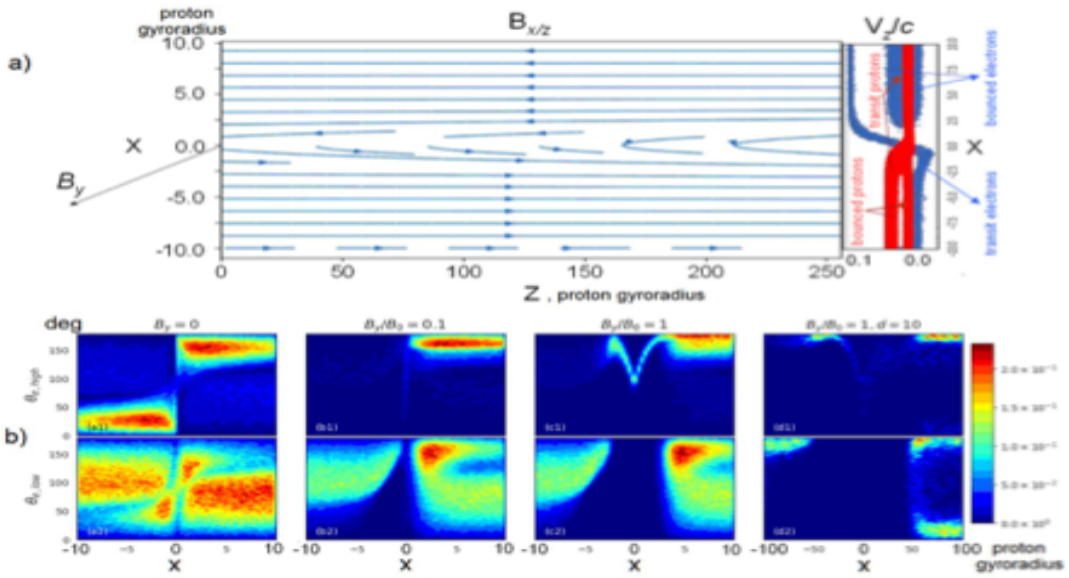


Figure 24. Simulations of acceleration of solar wind electrons to suprathermal energies at the 3D RCS: **a)** Topology of magnetic field lines in the vicinity of the single X-nullpoint of the RCS (on the left), and example of 2.5D particle-in-cell simulations (3D by velocity V and 2D by coordinate) of particle trajectories for the strong guide field, $B_y/B_0 = 1$ (on the right). Bounced particles form clouds at the injection side with respect to the midplane, but more energetic transit particles are ejected into the opposite semiplane. **b)** PADs for electrons with lower energy (bottom row) and higher energy (top row) for the guide field By of different strength: $By/B_0 = 0$ (first column, weak guide field), 0.1 (second column), and 1.0 (third column, strong guide field). RCS width d=1.0 ρ_i (thin RCS) in the three columns, $B_0 = 10^{-9}$T. The fourth column is given for comparison under condition of thicker RCS and strong guide field ($By/B_0 = 1$, d=10 ρ_i).

4.6.4. Interpretation of PAD features in MIs observed with PSP

PADs of electrons observed in realistic plasmas containing numerous X-nullpoints and MIs are far more complex than the simulations provided above because the final picture formed by accelerated particles is determined by the magnetic field topology and the reconnection rate, which depend on the magnitude of the guide field, the dimension of RCSs and MIs, and the plasma density. Nonetheless, knowing that all the effects are cumulative, some of the key points of Figure 22 and Figure 23 can be easily understood from Figure 24b and Figure 25.

DISTRIBUTION A: Distribution approved for public release. Distribution unlimited

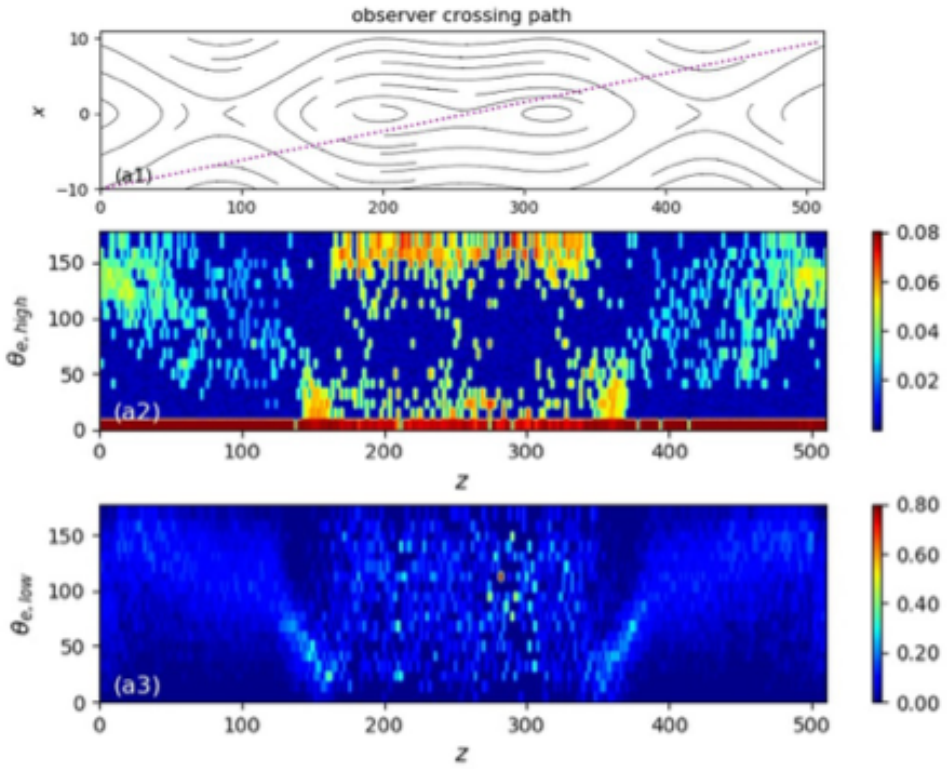


Figure 25. PADs observed when a hypothetical spacecraft crosses two coalescent MIs. The top plot presents the magnetic field topology (black lines) and the paths of a spacecraft (purple line). Middle and bottom colour plots present the PADs of higher (middle) and lower (bottom) energy electrons accelerated in the system of the islands and CSs. Parameters of the islands employed are $B_0 = 10^{-9}$T, E_0 = 0.100m V/m, By/B_0 =0.1, d = $2\rho_i$. k=L/d= 0.0325. L is the half length of the island, d is the current sheet half-thickness. Both counter-streaming strahls and dropouts may be observed in such a configuration.

The electrons in the upper left PAD of Figure 14b are ejected mainly along 0°-180°, and the RCS midplane is clearly visible as a vertical stripe. This PAD pattern is often observed in the solar wind (see Figure 22 and Figure 23) but has always been interpreted in terms of crossing of the HCS or a similar current sheet connected to the solar source. This study shows that such a pattern just reflects a crossing of a single thin current sheet reconnecting in a weak guide field. A bird-like pattern seen especially clearly in the middle of the right panel of Figure 13 and in Channel 9 of Figure 22 indicates a crossing of the CS reconnecting in a strong guide field. According to Figure 14b, it is not expected to be seen in lower-energy channels.

Figure 24b and Figure 25 suggest that an intense unidirectional PAD stripe is formed in the areas with bigger MIs (Figure 22 and Figure 23) because electrons can be accelerated to higher energies in bigger MIs, propagating much further from the initial acceleration sites (X- nullpoints or MI pools) and gradually becoming strahls that mix with solar-origin strahls and contribute to the total PAD picture in the middle- and higher-energy channels.

DISTRIBUTION A: Distribution approved for public release. Distribution unlimited

Counter-streaming electrons appear naturally in the lower-energy channel of Figure 24b when the guide field is rather strong, and a huge dropout encompassing the midplane is seen in the three bottom panels (lower energy electrons) and the top right panel (higher energy electrons, strong B_y, and the wide RCS). Finding this important PAD feature easily solves the mystery of the observation of numerous narrow dropouts associated with CSs in the solar wind. PAD simulations presented in Figure 24b allow us to suggest that the occurrence of dropouts and their properties are mainly determined by the width of RCSs and the reconnection rate.

Figure 25 also shows a clear signature of bi-directionality of higher-energy strahl electrons trapped and reaccelerated in dynamical MIs, while lower-energy electron paths are less structured. Wide dropouts are seen mainly in Figure 25 in the area free of merging MIs. It is noteworthy that bi-directionality and dropouts in PADs can be observed in the cases of both relatively low and high energies. Therefore, such PAD features can be determined by properties of a particular RCS or MI region of any origin. The lower-energy PAD in Figure 12 (the lower colour panel) shows the rotation of the direction of the electron flux in the area of dynamic MIs separated by CSs. Figure 25 suggests that this is the case when lower-energy electrons cannot leave dynamical MIs and would trace the local IMF topology instead.

Therefore, some of the heat flux dropout and bidirectional strahl events can be explained by local dynamical processes involving magnetic reconnection. The most essential specific point derived from this interpretation is that, according to simulations, lower- and higher-energy electrons produce differently appearing PADs, which suggests that such a difference in PADs observed in higher- and lower- energy PAD channels is a signature of the local particle acceleration in current sheets with or without magnetic islands.

Parker Solar Probe (PSP) observations

This point was further explored by investigating the observations by Parker Probe payload (Zharkova and Xia, 2021, A&A). Most recently, during Perihelion 1 of Parker Solar Probe (PSP), 21 RCSs have been identified by the paired rotational discontinuities bounding the exhausts (Phan et al. 2020). Although, due to the low resolution (≥ 27s) of the spacecraft PAD measurement at this moment, PSP could only sample 0 − 4 times in the RCS, or even record < 2 samples during the surveyed time. Still, we are able to identify two events (ID 7 and 15 in the table of Phan et al. (2020)) showing the electron PAD patterns near a single X-nullpoint.

PADs measured by PSP in different energy bands and the change of magnetic field components are shown in Figure. 26 (a1, a2) (Zharkova and Xia, 2021). The period of the first RCS crossing is 65.7s, and the guiding field was weak (0.82 nT). The electron beam streaming from the Sun (Kasper et al. 2019) is locally discontinued. The reversing of the mono-directional strahls from 180° to 0° across the RCS is presented in the higher-energy channels > 253 eV, which is consistent with Fig. 27b.

The second case is presented in Figure. 26(b1, b2). It shows a heat-flux dropout in the higher-energy channel (> 55 eV) (Zharkova and Xia, 2021). The unidirectional strahl at 180° could be a combination of local accelerated electrons and the electron beams from the Sun. Meanwhile, the transition of mono- to bi-directional beams in the lower-energy (< 45 eV) matches rather closely to the features of PADs presented in Fig. 28b. Since the observed guiding field was rather weak (0.89 nT), while the simulation in Fig. 28b was made for a stronger guiding field, this good fit is likely to be caused by an increase the current sheet width to $100\rho_i$, for which the previous single X-nullpoint simulation was carried out.

DISTRIBUTION A: Distribution approved for public release. Distribution unlimited

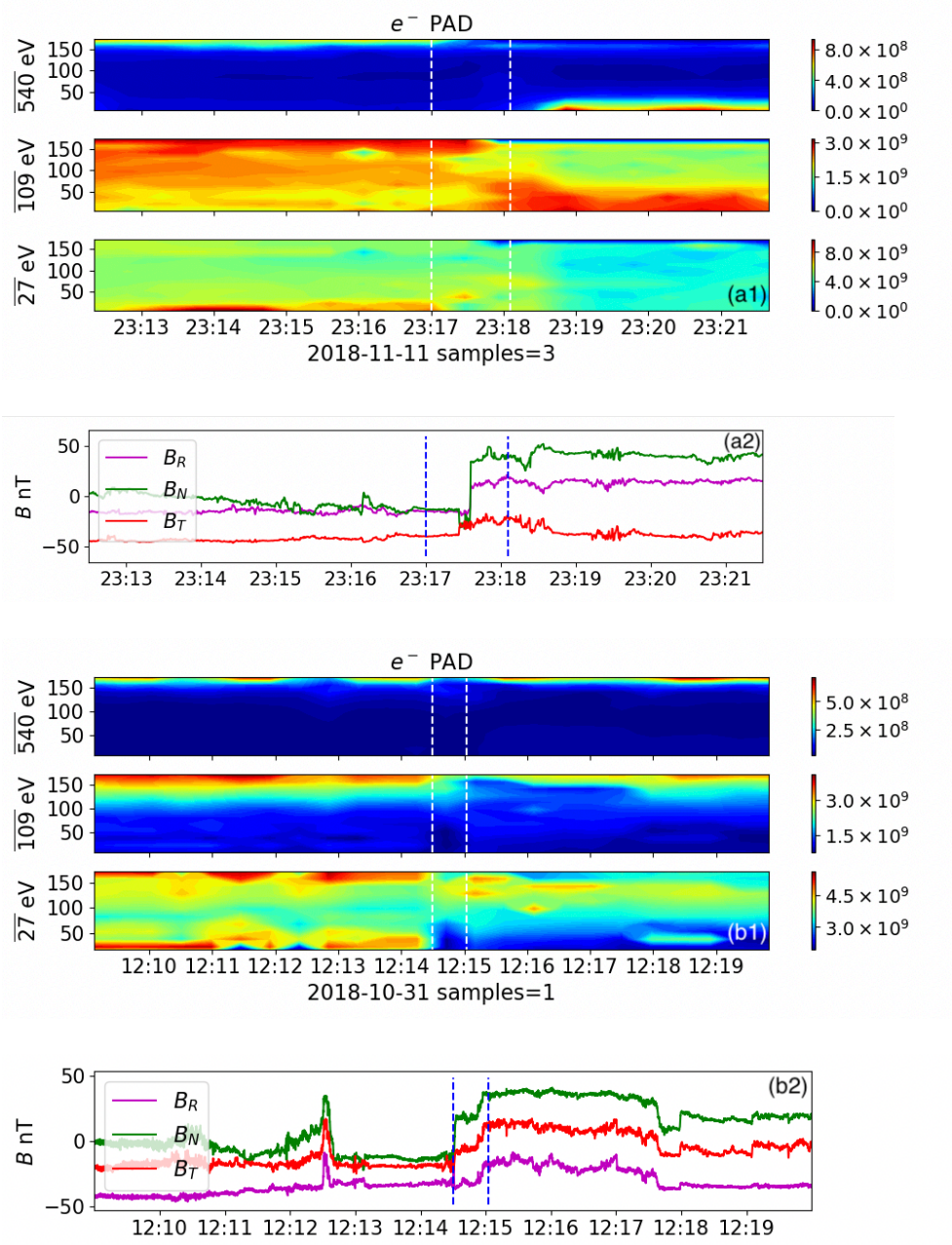


Figure 26. PSP observations: The electron PADs averaged over 253.3 − 934.2, 55 − 164.6, and 9.7 − 44.3 channels from top to bottom. The two top panels come from the event of 11 November 2018 and two bottom panels come from the event of 31 October 2018. The bottom panels in each event show the magnetic field components in the RTN coordinate. The vertical dashed lines mark the crossing of the RCS.

Also, it has to be emphasised that the energy threshold for lower- and higher-energy electrons, when their PADs become qualitatively different, is ~ 50 eV. This is smaller than the value of ≥ 100 eV obtained from the measurements near 1 AU in the solar wind (Khabarova et al. 2020), which suggests the reconnection event in the RCS measured by PSP was weaker.

DISTRIBUTION A: Distribution approved for public release. Distribution unlimited

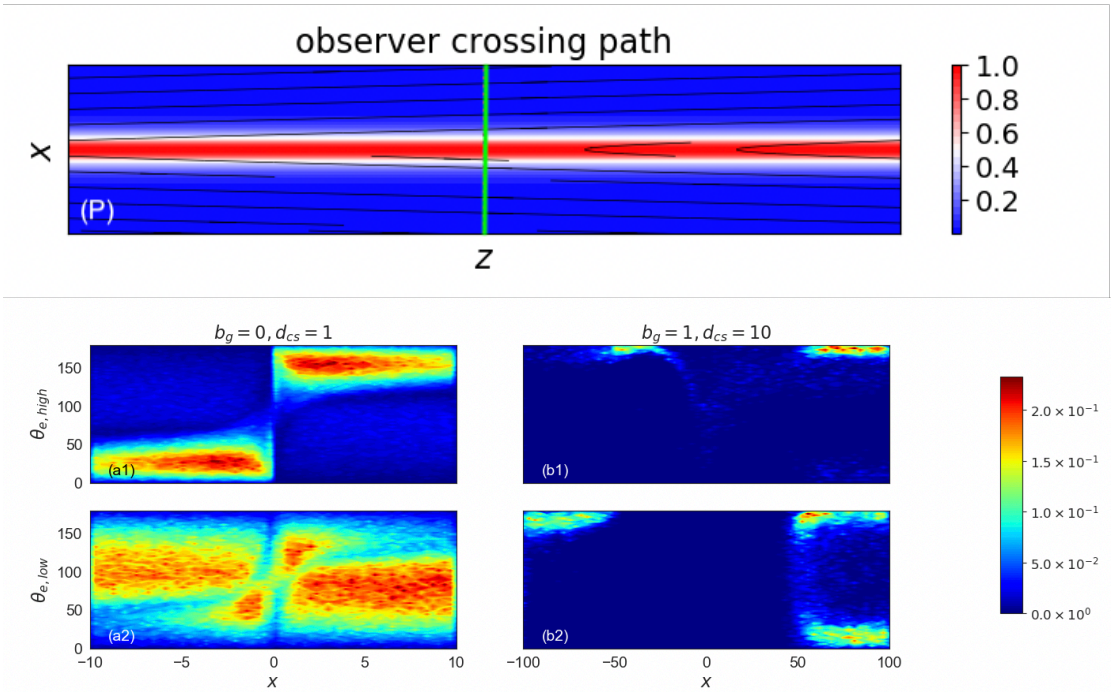


Figure 27. Electron PADs observed when a hypothetical spacecraft crosses the RCS with a single X-nullpoint. The top panel (P) shows that the sampled crossing path of the spacecraft is perpendicular to the RCS midplane (green solid line). The in-plane magnetic field topology is drawn in black lines with the amplitudes of B_Y (b_g = 1 case) coloured as the background. The PADs of high-energy electrons (second row) and lower-energy electrons (third row) for the guide field b_g = 0 (a1, a2) and b_g = 1 (b1,b2). obtained from (a0) are presented in (a1) and (a2). The PADs shown in (b1) and (b2) (b_g = 1) are recorded along the same path as in (a1) and (a2) with the virtual spacecraft crosses an RCS with no guiding field (b_g = 0).

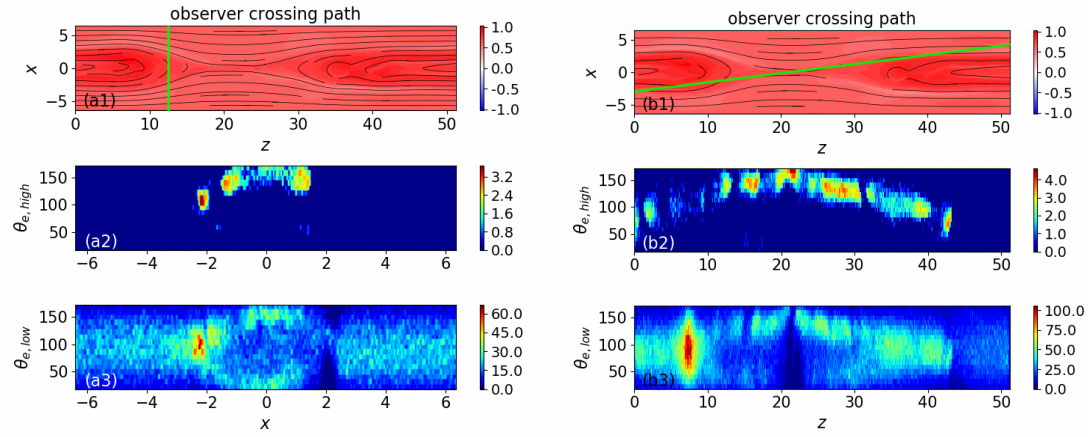


Figure 28. PADs observed by a virtual spacecraft in the simulation starting with a strong guide field (b_g = 1) at t = 33Ω_i: left column: the path perpendicular to the midplane x = 0, right column: the path across the separatrices. The magnetic field and the paths of the spacecraft (green lines) are demonstrated in the top row. Middle and bottom rows present the PADs of higher- and lower-energy electrons observed on the paths.

There are also a few other examples of simulations of the electron PADS seen under different paths of spacecrafts across magnetic islands presented in the paper by Zharkova and Xia, 2021, which can be useful for the interpretation of electron PADs observed in the heliosphere in the future.

DISTRIBUTION A: Distribution approved for public release. Distribution unlimited

4.7. Particle transport models and their comparison with observations

4.7.1. General introduction

The complex processes of plasma heating in solar flares are associated with a primary release of magnetic energy via magnetic reconnection occurring in the corona (Priest & Forbes 2000; Somov 2000) and subsequent acceleration of energetic particles (Vilmer et al. 2011; Zharkova et al. 2011) precipitating along newly reconnected field lines (Holman et al. 2011; Kontar et al. 2011). These processes happen on a very short timescale during flare onset and can be effectively diagnosed from the increase of intensities in flaring emission of hard X- rays (HXR), γ-rays (GR), soft X-rays (SXR), extreme ultra- violet (EUV), ultra-violet (UV), microwave (MW), and optical emission (Zharkova 2008; Matthews et al. 2015, and references therein). Energetic electron beams precipitating into the flaring atmosphere (Brown 1971; Syrovatskii & Shmeleva 1972) can account for HXR and MW emission (Holman et al. 2011; Kontar et al. 2011) while proton and ion beams (Vilmer et al. 2011) can account for observed γ-ray emission. The scenarios by which the magnetic field is reconfigured while triggerng flaring events and converting the energy of magnetic field into radiation and macro-motions in flares are to a large extent defined by the initial magnetic field topologies of interacting loops and the trigger mechanisms that initiate the reconnection process in each flaring case (Priest & Forbes 2000; Somov 2000).

Soft X-ray emission caused by the ambient plasma heating by particle beams produces emission in highly ionised elements, including for example Fe XXIV and Fe XXV ions (Porquet et al. 2001; Kawate et al. 2016), and often shows a longer (hours) duration. Furthermore, there are observed blueshifts in SXR and EUV emission with upward velocities of up to 1000 $km \cdot s^{-1}$ (Antonucci et al. 1982; Milligan et al. 2006a,b; Del Zanna 2008; Milligan & Dennis 2009; Polito et al. 2016). In addition, observations of Lyman-α lines by the instruments with low spatial resolution show impulsive brightening of Lyman line emission and the appearance of either red or blue wing asymmetries at different times of flare development (Procha´zka et al. 2017; Druett & Zharkova 2018; Dominique et al. 2018). This is also supported by brightening in Lyman continuum intensity, which becomes greatly enhanced from the continuum head at λ = 910 Å along the other wave- lengths (Kleint et al. 2016; Druett & Zharkova 2019), resulting in strong intensity flattening over the continuum wavelengths reported from observations (Machado et al. 2018; Druett & Zharkova 2019).

Simultaneously, with HXR bursts, gamma rays, SXR, and EUV emission growth, the dynamics of flares in the lower atmosphere can be effectively derived from the observations of optical lines and, in particular, hydrogen Hα line 6563Å emission revealing large redshifts up to 4-5 Å (Ichimoto & Kurokawa 1984; Canfield & Gayley 1987; Zarro et al. 1988; Wuelser & Marti 1989), followed at later times by blueshifts as observed in stellar flares (Houdebine et al. 1990; Houdebine & Doyle 1994). In addition, notable increases in white light (WL, or Paschen continuum) emission (Uchida & Hudson 1972; Kurokawa et al. 1988; Matthews et al. 2011; Procha´zka et al. 2018), Balmer and near-UV continuum emission (Kleint et al. 2016; Kotrcˇ et al. 2016; Druett & Zharkova 2018; Procha´zka et al. 2018) are often observed during early phases of flares. The locations of WL or Balmer continuum emission are nearly co-spatial with the contours of HXR emission and have close depths of formation in flaring atmospheres (Druett & Zharkova 2018). Uchida & Hudson (1972) suggested that energetic elec- tron beams injected into a flaring atmosphere can account for the temporal correlation of HXR and WL emission. Later, Aboudarham & Henoux (1987) proposed that WL emission can be mainly produced by negative hydrogen ions at very deep dense photospheric levels. However, the precise mechanisms responsible for the enhancement of WL emission in flares has remained an active topic for debate for three decades. Only recently, Druett & Zharkova (2018) showed

DISTRIBUTION A: Distribution approved for public release. Distribution unlimited

that non-thermal ionisation of hydrogen atoms by relativistic electron beams can naturally produce strong increases in Balmer and Paschen (WL) emission during flares at chromospheric levels expanding from photospheric depths where this emission is expected to originate in the quiet Sun.

In addition, particle beams cause a large increase in collisional ionisation and excitation of hydrogen atoms by non- thermal electrons, which strongly (by orders of magnitude) in- creases excitation and the ionisation degree of hydrogen atoms from all atomic levels (Zharkova & Kobylinskii 1993). These non-thermal collisions combined with plasma heating caused by beam electrons can lead to an increase in hydrogen line and continuum radiation in Lyman, Balmer and Paschen series. This suggestion was recently tested with detailed radiative hydrodynamic simulations using the HYDRO2GEN code including non-thermal excitation and ionisation by beam electrons (Druett et al. 2017; Druett & Zharkova 2018, 2019). The authors confirmed the enhancement of Lyman, Balmer, and Paschen lines and continua of hydrogen atoms in flares caused by beam electrons. Druett & Zharkova (2019) showed that after the beam is switched off, the high ionisation degree of a flaring plasma gained during the beam injection is sustained for a very long time by Lyman continuum emission because of its large opacity. This leads to a long enhancement of hydrogen ionisation in the flaring atmosphere and an increase of the Lyman -α and β line emission in the line cores and wings. The earlier wide-spectral filter observations with large (2-4 Å) red shifts (e.g. Ichimoto & Kurokawa 1984; Wuelser & Marti 1989) can- not be seen by modern instruments with narrow (2×1.5Å) spec- tral windows (Druett et al. 2017; Druett & Zharkova 2018), which explains the frequently reported delays of the order of 30 s between maximum HXR emission and the appearance of Hα-line emission in powerful flares (Kaempfer & Magun 1983; Veronig et al. 2002; Radziszewski et al. 2011).

Strong high-energy emissions in HXR, EUV, UV, and WL wavelengths are often accompanied by the occurrence of sun- quakes or ripples on the solar surface radially emanating from a point source from 20-60 minutes after a flare onset (Kosovichev & Zharkova 1998; Zharkova & Zharkov 2007; Zharkova 2008; Donea 2011; Zharkov et al. 2011a; Zharkov et al. 2011b; Matthews et al. 2015). Sunquakes are detected on the solar sur- face using time–distance (TD) diagram analysis (Kosovichev & Zharkova 1998) and acoustic holography (Donea et al. 1999; Lindsey & Braun 1999; Donea et al. 2000; Lindsey & Braun 2000; Donea & Lindsey 2005). The sunquake origin is nor- mally indicated by a compact bright kernel (source) peaking during a flare, which is verified by statistical tests (Zharkov et al. 2011a). Sunquakes have been detected in X-class (see e.g. Kosovichev & Zharkova 1998; Zharkova & Zharkov 2007; Moradi et al. 2007), M-class (Donea et al. 2006), and even in C- class (Sharykin et al. 2015) flares, while the most powerful sun- quakes appeared to be associated with M-class flares (Donea 2011). The ripples are suggested (Kosovichev & Zharkova 1998; Zharkov 2013) to be reflections from the solar surface of acoustic (in some cases, magneto-acoustic) waves induced by a sharp deposition into the solar interior of the momentum delivered by hydrodynamic shocks formed in flaring atmospheres. Some localised magnetic configurations are found to be more effective in channelling the energy and momentum to the lower atmosphere (Green et al. 2017).

The mechanisms responsible for the generation of sun- quakes are still under investigation. The first of the mechanisms proposed for generating sunquakes was a hydrodynamic response of flaring atmospheres to the injection of energetic particle beams (Kosovichev & Zharkova 1998; Zharkov 2013; Macrae et al. 2018), which produces strong hydrodynamic shocks travelling downward to photospheric levels at super- sonic speed (Somov et al. 1981; Fisher et al. 1985c,a; Allred et al. 2005; Zharkova & Zharkov 2007; Zharkova & Zharkov 2015). Some authors have also suggested radiative back- warming as a source of pressure transients that can produce acoustic waves (Donea et al. 2006; Donea 2011). However, observations show that some sunquake locations are associated with little or no white light emission, and little or no HXR emission (Matthews et al. 2011; Buitrago-Casas

DISTRIBUTION A: Distribution approved for public release. Distribution unlimited

et al. 2015; Zharkov et al. 2011a). Hudson et al. (2008); Fisher et al. (2012) noted that sunquakes often occur in the locations of Lorentz force transients, which can produce a well-directed magnetic impulse of Poynting vector towards the photosphere and subsequent magneto-acoustic wave conversion (Cally 2006; Hansen et al. 2016).

Recently, Macrae et al. (2018) detected a sunquake in the flare of 6 September 2011, which was previously reported to be acoustically inactive (Liu et al. 2014). Subsequently, the authors (Macrae et al. 2018) provided a quantitative interpre- tation of the properties of the sunquake (timing, directional- ity) using a hydrodynamic model for plasma heating by beam electrons as an input for the hydrodynamic model for acoustic wave propagation in the solar interior. They demonstrated that all three mechanisms associated with the generation of seismic signatures are present in flaring atmospheres if they have sunquakes.

The energetic particles gain their energy from a reconnecting current sheet formed during a flare by converting the magnetic energy into particles with the help of Lorentz force. Also, the same relativistic electrons over-ionise the ambient hydrogen plasmas by five to six orders of magnitude and keep it in this state for a very long time for up to 40 minutes by the ra- diative transfer in optically thick Lyman continuum (Druett & Zharkova 2019) leading to the appearance of white light emission (Druett & Zharkova 2018).

On 6 September 2017 the active region NOAA 12673 produced two X-class flares: an X2.2 flare and three hours later an X9.3 flare, which have been studied by many authors. A few sunquakes associated with the X9.3 flare were originally reported by Sharykin & Kosovichev (2018). Further helioseismic analyses of magneto-acoustic waves in this active region were carried by Zhao & Chen (2018), who also discovered fast and slow magneto-acoustic waves that occurred prior to the major sunquakes and travelled through this active region. Similar waves were also seen in Ca II line spectral observations by the Swedish Solar Telescope (SST), as recently re- ported by Quinn et al. (2019), who linked these Ca II waves to the largest sunquake. Keeping in mind that maximum Doppler velocities of the first bounce of these acoustic waves formed in the interior measured from the HMI dopplergrams do not exceed of ±3 km/s at the photosphere as reported by Sharykin & Kosovichev (2018), it is important to establish, whether these or other waves can reach the heights of the chromosphere to produce the Ca II waves seen by Quinn et al. (2019). Alternatively, these chromospheric Ca II waves may be linked to the slow magneto-acoustic waves seen in the HMI dopplergrams prior the sunquake onsets as reported by Zhao & Chen (2018).

Both flares produced very extensive white light emission in the shape of ribbons (Romano et al. 2018). All authors re- ported a complex magnetic structure for the active region and the non-linear force-free field (NLFFF) reconstruction of the magnetic field in this active region prior to the X2.2 flare. In order to restore magnetic configuration at the start of X9.3 flare, three-dimensional MHD simulations were carried out (Inoue et al. 2018) revealing that there were three magnetic flux ropes (MFRs) formed after the X2.2 flare and just prior to the X9.3 flare. These MFRs are very likely to be associated with sun- quakes as discovered earlier by Zharkov et al. (2011a); Green et al. (2017).

In this project we compared the available multi-wavelength observations and multiple sunquakes in the flares of 6 September of 2011 (maximum of solar activity) and 6 September 2017 (minimum of solar activity) and provided interpretation of this emission and detected sunquakes with the radiative hydrodynamic model HYDRO2GEN.

4.7.2. Observations of the X2.1 flare of 6 September 2011

4.7.2.a. Magnetic structures

Active region (AR) NOAA 11283 produced two X-class flares 94 that have been well studied by many authors, including the prop- 95 erties of associated flare emission (Xu et al. 2014), the observed 96 magnetic field changes (Liu et al. 2014; Petrie 2016) and flare 97 energetics (Feng et al. 2013). The

DISTRIBUTION A: Distribution approved for public release. Distribution unlimited

X2.1 class flare occurred on 98 September 6, 2011 and was the first of two WL homologous flares produced by this region. None of the authors listed above have detected seismic signatures associated with the flare.

Observationally, the X2.1 flare starts with the activation of an S-shaped sigmoid, representing a flux rope, as seen in the 94 Å AIA data (Fig. 18a). During flare onset (22:18:37 UT) one observes two flaring loops and a circular H-alpha ribbon (Fig. 1b), similar to that reported by Kawate et al. (2016). NOAA 11283 undergoes a period of flux emergence prior to the September 6 flare leading to fan-spine reconnection initiating the flare (Jiang et al. 2014). This process leads to repeated eruptions with a stronger eruption occurring to the south at 22:19 UT, followed by the ribbons that form a circular structure, as expected from a reconnection at the null point of the fan-spine configuration (Janvier et al. 2016). Using NLFFF extrapolation and MHD simulations, the sigmoid eruption was shown to proceed due to the torus instability (Jiang et al. 2013). This flux rope eruption signalled the possible occurrence of a sunquake as first noted by Zharkov et al. (2011a) for the flare of 15 February 2011.

4.7.2.b. X-rays, H-alpha and white light (WL) flare emission

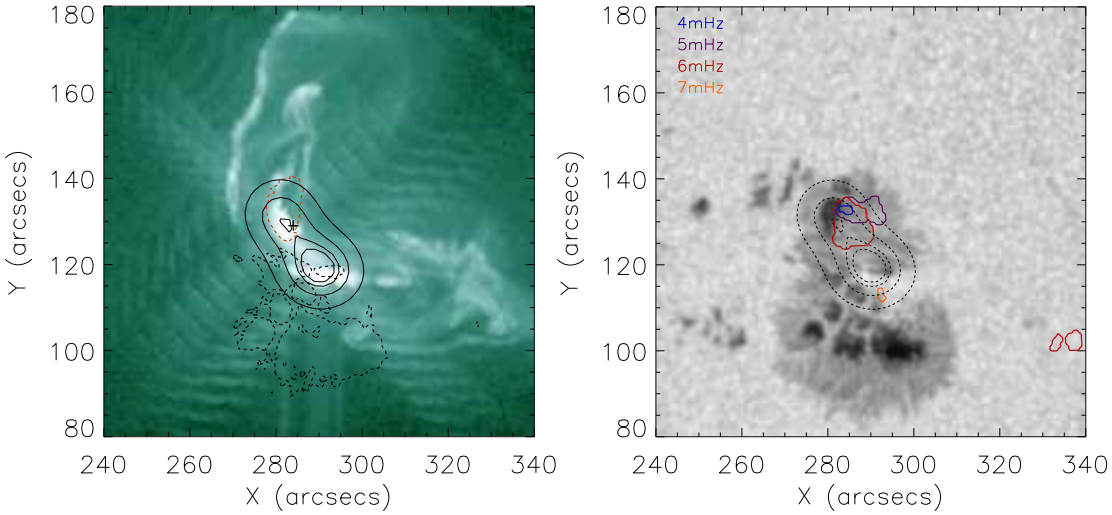


Figure 29. Left: The AIA 94 Å images at 22:10 UT with an s-shaped sigmoid and flux rope prior to flare onset with the two flaring loops and circular ribbon formed during the flare (22:18:37 UT). Red and Black contours denote 500 and 500 Gauss LOS magnetic field respectively. HXR emission at 50100 keV (solid contours) highlights two closely spaced sources in (*panel b*), with TD source (black cross) located close to the northern HXR source. Right: The context images of both HMI continuum and LOS magnetogram at 22:18:37 UT are given with detected source location contours from the statistical test on full-angle egression power maps. Regions of a significant acoustic signal are given for the 4–7 mHz pass bands, in addition to the location of the time–distance source origin. HXR emission is represented as dashed contours.

There were two closely separated sources of 50-100 keV HXR 23 emission during the flare, co-spatial to the observed WL kernels. However, it is the northern kernel with weaker emission where we detect the acoustic source (Fig. 18c and 18d) previously missed by the other authors (Liu et al, 2014).

In order to extract HXR parameters required for modelling the hydrodynamic response, spectral fitting across the flare duration is carried out using Object Spectral Executive (OSPEX) for RHESSI data from all collimators from 2 and 7. To retrieve an initial electron flux and spectral index we select the time period 22:18:16–22:18:36 UT, during the quake onset (interval 20, see Fig. 30, right top plot), and fit using a variable thermal (green) and thick-target bremsstrahlung (yellow) component. The resultant two-component fit (red) is made

DISTRIBUTION A: Distribution approved for public release. Distribution unlimited

over the energy range 12–270 keV, dictated by the detector's attenuator state and the drop to background levels of photon flux. Background levels are determined from RHESSI night time prior to the event. From the fit displayed in Fig. 30, we extract the following initial parameters: the initial energy flux F_0 = 4.3 10^{11} erg cm^2 s^1 and spectral index = 3.5. The second HXR peak occurred at 22:19:20UT, where a similar fitting procedure provides the following parameters: F_0 = 3.7 ↠ 10^{11} erg cm^2 s^1 and spectral index = 4.0.

Moreover, in these two regions there is enhanced WL emission (WL kernels 1 and 2) observed during the flare onset, or its impulsive phase, which is co-spatial with the velocity and LOS magnetic field transients (Fig. 30 left column). The WL kernel brightening appears at chromospheric and photospheric levels at 22:10UT (Xu et al. 2014) quickly evolving into flare ribbons that grow to full-length by 22:18UT (Fig. 29a and 29b). As the two ribbons evolve almost perpendicularly to each other, another circular ribbon encircles the two ribbon structure (Janvier et al. 2016; Kawate et al. 2016). Averaging over the seismic source location one can see that all the transients and WL emission are co-temporal with one another, situated prior to SXR peak and between the dual HXR peaks (Fig. 30).

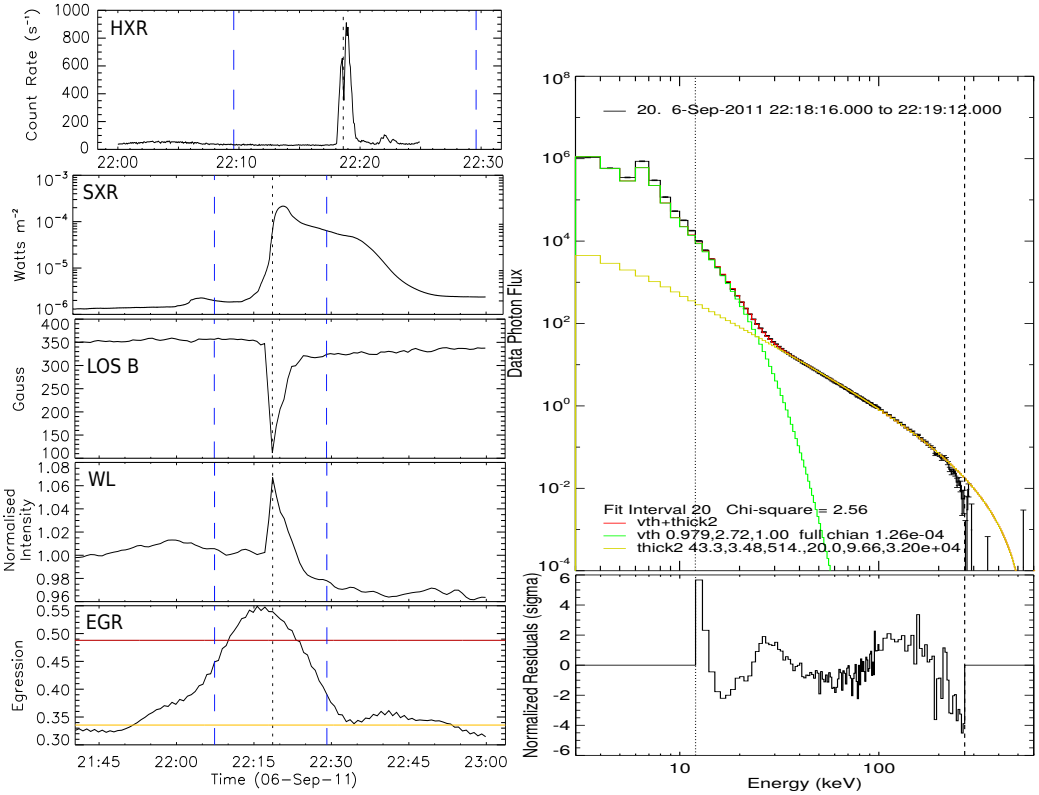


Figure 30. *Left plots*: light curves of RHESSI 100300 keV HXR (*HXR*), GOES (1.08.0 Å) SXR (*SXR*), integrated HMI LOS magnetogram (*LOS B*), WL continuum (*WL*) and egression power (*EGR*). The HMI data products are integrated over the seismic signal. Black vertical dotted line denotes the sunquake onset time (22:18:37 UT) from time–distance diagrams (Fig. 31). Continuum emission shows a peak emission at 22:18:37 UT, coincident with quake onset and LOS magnetogram transient. Egression power, normalised with respect to quiet sun levels, peaks above a defined detection threshold (red horizontal line) of the local mean (yellow) plus 5 within the flare window (blue vertical lines). *Right plots*: photon flux spectrum for the time interval 22:18:16–22:19:12 UT with variable thermal (green) and thick-target bremstrahlung (green) fitting giving the total fit (red) over the 12270 keV energy range (bounded in black) (*top*) and respective residuals of fitting (*bottom*).

DISTRIBUTION A: Distribution approved for public release. Distribution unlimited

4.7.2.c. Detecting a missing sunquake

In this work, for detection of the missing sunquake both time–distance and helioseismic holography combined statistical significance 25 analysis of egression power are applied. Additionally, the egression power from acoustic holography has been treated directionally, in order to analyse anisotropy of the source.

Detection results – holography

Helioseismic egression is computed from a single frame running difference of the SDO/HMI Dopplergrams (Schou et al. 2012), with a pupil size of 1080 Mm. We run a semi-automated statistical testing, as described in the section above, on a flare window of 22:09:37–22:29:07 UT in all the frequency bands. Significant signals are detected in 1 mHz frequency ranges around 4, 5, 6 and 7 mHz. The detected statistical egression kernel is bounded by red solid contours in the 6 mHz egression snapshot in Fig. 20a, located around 284″ -129″ – 6 mHz is typically where the strongest acoustic sources are observed. Another 6 mHz source (Fig. 29a) and a 7 mHz source are highlighted in Fig. 3118c and 18d, away from the detected sunquake source. These detections do not pass the necessary conditional tests to be verified as seismic sources, therefore, they are ignored. We note that the statistical kernels have different properties when compared to the egression kernels usually used in acoustic holography. For instance, apart from the capability to detect diluted signals, another clear difference would be smudging of a (usual) compact egression kernel due to the integration used in the statistical procedure.

In order to provide a spatial reference, Fig. 31 displays the source location contours, as determined by the detection code, for frequency bands 4–7 mHz over intensity continuum at 22:18:37 UT. It is clearly seen that the source is located in the penumbra to the north of the AR. In comparisons with LOS magnetogram reference at 22:18:37 UT, we see the source to be located in the parasitic positive polarity region of the AR (Fig. 31), in close vicinity to the umbral transient perturbation seen at the time of the flare – where we see WL emission peak and LOS magnetogram step change. Following methodology described by Zharkov et al. (2013a,b), we estimate the acoustic energy emitted from the source region into the 10–80 Mm pupil through 3–10 mHz frequency bands to be 8.26 ⇥ 10^{27} erg.

Directional egressions (calculated from the selected arcs of the input pupil (see the previous section), highlight the anisotropy of the seismic source, with the enhanced acoustic brightening observed within the source location in the input arc of 090 in Fig. 20a. Here, 0 is defined as the west on the solar disc, progressing anti-clockwise. This source is highlighted using the overplot 6 mHz statistical test result from Fig. 31 left, where it is centred at 284″ -129″ (black cross). By plotting the value of directional egression power, in terms of local non-flaring levels, at 284″ -129″ against arc starting angle (Macrae t al, 2018), the anisotropy of the source becomes clear, with peaking egression power between the starting angles 330 and 0 – essentially covering first bounce wave propagation between angles 330 and 90.

DISTRIBUTION A: Distribution approved for public release. Distribution unlimited

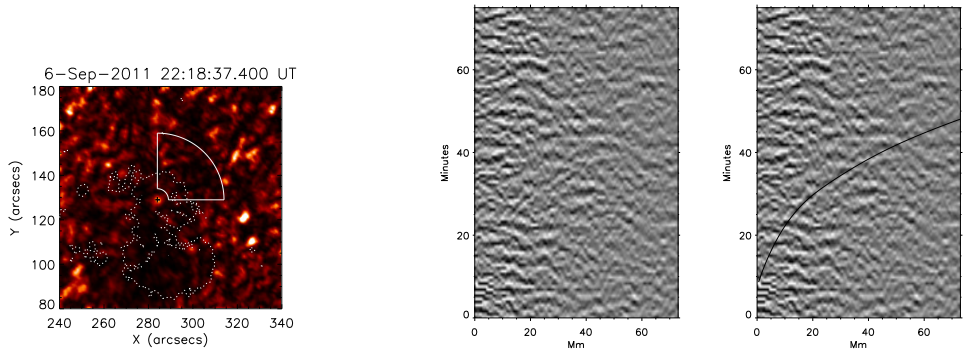


Figure 31. Sunquake of flare 6 September 2011. Left: Directional egression computed with a displayed pupil arc highlights the acoustic kernel centred at 284" -129". Value of the egression directional power is calculated at the same location and normalised to the local non-flaring levels is given in where angle denotes the starting angle of a 60 arc progressing anti-clockwise. Right: TD diagram is presented for the source centred at the same location using arc of 0 90 . A distance is in Mm and time is given in minutes starting at 22:11:07 UT. Fitting of the theoretical curve (*right* – black curve) yields an onset time of +7.5 min, or 22:18:37 UT.

Time-distance diagram

The sunquake was also detected in time-distance (TD) diagram collecting the ripples on the surface forming a ridge on the TD diagram. The results are presented in Fig. 31 (middle and right plots)), where we see an accelerating TD ridge become visible 20 min into the selected time range (starting with 0 min at 22:11:07 UT). This ridge is highlighted Fig. 20d (right) with an overplot theoretical ray path. Manual fitting of the ray path to the signal ridge indicates the onset time for the quake of +7.5 min, giving the sunquake start time at 22:18:37 UT. This is in agreement with the times of observable LOS magnetogram transient peak, as well as WL emission peak and about 20 s later than HXR emission onset (see light curves, Fig. 30).

4.7.3. Observations of the X9.3 flare of 6 September 2017

4.7.3.a. Magnetic configuration prior flare onset

NOAA active region (AR) 12673 was a flare-prolific region that had one of the fastest magnetic flux emergence rates ever observed (Inoue et al. 2018). The AR became very active from September 4, 2017, and produced many C- and M-class flares over a time interval of two days, eventually resulting in the pro- duction of an X2.2 flare at 08:57 UT and an X9.3 flare at 11:56 UT (SOL2017-09-06T11:53) on September 6 at disc location S09W34.

The non-linear force-free field (NLFFF) restoration of the magnetic field in this active region prior to the X2.2 flare followed by 3-dimensional (3D) magneto-hydrodynamic (MHD) simulations of magnetic field dynamics during the recent two solar flaring events of X-class occurred on 6 September 2017 (Inoue et al. 2018) revealed that after the X2.2 flare and prior to the X9.3 flare three magnetic flux ropes (MFRs) formed with very braided and twisted magnetic structures. It was shown that a tether cutting reconnection between the red and green loops illustrated in the plot of Fig. 32 produced long twisted red magnetic lines and drove the eruption during the X9.3 flare. Furthermore, the MHD simulation shown that one footpoint of this red loop became anchored in the positive polarity and the another footpoint was embedded in the negative polarity located in the northern area away from the main part of the active region. These long twisted red lines eventually reconnected with the green and blue lines creating a large green flux rope, which erupted during the X9.3 flare.

DISTRIBUTION A: Distribution approved for public release. Distribution unlimited

The places where the ropes are embedded into the photosphere are close to the locations of the sunquakes reported below.

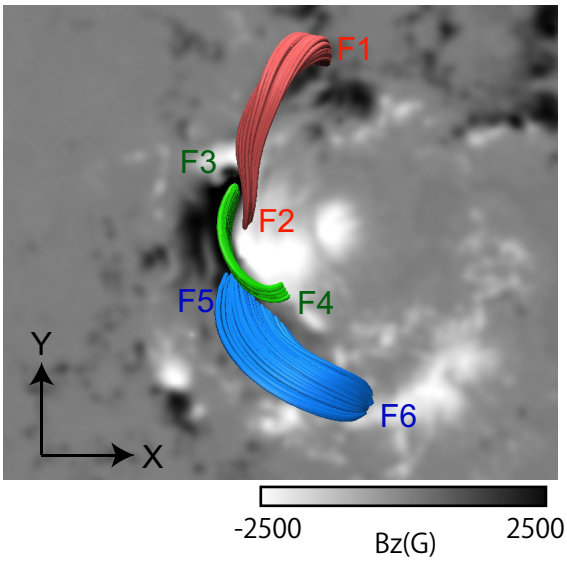


Figure 32. Magnetic flux ropes formed during the X2.2 flare just prior to the 9.3 flare derived from NLFFF magnetic field reconstruction by Inoue et al. (2018), which established the magnetic topology derived by the MHD simulations just prior to the X9.3 flare (b) with the loop footpoints being linked to the sunquake locations.

4.7.3.b. γ-*ray, hard X-ray bremsstrahlung and Ly-alpha emission*

Flaring event 1 (FE1) of the X9.3 flare of the 6 September, 2017, occurred at 11:55:29.0 UT. The Ly-α light curve (Fig. 33 right plot) clearly demonstrates a succession of four distinct flaring events (Fes) occurring at approximately 11:55:30 UT, 12:04 UT, 12:06:40 UT, and 12:08 UT. These events were seen separately by KONUS /WIND payload (FE1) and then by RHESSI (FE4) payload.

The flaring event 1, together with a few spikes, was observed by KONUS/WIND (see Fig.33, left) and lasted for a few minutes before the second series of flaring events occurred from 12:04:30 UT to 12:07 UT , which were recorded in Lyα line emission by the LYRA payload. The third flaring event starting from 12:08 UT was later recorded also by RHESSI. The KONUS instrument aboard WIND satellite observations in G1, G2, and G3 channels with high temporal resolution is shown in the top plot of Fig. 33, left plot from 11:55:29.0 UT until 11:59:18.7 UT (Lysenko et al. 2019).

Proton spectral index in ≤30 MeV energy range is s = 4.0 ± 1 and the total energy of ions was estimated to be about 1.1×10^{31} erg (Lysenko et al. 2019). For the area of footpoints affected by this beam we considered Hα line observations, which allowed us to estimate the initial energy flux of particle beams.

DISTRIBUTION A: Distribution approved for public release. Distribution unlimited

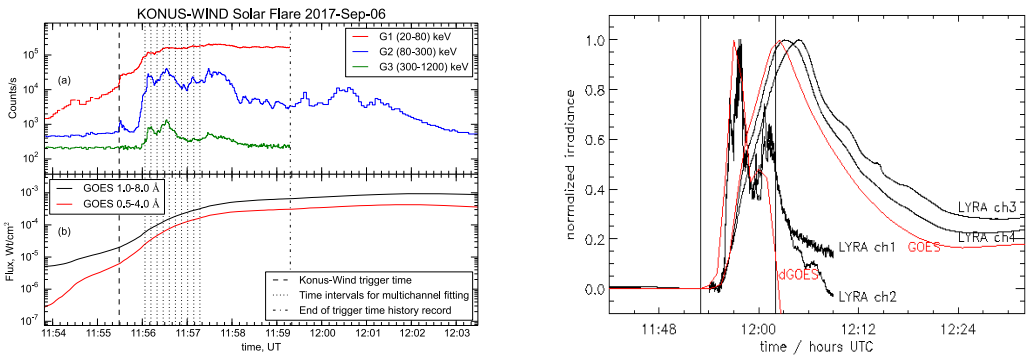


Figure 33. The light curves of the X9.3 flare. a): Light curves by the KONUS instruments (upper plot) and by GOES (bottom plot). b): the light curve in Ly-α line observed by the LYRA instrument (Hochedez et al. 2006; Dominique et al. 2013) showing flaring events 1 (after 11:55 UT) and 2 (after 12:04 UT, see the text for details).

4.7.3.c. Detection of seismic sources - holography

The seismic sources detected in this active region during the time of the flare by using the simple 5σ rule of the acoustic holography method are shown on the HMI white light in Fig.34 (left plot). The egression contours in 3-7 mHz frequencies for those four seismic sources clearly confirmed by the further statistical analysis are shown on the HMI magnetogram image in Fig. 34 (right plot). The point locations of the four seismic sources are indicated by the asterisks in the HMI white light image in Fig. 34 (left plot), where the future time–distance diagrams are obtained, while the sectors in the three seismic sources with the most significant statistical signals derived using the directional holography are shown in Fig. 34 (right plot).

The locations of these four acoustic sources coincide with some of the footpoints of the magnetic ropes formed just prior to the X9.3 flare onset as demonstrated by the simulations of (Inoue et al. 2018) and shown in Fig. 32. Namely, the acoustic source 1 (seen in holography and TD diagram) occurring during flaring event 1 is likely linked to the F3 footpoint in the northern end of the green rope (see Fig. 32). The strongest seismic source, source 2, which is clearly seen in holography and TD diagram, is linked to the F5 footpoint at the southern end of the green rope. Seismic source 3 (seen in holography and TD diagram) is linked to the F5 footpoint of the northern end of the blue rope and source 4 (seen only on holography) is linked to the F6 footpoint of the southern end of the blue rope.

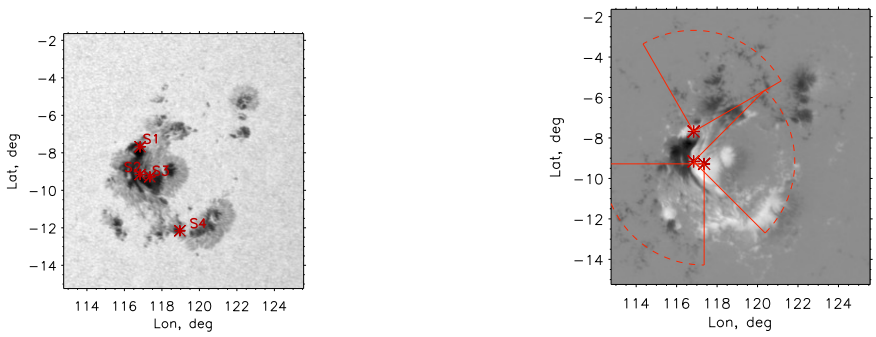


Figure 34. (left) HMI white light image of the active region marked with the egression maps of the seismic sources 1-4; (right) Directivity maps of seismic sources 1-3 derived with directional holography shown by the sectors with detectable acoustic signals marked by the solid and dashed red lines.

DISTRIBUTION A: Distribution approved for public release. Distribution unlimited

The locations of these four acoustic sources coincide with some of the footpoints of the magnetic ropes formed just prior to the X9.3 flare onset as demonstrated by the simulations of (Inoue et al. 2018) and shown in Fig. 32. The acoustic source 1 occurring during flaring event 1 is likely linked to the F3 foot- point and has a directivity consistent with an angle of the shock deposition of -(0 − 10)°. The middle (and strongest) acoustic source 2 clearly seen also during flaring event 1 is linked to the F4 footpoint and its directivity indicates an angle of -30° for the shock deposition. Acoustic source 3, linked to footpoint F5 of the blue rope, has a directivity that is in agreement with an angle of +30° to the local vertical. The most southern acoustic source 4 on the other hand is linked to footpoint F6 of the blue rope with an angle of the shock deposition of +30°.

4.7.3.d. Time-distance diagrams

The time–distance diagrams are detected in three seismic sources, or sunquakes (SQs): 1, 2 and 3 (see Fig. 36). These TD diagrams are significant improvements on the seismic results reported earlier (Sharykin & Kosovichev 2018; Zhao & Chen 2018), since the TD diagrams for sources 1 and 3 are reported for the first time. Also, for the source 2 we were able to detect for the first time a second bounce of the acoustic waves produced in the flaring at- mosphere of footpoint F4 discussed in the last few paragraphs of this section, which was predicted earlier (Duvall et al. 1997) but never observed in flares. Nevertheless, it was not possible to detect ripples with a TD diagram for seismic source 4. We suspect this is because the seismic source 4 was rather weak, only being seen by the holography method at the frequency of 6 mHz, which indicates that the heights of its ripples were at the level of the background noise, making them undetectable with a TD diagram.

The TD diagrams detected for SQ1-SQ3 are presented for seismic source 1 in Fig. 36 (two right plots), and seismic source 2 in Fig. 36 (two left plots0. The SQ 1, is located in foot-point F3 of the green loop, and SQ 3 is located in footpoint F5. Their TD diagrams are computed from the surface signal centred on a field of view (FOV) of 284″×129″, as determined through directional egression analysis, over the 90 ° arc originating at 60°.

The TD diagram of SQ 1 shows a rather weak TD ridge, which becomes visible 15 minutes into the selected time range (starting at 11:55:37 UT). This ridge is highlighted in Fig. 6 (*right*) with an overplotted theoretical ray path. Manual fitting of the ray path to the sig- nal ridge indicates an onset time for the quake of +7.5 minutes, resulting in the start time at 11:55:37 UT for the SQ 1 (source 1 in flaring event 1). This is in agreement with the time of the observable LOS magnetogram transient peak, as well as the WL emission peak. The TD diagram shows that the ridge approached the end of the datacube of 120Mm with a velocity of 48 km/s. The TD diagram of seismic source 3 showed the ripples started at the same time as in the seismic source 1. Although, seismic source 3 has a deeper ridge, which approaches the 120 Mm distance slightly quicker than in source 1, travelling with a velocity of 51 km/s.

The TD diagram for acoustic source 2, which is located in the F4 footpoint of the green loop, is computed from the surface signal centred on 284″ ×129″ , as determined through directional egression analysis (see Fig. 34, right plot), over a 90 ° arc starting at 60°. The results for seismic source 2 are presented in Fig.36 (most *left plot*), where one can see the very deep TD ridge approaching a velocity of about 52 km/s at the edge of the data cube of 120 Mm, which become visible 8-10 minutes into the selected time range (starting with 0 minutes at 11:55:37 UT). This ridge is highlighted in Fig.36 (*second left plot*) with an overplotted theoretical ray path. Manual fitting of the ray path to the signal ridge Fig.36

DISTRIBUTION A: Distribution approved for public release. Distribution unlimited

(*second left plot*) indicates, similar to source 1, the onset time for the quake of +7.5 minutes, giving the sunquake start time at 11:55:37 UT (source 2 in flaring event 1). This is in agreement with the time of the observable LOS magnetogram transient peak, as well as the WL emission peak and about 20s later than HXR emission onset (see the light curves, Fig. 30).

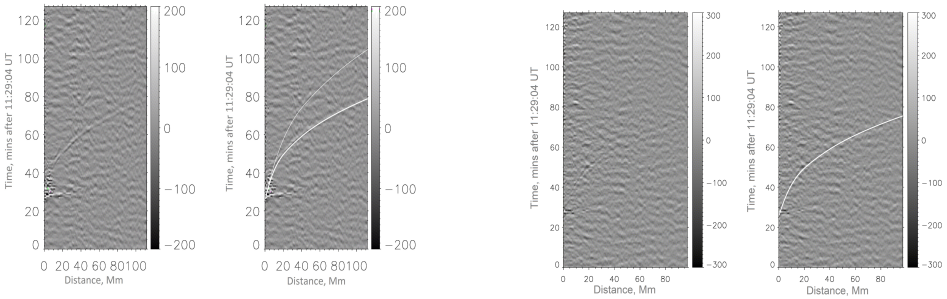


Figure 35. Time–distance diagram for the seismic sources SQ2 (left) and SQ1 (right), obtained from the filtered HMI dopplergram without (left) and with (right) theoretical curves. The TD diagram shows the ridge derived from ripples produced at some distance from the event location by acoustic waves in their first bounce from the photosphere (lower white line) and the second bounce (upper white line). The start (zero) time on the Y-axis is 11:29.04 UT, which corresponds to the shock deposition and seismic response initiation at 11:55:37 UT. The grey colour bars on the right show the background Doppler velocities in m/s.

There is also the indication of a unique feature seen for the first time on the time–distance diagram obtained for seismic source 2: a second ridge above the first one marked by the second white line of the ridges shown in Fig.36 (second left plot). This second ridge indicates a second bounce from the surface of the acoustic waves (Duvall et al. 1997) propagating in the solar interior after their first bounce and reflection back to the surface by the interior because of Fermat principle. The second bounce acoustic waves are assumed to exist but until now have never been observed in this or any other flares. The second ridge shown in Fig.35 has, as expected, a slower speed of the ripple propagation on the solar surface approaching about 27 km/s at the distance of 120 Mm.

DISTRIBUTION A: Distribution approved for public release. Distribution unlimited

4.7.3.e. Extreme ultra-violet signatures

The X9.3 flare was also observed with the EUV Imaging Spectrometer (EIS) aboard the Hinode spacecraft (Culhane et al. 2007). In Fig.36 we plot a series of He II 256.3 Å spectrograms at the slit positions that include the sunquake locations as well as a few slits to the east and west of those lo- cations for comparison. The slit positions that correspond to strongest 6 mHz seismic sources are located at heliocentric lo- cations at 528-540 arcseconds. The spectrograms illustrate the intensity of the emission as a function of heliocentric location on the y-axis and Doppler velocity (wavelength) on the x-axis. The wavelength axis was converted to velocity units using a rest wavelength derived from a pre-flare raster at 11:48 UT and the instrument spectral dispersion. Negative velocities indicate blue-shifted or upflowing plasma, while positive velocities indicate redshifted or downflowing plasma. The black horizontal lines indicate the heliocentric location of the egression sources on the disc (N-S).

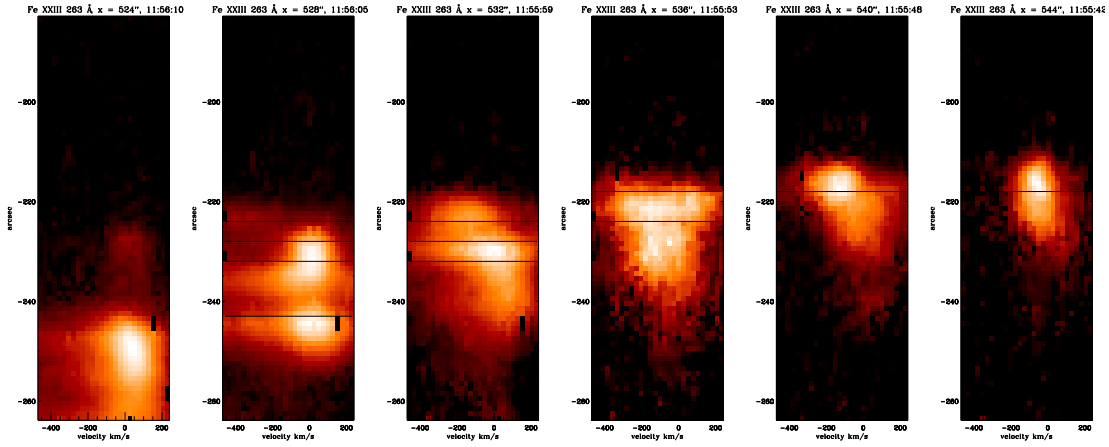


Figure 36. Flaring event 1 (>11:55 UT): Series of EIS spectrograms in the Fe XXIII 263.76 Å line taken during the onset phase of the X9.3 flare on 6 September 2017. The titles above spectrograms indicate the time and slit location, while the y-axis represents location along the slit, and Doppler velocities represented on the x-axis. Black horizontal lines indicate the location of the egression sources.

it can be observed that there are asymmetries associated with the egression source locations (black lines) both to positive and negative velocities of several hundred kilometres per second. The most intense He II emission ap- pears shifted towards positive velocities (redshift; the bottom three rows for flaring atmospheres with SQs 1-3, indicating the downflows of >250-300 km/s caused by hydrodynamic shocks generated in these atmospheres). These shifts appear at the start of flaring event 1 (and sunquakes (SQs) 1-3) and last for 90 seconds before the appearance of blue-shifted profiles during the flare relaxation phase (shown in the upper four rows when downward moving material returns back to the solar atmosphere from the interior, thus showing upflows, or lines with blueshifts).

We also shown in the paper Zharkov et al, 2020 these downflows and upflows in more detail by plotting the He II line profiles for six slit positions in time shown on the top of each window. The SQ locations associated with these motions are indicated at the slit positions with a black line. These include the locations of the egression sources, as well as the positions within the flare ribbons outside of the egression sources. The X positions are plotted on the left- hand side of each spectrum: 528″ (the left column), 536″ (the central column) and 540″ (the right column). The observation time starts from the time close to the

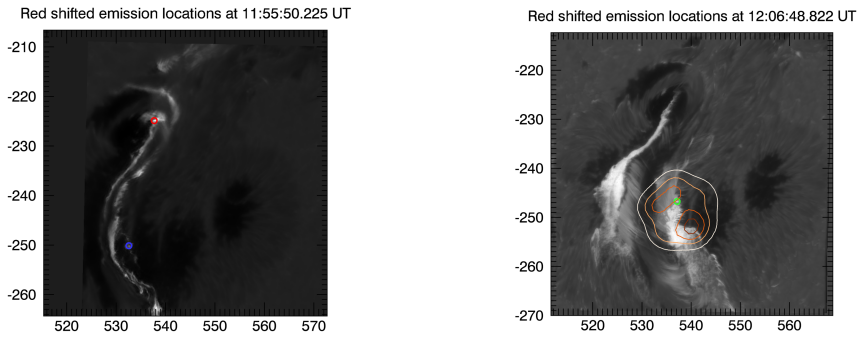
DISTRIBUTION A: Distribution approved for public release. Distribution unlimited

SQ onsets (the right-most plot) and continues to later times from right to left. These locations correspond to the locations of SQs 1, 2, and 3. As can be seen from the He II profiles, the emission is predominantly redshifted in the SQ locations. Given the complex nature of some of the line profiles, we do not fit the lines (e.g. slit position 536$''$), but use the rest wavelength and spectral dispersion to indicate the range of velocities present.

The Fe XXIII line profiles demonstrate from the very start the increasing blue asymmetry of the Fe XXIII line at several locations along the slits that sample SQs 1, 2, and 3. The blueshifts are highest at the onset of flaring event 1 in source 2 and are slightly lower in SQ 1 and 3. Figure 13 displays the spectrograms of the Fe XXIII 263.76 Å line for flaring event 1, where one can see predominantly blueshifted velocities of several hundred kilometres per second with upflows in excess of 300-400 kms^{-1} observed around (528-532$''$, -232-243$''$). In this case, the velocity scale was derived relative to the laboratory rest wavelength as Fe XXIII is only produced in plasmas of T>10MK during flare conditions, so that no 'quiet' sun reference is available. In both He II and Fe XXIII spectrograms, it is clear that large asymmetries and flows are observed at flare onset, as expected.

4.7.3.f. H-alpha observations

We used the H-α observations by the CRISP Imaging Spectro- Polarimeter (CRISP) (Scharmer et al. 2003; Scharmer 2006) at Swedish Solar Telescope (SST). We identify two locations for the study of the Hα line profiles using frame 0 shown in Fig. 37. The identified kernels are: Kernel 1, which is closely co- spatial with the seismic source 1, possibly indicating the northern footpoint F3 of the green magnetic rope (see Fig.32), which later erupted during flaring event 1; the second kernel (kernel 2) was located close to the northern footpoint F5 of the blue mag- netic rope, which produced seismic source 3 (see Fig. 1, left); Hα kernel 3 was observed at 12:06:48 UT during flaring event 2 at the location of the southern footpoint F2 of the red rope. This footpoint was close to the location of footpoint F4 of the green rope (Fig. 32), which erupted before flaring event 2 freeing the space for the footpoint F2 of red rope. Its location is close to seismic source 2 but the event likely occurred 10 minutes later as a new seismic source 5.



DISTRIBUTION A: Distribution approved for public release. Distribution unlimited

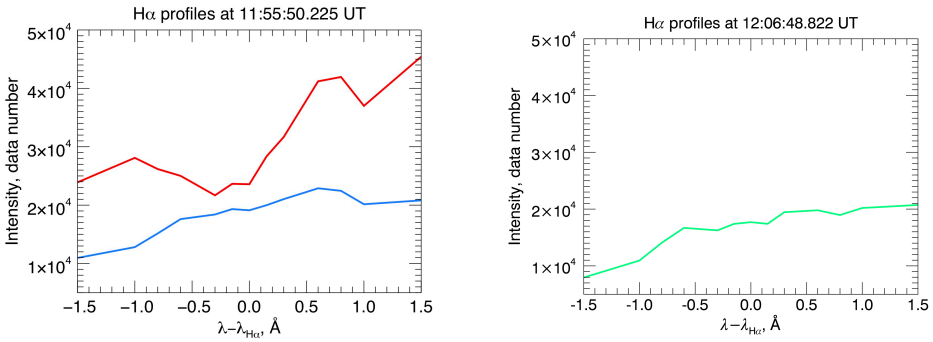


Figure 37. H-alpha line observations of flare 6 September 2017. Top plots: Red wing emission (λ*Hα*+ 1.5 Å) in the Hα line at 11:55:50 UT (flaring event 1) with the locations of (a) kernel 1 (seismic source 1) and kernel 2 (seismic source 2), shown by the red and blue circles, respectively, and the location of (b) kernel 3 (flaring event 2), marked by the green circle, observed at 12:06:48 UT . Bottom plots: (c) Hα line profiles in kernel 1 (red line) and kernel 2 (blue line) and (d) kernel 3 (green line) obtained with SST (arbitrary units) by taking the average over the pixels. The HXR contours obtained at 12:08:26 UT are over-plotted for the 25-50 keV channel with the contours at 0.25 of maximal intensity (white), 0.48 (light brown), 0.7 (medium brown), and 0.9 (dark brown).

The top panel of Fig.14 shows the images taken at 11:55.50 UT (left) and 12:06:48 UT (right) in Hα (6563 + 1.5) red wing emission. Kernel 1 (red circle) occupied five pixels in the observation at 11:55:50 UT, representing an area of around 9245 km^2 (equivalent area to a 96 by 96 km box). This frame is of particularly good image quality and shows enhanced red wing emission in the northern end of the eastern ribbon, as highlighted by the red circles in Fig.37 in Hα kernel 1. The line profile in each kernel was produced by taking the average of the profiles from these five pixels, which were individually alike.

The average profile for kernel 2 (blue circle) (Fig. 37) was produced in a similar way, by taking the average of the similar profiles over 14 pixels, covering an area of around 25,900 km^2, equivalent to the area covered by a 161 by 161 km box. The emission in kernel 2 shows an enhancement in the red wing at 11:55.50 UT; it is shown in the location marked by a blue circle, where the seismic source 2 was located.

The Hα emission in kernel 3, whose location is indicated by the green circle in Fig.37, shows enhancement in the red wing of the Hα line profile occurring 1 minute before the RHESSI HXR signatures detected after about 12:08:26 UT (see Fig.37, top right plot). This emission occupies 22 pixels showing similar profiles over an area of 40,680 km^2.

4.7.3.g. Hα-line profiles

The Hα profile of the spectral data from the Hα kernel 1 is shown in Fig.38 (bottom panel, red line). This feature does not have strong emission in the Hα line core. However, it does have highly enhanced red wing emission, with the emission intensities still increasing as one moves up to 1.5 Å from the line centre (see Fig.37). The Hα line profile in kernel 2 (the blue line in the bottom panel of Fig.37 is also likely to show the emission profile with strong red asymmetry catching only the intensity of a blue wing, with the central part of the profile being strongly redshifted beyond the available CRISP spectral window of 3 Å. Therefore, it is certainly possible that the core profile intensities in both Hα kernels 1 and 2 will be shifted well above 3-4 Å in the red wing for both these kernels, thereby falling outside the observed

DISTRIBUTION A: Distribution approved for public release. Distribution unlimited

wavelength range of the spectral window. This assumption can be only tested by the simulations presented in paper 2 (Zharkova et al. 2020).

The profile in Hα kernel 3 (Figure 37, bottom right plot, green line) for flaring event 2 at 12:06:48 UT shows a much larger intensity rise in the near blue wing than in flaring event 1 (kernel 1), indicating a redshift larger than the size of the spectral window (>3 Å). This is similar to the behaviour seen in Hα kernel 2, which coincides with seismic source 2. Hence, it can be also argued that we only observe a blue wing of the Hα emission, and see little sign of the central core emission with self-absorption, as this part of the line is shifted to the red wing outside the spectral window of CRISP.

4.7.3.h. White light emission

In the continuum images observed by SDO/HMI, AR NOAA 12673 appears to be made up of a main delta spot (S1) sur- rounded by some smaller spots (S2-S5) in the northern and southern parts of the active flaring events (top panel of Fig. 38). The WL emission of the X9.3 flare is relatively intense and exhibits a clear ribbon shape, including the same regions previously involved in the first X2.2 flare (Romano et al. 2018). The area covered by the WL ribbons in the continuum filtergram at 11:59 UT reaches a maximum extension of about 9.2 $\times 10^7$ km^2.

We selected two cases of the enhancements in white light emission in the HMI continuum during the flaring events of the X9.3 flare shown in Fig. 15 during the flaring event at 11:55:56 UT located in Hα kernel 2 (left plot) and 12:06:00 UT located in Hα kernel 3 (right plot). The pixels from the first WL event were located in seismic source 2 and those from the second WL event were located in seismic source 4. It can be observed that WL emission in both events grows very sharply at their beginning. However, the emission in WL event 1 occurred during FE1 drops very sharply after its maximum, while WL emission in the second WL event occurred during FE2 has double peaks and shows much slower decay over time, indicating larger initial intensity of the hydrogen continuous emission in Paschen continuum as was proposed by Druett & Zharkova (2018).

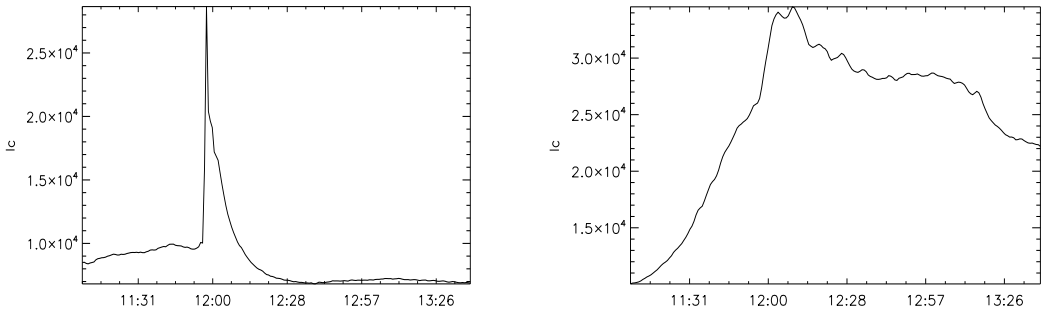


Figure 38. White light emission of flare 6 September 2017. Left: Temporal profiles of white light emission obtained in the WL kernel 1 in the locations of the Hα kernels 2 and seismic source 2. Right: WL light curve in kernel 2 at the location of Hα kernel 3 and possible seismic source 5.

DISTRIBUTION A: Distribution approved for public release. Distribution unlimited

4.7.4. Hydrodynamic models of flaring atmospheres

4.7.4.a. Parameters of particle beams

Given that the area covered by Hα emission in kernel 1, which occurred at the start of flaring event 1, we believe it is safe to suggest that it could be produced by beam electrons with an energy flux of about $(6 - 8) \cdot 10^{12}$ erg·cm^{-2}·s^{-1} . We can still use a spectral index of 4 derived from the KONUS observations. While the Hα line profile observed in kernel 2 has a lower intensity than in kernel 1, its area is smaller than that of kernel 1, indicating that the mixed beam should have a higher initial energy flux of $(8 - 12) \cdot 10^{12}$ erg·cm^{-2} ·s^{-1} and the similar spectral index of 4 as in the Hα kernel 1. Because of the small area of the Hα kernel 3 and the absence of HXR emission at the start of flaring event 2, the initial energy flux of the beam that produced this emission remains unknown. However, only the blue wings of the Hα line profile were observed without the line cores in kernels 1, 2, and 3, thus, indicating that the redshifts in these kernels were rather substantial.

4.7.4.b. Hydrodynamic models of flaring atmospheres heated by mixed and electron beams

Hydrodynamic responses of flaring atmosphere caused by 10 second pulses heating by intense particle beams (either mixed or pure electrons) are shown to lead to quick sweeping of the quiet sun (QS) chromosphere plasma towards the photo- sphere and beneath forming hydrodynamic shocks, which are shown to first move with large velocities towards the solar interior and to later return to the pre-flare conditions. The phases of this process include the initial heating by beam particles in Coulomb collisions lasting ten seconds after the beam on- set, which produces a hydrodynamic response of the ambient plasma to this heating followed by slow cooling off of the am- bient plasma and its return to the pre-flaring position and conditions. Hydrodynamic responses start to develop over a minute after the beam onset and last up to an hour because of a larger characteristic hydrodynamic time (order of 30 seconds) caused by thermal diffusion (Shmeleva & Syrovatskii 1973).

Hence, the hydrodynamic simulations for the flaring atmo- spheres heated by a mixed beam in the footpoints associated with the seismic sources 2 and 3 are plotted in Fig.39 (left column). For a comparison of the current conditions for sunquake 2 with the conditions of the sunquake formation in the flare of 6 September 2011, in Fig.39 (right column) we present the hydrodynamic models simulated for the injection of an electron beam with the initial energy flux of $4.3 \cdot 10^{11}\ erg \cdot cm^{-2}\ s^{-1}$ and spectral index of 4 (Macrae et al. 2018). These two hydrodynamic models can provide important insight into the mechanisms of formation of the acoustic signatures in two flares discussed below.

It can be noted that the hydrodynamic responses induced by a mixed beam (Fig.39, left column) in flare of 2017 and by electron beam (Fig.39, right column) in flare 2011 are very different despite they both show a quick increase of the kinetic temperatures within the first 5 seconds after the beam onset. However, compared to the initial chromospheric temperature of 6700K, the mixed beam causes a much stronger increase of the kinetic electron temperature in the corona up to 40 million Kelvin (MK) (Fig.40a), while the kinetic temperature in- crease by less intense beam is found increasing only to 10 MK. The ambient plasma density in the atmosphere heated by either beams (Fig. 39b is significantly reduced in the flaring corona, from the initial QS chromospheric magnitude (10^{10} cm^{-3}) to $10^{9} - 10^{8}$ cm^{-3}, to form the new corona of a flaring atmosphere (Somov et al. 1981). As expected, during the time of the beam injection (10s) there is also a larger reduction of the coronal

DISTRIBUTION A: Distribution approved for public release. Distribution unlimited

density swept by precipitating mixed beam compared to the electron one (see Fig. 39b). These trends are similar to the hydrodynamic models heated by electron beams with the same parameters reported by Fisher et al. (1985a,d).

This stronger plasma sweeping in the flaring atmosphere by the mixed beam leads to a larger speed of chromospheric plasma evaporation back to the corona that approaches 1600 km/s compared to 1300 km/s for an electron beam as shown in Fig. 39c (compare the left and right plots). Furthermore, the fast dynamics of the coronal plasma heating by a mixed beam leads to very strong, explosive, evaporation (with velocities above 1500 km/s) of the chromospheric plasma to the coronal levels up to 8000 km above the surface, while the electron beam would cause much milder evaporation to the heights of about 1500 km above the surface approaching the macrovelocities just above 1200 km/s.

The upward motion of the flaring plasma is reflected in the macrovelocity plots (Fig. 39c), showing negative (upward) macrovelocities corresponding to the evaporation of chromo- spheric plasma upwards to the newly formed corona at the column depths between 10^{17} and 10^{19} cm^{-2}. This evaporation lasts for a one-two thousand seconds even after the beam is stopped expanding with the increasing velocities up- wards to the QS corona (Somov et al. 1981; Fisher et al. 1985c,e; Zharkova & Zharkov 2007). The evaporation velocities range from a few tens of $km{\cdot}s^{-1}$ (at 1s) up to 1500 $km{\cdot}s^{-1}$ (at 30–100 s). As shown earlier (see section IV and Fig. 5 in Fisher et al. 1985c), these high upflow velocities naturally appear in the gasbag models (Somov et al. 1981; Fisher et al. 1985c; Zharkova & Zharkov 2007).

Besides large upflows, the abrupt energy deposition by super-energetic particle beams within a short timescale of 10 seconds leads to a formation in the flaring chromosphere of low temperature condensations, which move downwards to the photosphere and interior with supersonic velocities as shocks, thus producing large downflows (Somov et al. 1981; Zharkova & Zharkov 2007; Zharkova & Zharkov 2015). From comparing the macrovelocities and depths of penetration for different times after the beam injection, it becomes evident that the higher the initial energy flux the larger the speed of a shock produced by hydrodynamic response (Zharkova et al, 2020). For example, for the mixed beam the shock velocities of 50 − 100 $km{\cdot}s^{-1}$ are reached just 1 second after the beam onset (see Figs. 39c) while after 5 seconds these velocities sharply increase to 200 − 250 $km{\cdot}s^{-1}$ for weaker beam (see Figs. 39c, right plot) and 380-400 km/s for more intense beam (see Figs. 39c, left plot). The plasma of the shocks has a slightly (up to 10^4 K) increased temperatures and much larger densities (a factor of 10^{13} cm^{-3} up to 10^{14} cm^{-3}) for the most powerful mixed beam (Fig. 39b, left plot).

Hence, these shocks have large densities and high macro- velocities being capable of delivering very large momenta to the lower atmosphere and. solar interior. It is important to determine how deeply these shocks can travel into the QS solar atmosphere.

DISTRIBUTION A: Distribution approved for public release. Distribution unlimited

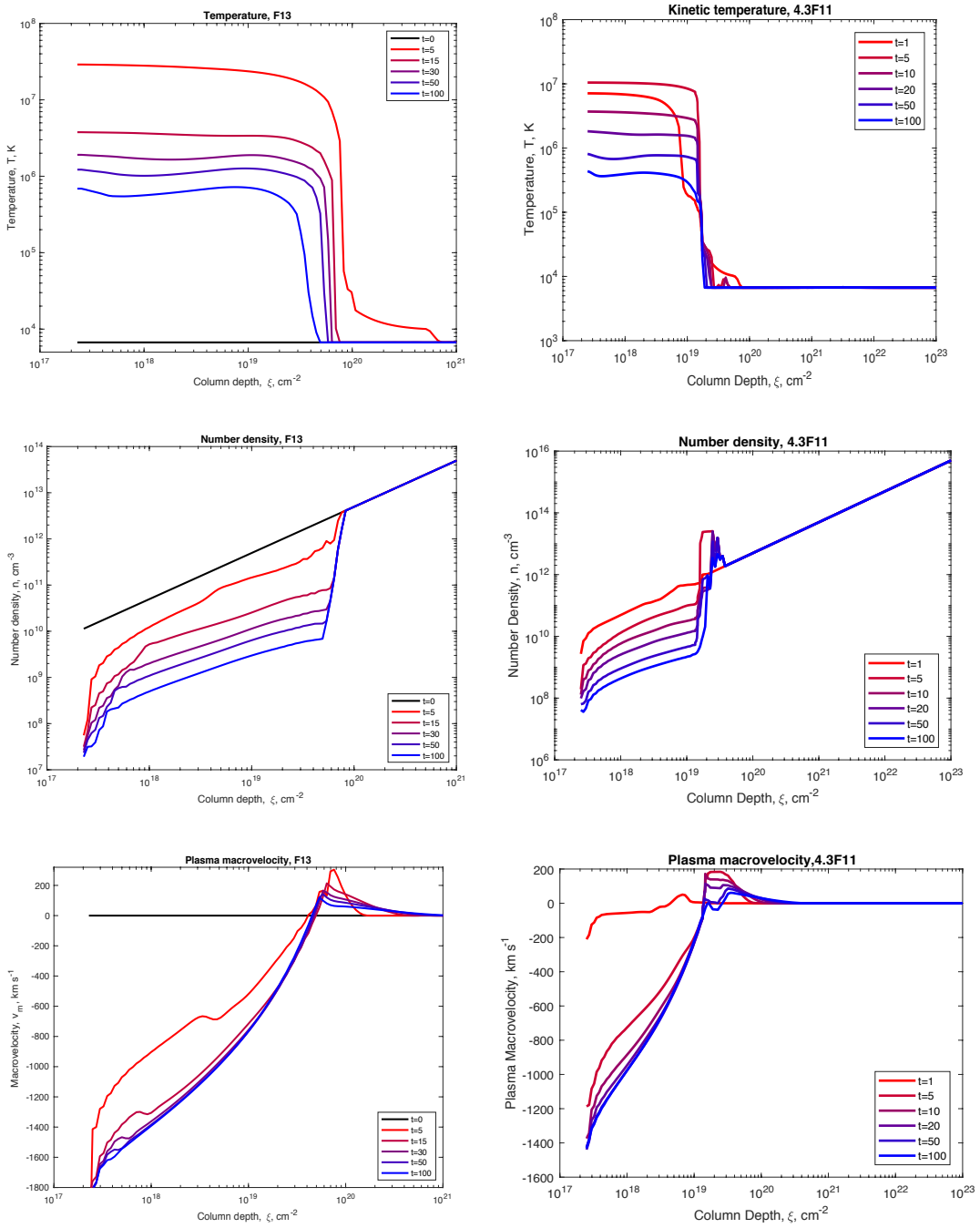


Figure 39. Hydrodynamic models of flaring atmospheres. The simulated hydrodynamic responses of flaring atmospheres to the injection of power-law particle beams with the initial energy flux of 1.0×10^{13} erg·cm^{-2}·s^{-1} and spectral index 4 (left column) and with the initial energy flux of 4.3×10^{11} erg·cm^{-2}·s^{-1} and spectral index 3.5 (right column) showing the column depth dependencies of electron kinetic temperature, K (top row), ambient plasma densities, cm^{-3} (middle row) and plasma macrovelocities, km·s^{-1} (bottom row).

4.7.5. Shock propagation in the solar interior

The shocks generated by a mixed beam shown in Fig. 39c, left plot are presented versus a linear depth of the quiet Sun (a) and time (b) (see Fig. 40, left column) for the flare of 2017

DISTRIBUTION A: Distribution approved for public release. Distribution unlimited

while the shocks deposited by an electron beam for the flare of 2011 are shown in Fig. 40, right column.

It can be noted that the shocks generated by the electron beam were first deposited above the solar surface and only later propagated with a supersonic velocity into the solar interior to the depths above 500 km. Since the shocks travelled not a very long distance in the interior, it did not produce very intense acoustic waves, so that the the ridge they produced in TD diagram is not very deep that explains why it was missed at first.

While the shock produced by the mixed beam shown in Fig. 40, left column) is deposited from the very first seconds in the solar interior with a supersonic speed. The hydrodynamic shock formed in a flaring atmosphere enters the solar interior (crosses the linear depth of zero) above the local sound speed, with the vertical velocities of $v(z_S)$ = 380 km·s^{-1} at z_S = 100 km s^{-1} (Fig. 40a). The density of the shock should be (1 – 3) × 10^{13} cm^{-3}. The macrovelocities of a downward mov- ing hydrodynamic shock reach 280 kms^{-1} at 5 s then slowly reducing to 175 at 50 s, approaching 100 km/s at 100 s, so the average macrovelocity is about 180-200 kms^{-1} (see Fig. 40, left column). These downward velocities were complied well with those derived from the Hα kernels 1 and 2 detected in the locations of seismic sources 1 and 2 for the flaring event 1.

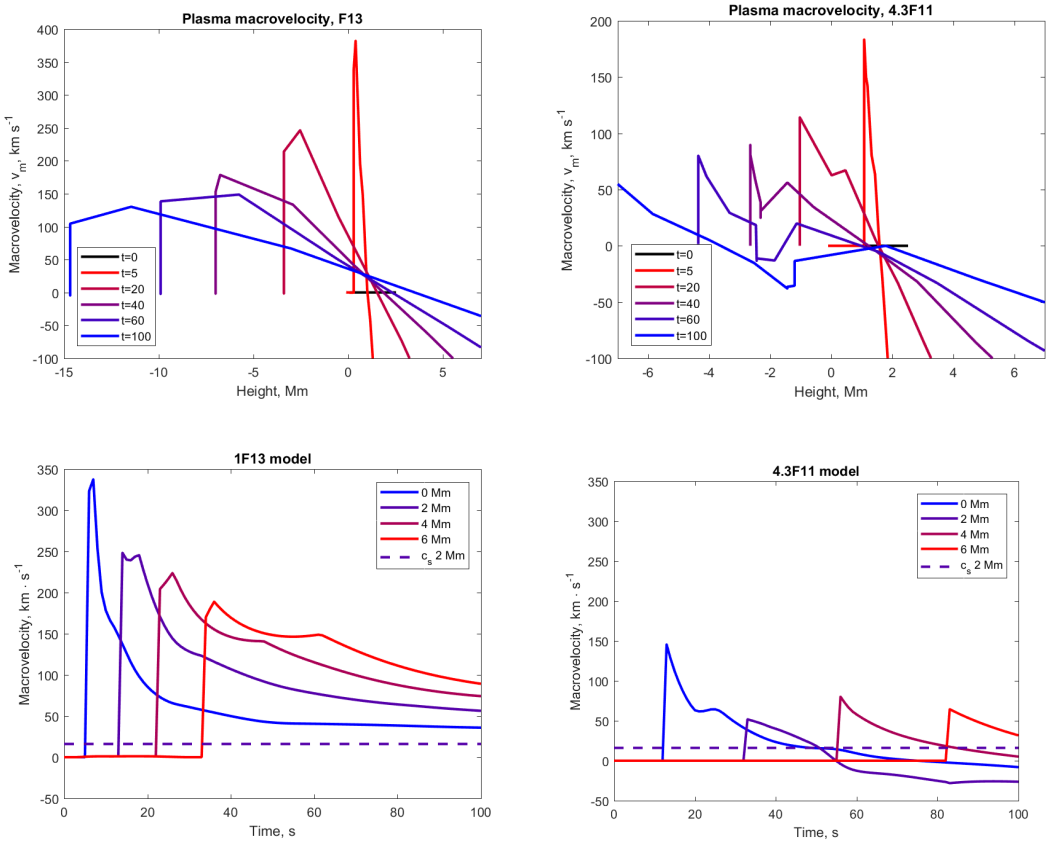


Figure 40. Velocity versus linear depth profiles of the simulated hydrodynamic shocks in the seismic event 2 of flare 6 September 2017 (left column) and sunquake of 6 September 2011 (right column) plotted versus linear depths under the quiet Sun (QS) photosphere for different times after beam injection (top row) and versus time after the beam onset for different linear depths in the solar interior under the QS photosphere (bottom row). Zero in the X-axis indicate the position of the QS

DISTRIBUTION A: Distribution approved for public release. Distribution unlimited

photosphere, the negative numbers indicate the depth under the photosphere (see text for details). The solid black line in (a) represents sound speed in the photosphere.

The depth of deposition of this shock in these events starts from the surface, or quiet sun photosphere, and moves down to 1000 km depth in the interior (Zharkova et al, 2020). The plasma density in the shock is about $(5-6)\times 10^{13}\ cm^{-3}$. Thus, such the shock is capable of producing intense acoustic waves for a rather long time while travelling inside this interior (compare the curves for different times in Fig. 41a.) Hence, the shock produced by the mixed beam produced a very deep ridge for the first bounce. And because the first set of acoustic waves was very intense, they had enough energy to travel to the interior, be reflected from it back to the surface following the Fermat principle and to travel to the solar surface again to become bounced back by the photosphere at the second upper turning point, as the theory predicts. Only very intense mixed beam can produce such the phenomenon observed for the first time for the flare 6 September 2017 (Zharkov et al. 2020).

By comparing the line profile observed in Hα kernel 3 we reckon that it can be produced in flaring atmosphere heated by a mixed beam with the initial energy flux close to $(6-8)\times 10^{12}\ erg/cm^2/s$, spectral index is 4. From the simulated hydrodynamic model we derive that the density of the shock should be $(1-3)\times 10^{13}\ cm^{-3}$, and the shock macrovelocity would be slightly lower than in source 2 reaching 320 kms^{-1} at 5-10 sec and dropping to 100 at 50-60 s, with the average velocity of 120-140 kms^{-1}. The shock starts above the surface and propagates as a shock down to 500-1000 km below the surface, and the angle of deposition is about $+30^{\circ}$ from the vertical as derived from directional holography approach. The impact of these shocks on the seismic response of the solar interior beneath the flaring atmospheres where they produced is discussed in section below.

4.7.6. Interpretation of the EUV, H-alpha and WL emission in these two flares

4.7.6.a.EUV

The HD models heated by the mixed beam produce within 5-15 seconds very fast heating of a flaring atmosphere above 40 MK that may explain an early brightening of flaring atmosphere in 1700 Å leading to its over-exposure of this AIA emission. For the HD model caused by the powerful mixed beam the EUV emission can be observed by EIS instrument in He II and Fe XXIII emission at the very beginning of the flare onset if the flaring atmosphere temperature approaches the temperature range suitable to the radiation temperatures of these transitions: 7-20 million K for Fe XXIII and about 10^5 K for He II line. It can be seen that the temperature magnitudes favourable for this Fe XXIII emission appear immediately during the beam onset and continue to exist after the beam offset while at 15-30 seconds from the event start the atmosphere is cooling to a few million K shown by the dark red and purple lines in Fig. 39a. The emission of He II line is expected to appear in this model a bit (30-50 seconds) later after the beam offset. By the time of 50 seconds, the hydrodynamic shock velocity is also reduced if heated by a mixed beam (see Fig.39c, left plot) or even this shock becomes returning to the pre-flare atmospheric level if heated by an electron beam (compare the left and right plots of Fig.39c).

The explosive evaporation of the plasma heated by a mixed beam starts from the very first seconds of observations with high macrovelocities of 100 $km{\cdot}s^{-1}$ (see paper 1 Zharkov et al. 2020), similar to the macrovelocities simulated in the lower flaring corona (Fig.40c, left column) for a mixed beam, and approaching the velocities of 400-500 $km{\cdot}s^{-1}$

DISTRIBUTION A: Distribution approved for public release. Distribution unlimited

only 5 seconds after the beam onset. Later these macrovelocities are reduced to 250 km/s at 30-50 s after the event onset when these magnitudes are observed by Fe XXIII line (shown in Fig. 37 and other plots in Zharkov et al, 2020). As shown in Zharkov et al, 2020, the spectrograms for the Fe XXIII 263.76 Å line for the event 1 occurring in FP3 of seismic source 1 reveals the large blue-shifted velocities of the upflows of 400 kms^{-1}, similar to the simulated velocities for heating by a mixed beam (blue line in Fig. 39c, left plot).

Moreover, for SQ2 the blue shifts in the line of Fe XXIII 263.76 Å show the macro-velocity of explosive evaporation exceeding 400 km/s much faster than in the atmosphere with SQ1 that indicates a stronger shock occurring in the location of SQ2, which, in turn, led to the observation of secondary ripples, or the additional ridge in time-distance diagram, constituting a double bounce of acoustic waves in the interior beneath the flare.

This is combined with the downflows of > 100-200 kms^{-1} seen in the He II spectrograms associated with SQ 1 and SQ2. The EIS observations in He II 256 Å in the locations of SQ1 and SQ 2 appear 30 s after the onset of FE1 confirming the starting time of the SQ1 and SQ2 20-25 s earlier than the red shift in He II line, which exists for about a minute shown in the first three bottom plots in Figs. 9 and the most three right plots in Fig.10 in Zharkov et al, 2020. It can be noted that this He II line captures first the downflows, which are followed in a minute or so by upflows with the magnitudes of macro velocities close to those predicted by the hydrodynamic (HD) simulations for the heating by a mixed beam (in SQ 1 and SQ 2) shown in Fig. 39 and 40 (left column). It can be seen that blue line shows the upwards macrovelocities in Fig. 39c and 40 approaching 400 km/s , similar to that measured in Zharkov et al, 2020 by the EIS instrument for the location of seismic source 1. At the same time, the downward motion modelled for this event also reaches the macrovelocity of 150- 200 km/s (purple line in Fig. 39).

However, the He II 256 Å spectrograms with Doppler velocity taken in the location of a largest sunquake described in Paper 1 reveal the red-shifts approaching several hundred kms^{-1}, similarly to the simulations shown In Fig. 39c, left plot, to appear 15-20 seconds after the plasma started cooling off to the temperature when He II emission becomes observable. The simulated and measured blue shifts start from 150 km/s approaching 300 km/s within a short timescale of 15-30 seconds . The observed red-shifts in excess of 250 kms^{-1} are well-correlated with the largest sunquake 2 in the footpoint FP4 associated with the green magnetic rope (see Fig. 32).

Also in the flaring event 2 the EIS in He II 254 Å observed both blue shifts up to two hundred kms^{-1} reported in Zharkov et al, 2020, while the red-shifts in excess of 150 kms^{-1} are well-correlated with the possible sunquake 5 and Hα kernel 3, which seem to have the similar heating and seismic response as it was in seismic source 2.

4.7.6.b. H-alpha line profiles

In general, the hydrodynamic radiative simulations of hydrogen emission show that during the flare at the very first seconds after the beam onset, Hα becomes an emission line revealing a strong increase of the central and wing emission caused by enhanced ionisation and excitation induced by energetic power-law electron beams (Druett et al. 2017; Druett & Zharkova 2018). Furthermore, in the very first seconds, Hα line profiles become strongly redshifted as shown in Fig. 41 calculated for different particle beam parameters, similar to what has been observed in the past in the other flaring events with spectral windows of ±8 Å (Ichimoto & Kurokawa 1984; Wuelser & Marti 1989).

By looking at the observed Hα-line profiles reported in paper 1 (Zharkov et al. 2020) we recognised that in kernels 2 and 3 the profiles are clear blue wings, a far wing in kernel 2 and a near wing in kernel 3. In kernel 1 the observed Hα line profile can be considered at

DISTRIBUTION A: Distribution approved for public release. Distribution unlimited

first to be the regular profile with self- absorption and strongly increased red horn in the line core re- ported previously for near stationary and slightly moving atmospheres (Ding & Fang 1996; Kuridze et al. 2015; Druett et al. 2017). However, it turns out that this is not the case because of the very strong intensity of the whole emission and, particularly, of the red wing of the profile, which is higher than the Hα line profiles even in the cores simulated for weaker beams. Furthermore, the observed Hα line intensity in kernel 1 is still increasing as it reaches the edge of the available wavelength window (+1.5Å). However, based on the features present in the observation profile, it is certainly likely that we observed the near blue wing of the line since the line may not be so greatly red-shifted as is in kernels 2 and 3.

For these reasons we calculated Hα-line profiles (Fig. 41) produced from hydrogen atoms by combined thermal and non-thermal excitation and ionisation by beam electrons in flaring atmospheres heated by: 1) mixed beam with the initial energy flux of 1.0×10^{13} erg·cm^{-2}·s^{-1} (model F13), spectral index 4 as derived for the flaring events 1 and 2 in paper 1 (Zharkov et al. 2020), and 2) by electron beams with much smaller initial energy fluxes of 1.0×10^{11} erg·cm^{-2}·s^{-1} (model F11) and 1.0×10^{10} erg·cm^{-2} ·s^{-1} (model F10) for the spectral index of 4, in case if the electron component in the mixed beam in kernel 1 was much smaller than in kernels 2 and 3.

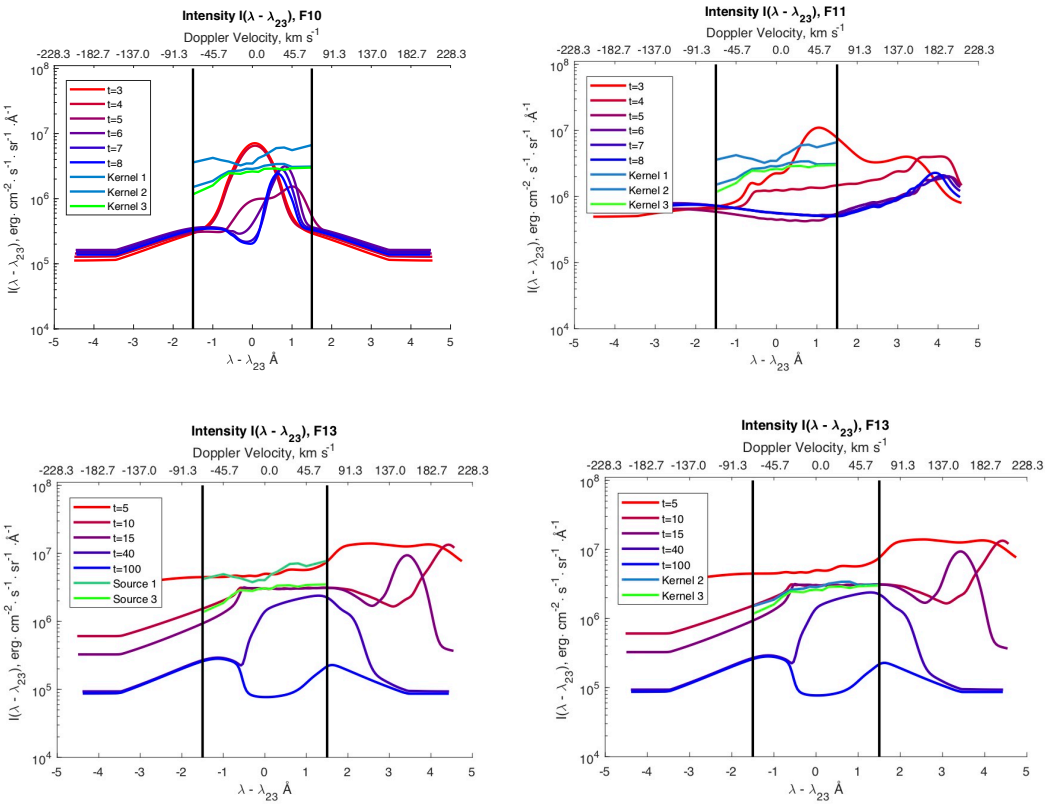


Figure 41. The observed Hα-line profiles in kernels 1-3 overplotted on the Hα line profiles simulated with HYDRO2GEN code (Druett & Zharkova 2018) in flaring atmospheres produced by: (a) an electron beam with spectral index 4 and the initial energy flux of 10^{10} $erg \cdot cm^{-2}s^{-1}$. (b) an electron beam with spectral index 4 and the initial energy flux of 10^{11} $erg \cdot cm^{-2}s^{-1}$; (c) a mixed beam with spectral index of 4 and initial energy flux of 10^{13} $erg \cdot cm^{-2}s^{-1}$; d) a mixed beam with the same parameters as in c). The observed Hα line profiles are shown in kernel 1 (blue line), kernel 2 (light blue line) and

DISTRIBUTION A: Distribution approved for public release. Distribution unlimited

kernel 3 (green line). The vertical lines shows the spectral window ±1.5 Å for the CRISP/SST Hα line observations.

The Hα line profiles simulated for the green rope footpoints in kernels 1 and 2 of flaring event 1 are based on the hydrodynamic models simulated for a mixed power-law particle beam F13 (see Fig. 39, left column) in the flaring atmosphere associated with the seismic source 1 (footpoint FP3 in the northern end of green rope in Fig.32) and with the seismic source 2 (footpoint FP4 in the southern end of green rope) as concluded by Zharkov et al, 2020.

The Hα-line profiles derived at kernels 1-3 are plotted in different colours on the top of model simulations of these profiles calculated for the atmosphere heating by beams with the initial energy fluxes relevant to models F10, F11 and F13 as shown in Fig. 41. It can be seen that the observed blue wings of Hα line profiles in all three Hα kernels only fit the model F13 at the times of 5 s (kernel 1) and 15 seconds (kernels 2 and 3), while the observed Hα blue wing intensities were much higher than those simulated for the HD models heated by the beams with lower energy fluxes (F10 or F11). The vertical lines show the spectral window of CRISP/SST which demonstrate the limits of the observations of Hα line profiles with the largely red- shifted cores.

The Hα-kernel 2, which occurred from 11:55:50 UT during the flaring event 1, is associated with seismic source 2. The red shift in the simulated Hα line profile of kernel 2 reaches a maximum of above 5-6 Å at 5 s, or just after a beam offset, when the downward velocity in a hydrodynamic model is maximal approaching 380 km·s^{-1} dropping below 300 km/s after 15 seconds (see Fig. 39c, right plot or Fig. 40 left plot.) The simulated Hα line profile is found to be strongly red-shifted by more than 5.0 Å from the central wavelength (λ = 6563 Å), corresponding to an averaged Doppler velocity of 268 $km \cdot s^{-1}$. The core of this Hα line profile cannot be observed by CRISP because it is strongly red-shifted far outside the CRISP spectral window of ±1.5 Å.

As result, we reckon the observed Hα-line profiles in the spectral window of ±1.5 Å shows only far blue wings of the Hα line, because the line is strongly red-shifted by the shock induced by a mixed beam with the high initial energy flux. Hence, the observed Hα-line profiles in kernel 2 is close to the simulations made for the F13 model about 15 seconds after the beam onset as shown in Fig. 41d with much lower intensity of this blue wing.

By comparing the observed Hα line profile in kernel 3 with the simulated ones shown in Fig. 41, we reckon that this footpoint F4 was heated by a powerful mixed beam with the initial energy flux about or above $(6-8) \cdot 10^{12}$ erg·cm^{-2} s^{-1} (still of the same order of magnitude as in Hα kernels 1 and 2).

4.7.6.c. Paschen continuum (WL) emission

The contribution functions for Paschen continuum responsible for white light emission are presented in Zharkova et al, 2020 assuming that in WL kernel 1 (Hα kernel 1) the emission is produced by the beam with initial energy flux of $(4-5) \times 10^{10}$ (F10) and the WL kernel 2 (Hα kernel 3) the WL emission is produced by the beam with the energy flux of 10^{13} (F13) (see Zharkova et al, 2020). By looking at the contribution functions of Paschen continuum produced by the beams F10 and F13 one can note that the intensity of this emission for the F13 beam is more then an order of magnitude higher than for the. model F10.

This is governed by a large opacity of Lyman continuum emission in F13 model (Druett & Zharkova 2019), which increases the intensity of all hydrogen continuum emission. In particular, Paschen continuum emission for the F13 beam is formed at deeper atmospheric

DISTRIBUTION A: Distribution approved for public release. Distribution unlimited

levels and has much longer existence compared to that induced by less powerful beam of the model F10 (see Fig. 42, Zharkova et al, 2020). Since the observations confirm the very intense and long- lasting white light emission of the flare of 6 September 2017 combined with the fit of Hα line profiles in the kernels for FE1 and FE2, we can confirm that the optical emission in this flare was produced by a very intense beam.

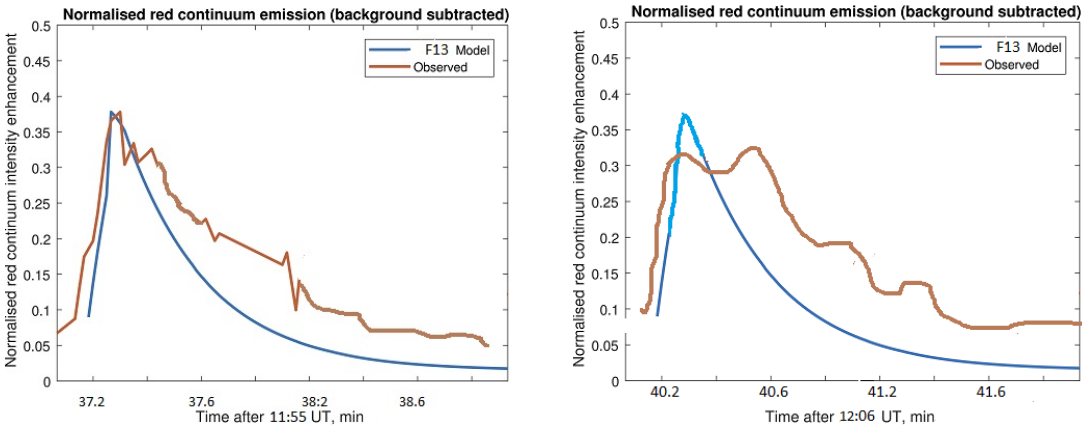


Figure 42. Simulated variations of the contribution functions of Paschen continuum (white light emission) derived from a radiative hydrodynamic model heated by the moderate electrons beam, model F10 (a) and by powerful mixed beam, model F13 (b) (see the text for more detail). Note the three orders of magnitude difference between the intensities in the model (F10) and (F13) plots. The comparison of the light curve of intensity of Paschen emission generated by a mixed beam with spectral index of 4 and the initial energy flux of 1×10^{13} $erg/cm^2/s$ with that measured from HMI/SDO images in the WL kernel 1 coinciding with Hα kernel 1 (c) and in the WL kernel 2 coinciding with Hα kernel 3 (d).

The emission in the first WL kernel (Fig. 42, left) is likely to be caused by a weak beam as derived from kernel 1 of Hα emission in section 3.2, whose line profile is likely produced by the rather weak beam. While the second white light kernel 2 (Fig. 42, right) was co-spatial to the *Hα* kernel 3 in flaring event 2 associated with a much stronger electron beam injected after 12:06:40 UT. The electron beam in the flaring event 2 produces stronger ionisation of the ambient hydrogen and stronger Lyman continuum, which controls the continuous hydrogen emission in flaring atmosphere, affecting, in turn, the intensity and duration of the Balmer and Paschen continua via the opacity of Lyman continuum (Druett & Zharkova 2019).

4.7.7. Interpretation of seismic emission with the shocks deposited in these two flares

Propagation of the acoustic waves (or rays) generated by a supersonic source (shock generated in flaring atmosphere) moving with an average velocity 120 km s^{-1} under the angle of 0° to the vertical (seismic source 1) is shown in Fig. 43 in Zharkova et al, 2020, and with average velocity of 200 km s^{-1} at surface depth z_S = 0 km -30 (as in seismic source 2) and in Fig. 44 in Zharkova et al, 2020 with the average velocity 150 km s^{-1} under the angle of $+30^{\circ}$(seismic source 3). The abscissa defines a horizontal distance in Mm of the ray propagation about the location of a deposition of supersonic disturbance (shock) and the ordinate shows a propagation depth, *z*, under the photosphere of the generated rays and

DISTRIBUTION A: Distribution approved for public release. Distribution unlimited

wavefronts at different times are shown in Figs. 44 and 45 for the wave vectors located in the same plane as velocity, i.e. if $\phi = 0$ (in notation of Section 5.2 by Zharkov 2013).

For the seismic model for SQ 2 shown in Fig. 43, the shock caused by the mixed beam is deposited at the surface and propagates much deeper into the interior (as shown in the video attached with the paper in supplementary materials) so that the acoustic wave produced by this shock moves into much deeper interior now under the angle -30° producing acoustic rays in the shortest path on the right hand side and the longest one on the left hand side. Since the acoustic rays travel much deeper into the interior, they gain much higher velocity before reaching the lower turning points than in the previous case described above. These rays when reflected back to the surface by Fermat principle (Zharkov 2013) will have much higher velocities and, when they approach the photosphere in the upper turning point, they create larger ripples, which can be easily detected in the time-distance diagrams as reported for seismic source 2 shown in Zharkov et al, 2020.

The other two seismic sources in flare 6 September 2017 show the rays characteristics consistent with being produced by shocks generated by mixed electron and proton beams and deposited at angles (0-10)° (source 1) and +30° (source 3) to the local vertical, which propagate beneath the surface but not too deep into the interior, contrary to type 1 acoustic waves in seismic source 2.

The weaker shock deposited first above the quiet Sun photosphere and propagating in the solar interior for shorter time was created during flare of 6 September 2011 since it has been created by electron beam. The weaker acoustic waves at shallower depths of the interior (see Figure 44), which are reflected by the interior to the solar surface (at lower turning points) with smaller velocities. When these acoustic waves reach the solar surface (photosphere) and become reflected by it (at the upper turning point), they create much smaller ripples in the photosphere, which can be only picked up as regular features by the holographic approach.

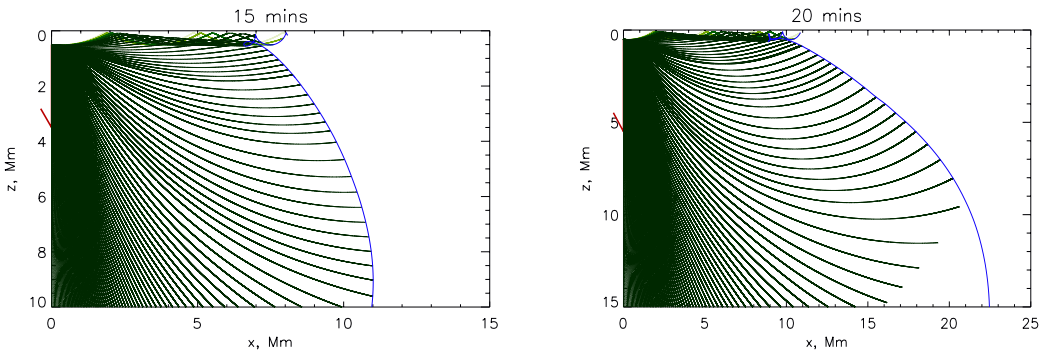


Figure 43. The individual acoustic rays travelling to the bottom of the plot generated in the interior by a moving supersonic source with average speed of v = 175 km s^{-1} like in the seismic source 2 at the times denoted on the top. The shock is inclined by -30° to the local vertical. Z is depth in the solar interior, the photosphere is denoted by Z=0, the X-axis denotes a distance in Mm from the point of the momentum deposition. The mustard arrow shows the direction of the wave propagation. The points of reflection from the surface are observed at 15 minutes after the deposition time starting from a distance 2 Mm (on the right) and very well seen in 20 minutes at distance starting from 3-4 Mm. The second bounce waves are appearing at 5 Mm in 15 minutes after the shock deposition and at 7 Mm in 20 minutes (see the the top far end of the wave set marked by the blue curve). Note, a video animation of these acoustic waves is presented in the supplementary materials showing

DISTRIBUTION A: Distribution approved for public release. Distribution unlimited

propagation of the generated acoustic waves with the first and second bounces as observed in seismic source 2.

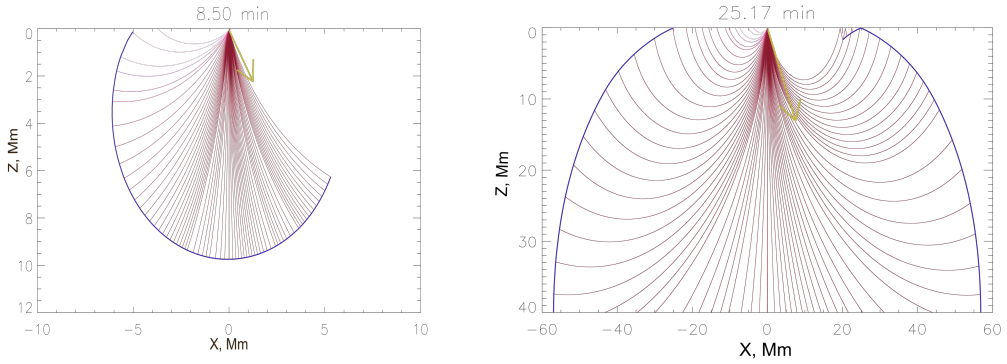


Figure 44. The individual acoustic rays generated by shock in the interior and travelling to the bottom of the plot) by a moving supersonic source with velocity v = 100 km s^{-1} , depositing a momentum below the photosphere under +30 ° angle from the local vertical for the times after the shock deposition shown above the plots. *Z* is depth in the solar interior, the photosphere is denoted by Z=0, the X-axis denotes a distance in Mm from the point of the momentum deposition. The mustard arrow shows the direction of the wave propagation. The points of ray reflection from the photosphere seen after 8:50 min in the left top corner are observed as ripples on the surface, or a sunquake, propagating outward the central point of the momentum deposition.

4.7.8. General conclusions on energy transport by energetic particles

Based on the parameters of the seismic events derived from observations, we apply a combination of two hydrodynamic models: one for a flaring atmosphere heating by a mixed beam and second one for production of acoustic waves in the solar interior by the shock coming from the flaring atmosphere for three seismic sources 1, 2 and 3. in order to demonstrate a role of the magnitude and deposition angle of the shock as well as a depth of the shock deposition in the solar interior on the resulting seismic signatures. These models provide the plausible quantitative interpretation of the seismic signatures associated with the hydrodynamic shocks caused by mixed and electron beam injection in flaring events of this flare.

The simulations show that the explosive evaporation of the plasma heated by a mixed beam starts from the very first seconds with high macrovelocities of 100 km·s^{-1} similar to that simulated in the lower flaring corona (Fig.39c, left column), and approaching the velocities of 400-500 km·s^{-1} at 5 seconds after the beam onset, which later are reduced to 250 km/s at 30- 50 s after the event onset. However, observations by Fe XXIII line only started 10-15 seconds after the beam onset, when the beam was off after 10 second and plasma was cooled off to the temperature of few millions K required to see this emission. The spectrograms of the Fe XXIII 263.76 Å line for the FE1 in the footpoint FP3 of SQ 1 reveal large upward velocities of 300-350 kms^{-1}, similar to the simulated velocities in the hydrodynamic model of flaring atmosphere heated by the mixed beam.

For SQ2 the blue shift in the line of Fe XXIII 263.76 Å, indicating the macro-velocity of explosive evaporation exceeds 400 km/s much faster than in the atmosphere with SQ1 that indicates a stronger shock in the location of SQ2, which was likely to lead to the additional ridge in time distance diagram of sunquake 2 constituting a double bounce of acoustic

DISTRIBUTION A: Distribution approved for public release. Distribution unlimited

waves. These upward motions are combined with the downflows of > 100-200 kms^{-1} seen in the He II spectrograms associated with SQ 1 and SQ2. However, the EIS observations in He II 256 Å in the locations of SQ1 and SQ 2 appear 30 s after the onset of FE1 confirming that the temperature of flaring atmosphere reached the magnitudes of radiative temperature of He II line. To this point also indicate he starting time of the SQ1 and SQ2, which is 20-25 s earlier than the red shift in He II line. Although, the red shift in He II line exists for about a minute that is close to that predicted by hydrodynamic simulations. What is remarkable that after a minute or so these downflows are followed by upflows with the magnitudes of macrovelocities close to those predicted by the hydrodynamic (HD) simulations carried out for heating by a mixed beam (in SQ 1 and SQ 2).

It can be observed that the upwards macrovelocities in the HD model approach 300-400 km/s, similar to those measured by the EIS instrument for the location of seismic source 1. At the same time, the downward motion modelled for this event also reaches the macrovelocity of 300 km/s at 5 seconds after the beam onset and then is reduced to 150-200 km/s for the next few minutes. These red shifts are close to that measured in Hα kernel 1 which was likely to be red-shifted by 3-4 Å, so only the blue wing of the line has been observed. At the same time, the He II 256 Å spectrograms in the location of a largest sunquake 2 reveal that similarly to the hydrodynamic simulations the red- shifts approaching 380 kms^{-1} dropping to 250-300 km/s 15-20 seconds after the beam offset. The observed He II red-shifts in excess of 250 kms^{-1} are well-correlated with those observed in the locations of the largest sunquake 2. This red shift also corresponds to the strong one of 5-6 |*AA* measured in Hα kernel 2, where only the far blue wing is observed with the intensity lower than that in Hα kernel 1. The simulated and measured blue shifts in SQ2 and Fe XXIII line start from 150 km/s at 1 second approaching 400 km/s within a short timescale of 15-30 seconds.

We also investigate the scenario of acoustic wave genera- tion by hydrodynamic shocks propagating for up 50-60 seconds in the solar interior with supersonic velocities and generating acoustic waves above the acoustic cutoff frequency. During the flare of 6 September 2017 the shocks in the SQs 1-3 were deposited beneath the solar surface and travelled much longer in the interior producing acoustic waves compared to the shock generated in the flare of 6 September 2011 reported earlier (Macrae et al. 2018). This difference in the shock deposition depths explain the clear ridges observed in the time-distance diagrams of SQ1, SQ2 and SQ3 in the 6 September 2017 (Zharkov et al, 2020) flare versus the rather weak ridge observed in the 2011 flare (Zharkova et al, 2020).

The acoustic waves (rays) generated by the HD shock induced by a mixed beam (MB) in the largest sunquake (source 2) are found to travel much faster and to deposit their momen-tum much deeper in the solar interior producing acoustic waves of type 1 with the double ridges: a very visible main ridge and a detectable second-bounce ridge. The shocks deposited by an electron beam (EB) produce acoustic waves of type 2 with a weaker single ridge as seen in the seismic sources 1 and 3. As a result, these acoustic waves of type 1 reach the first lower turning point in deeper interior depths, thus, gaining higher ve- locities compared to the waves of type 2. These type 1 acoustic waves approach higher velocities in the interior, with which they travel back to the surface in the photosphere to their first upper turning point (or first bounce) creating ripples while being reflected back to the interior. The reflected wave energy is lower than the original one but sufficient to travel again to the less deep interior and to return back for a second bounce creating secondary, slower, ripples.

DISTRIBUTION A: Distribution approved for public release. Distribution unlimited

The acoustic waves of type 1 simulated in the seismic source 2 for a momentum deposited at an angle of -30° from the vertical and travels rather deep into the solar interior demonstrate the occurrence of strong acoustic waves in the interior. These waves become reflected from the solar surface during the first bounce (or turning point), thus, forming well detectable ripples at t the photosphere a few minutes after the impact at a distance approaching 5-10 Mm from the source that is in a close agreement with the distance and time derived from the TD diagram. There are also the second bounce acoustic waves seen in the simulated wave packets occurring at the second up- per turning point at the photosphere showing them to start at 5 Mm in the model set at 15 minutes and at 7 Mm in the model set at 20 minutes that is also close to the parameters derived from the TD diagram for seismic source 2.

The other two sources show the acoustic waves, whose characteristics are consistent with those being produced by shocks generated by slightly weaker mixed beams and de- posited at angles of 0° (seismic sources 1) and +30° (source 3) to the local vertical, which propagate beneath the surface but not too deep into the interior, contrary to type 1 acoustic waves in source 2.

Hence, by combining the two hydrodynamic models: of flaring atmosphere and acoustic wave generation in the solar interior, we are able to provide the simultaneous quantitative interpretation of the three seismic events whose characteristics were also confirmed with blue and red shifts derived from the combined with EUV and Hα emission observed in the X9.3 flare of 6 September 2017.

5. Conclusions

In this project we investigated energetic particles in the Sun and heliosphere associated with flares, eruption of fast coronal mass ejections (CMEs) and reacceleration in the solar wind. The scenario of particle acceleration and parameters gained by these energetic particles (energy spectra, pitch angle distributions) and links to magnetic field topologies where they were energized. These characteristics are of a great interest for many researchers and space industry as they define space weather in the heliosphere.

These energetic particles reveal very peculiar distributions in velocities and pitch angles not anticipated by regular models of stochastic particle acceleration by turbulence or shocks. We carried out a revision of the existing particle acceleration models with the emphasis on their links to magnetic reconnection processes occurring in the Sun and heliosphere and derived particle parameters (energy, directivity, pitch angle distribution) during their passage through reconnecting current sheets occurring in the solar corona (eruptive flares) and in the heliosphere. The investigation of particle acceleration was carried out with a 3D Particle-in-cell PIC approach combined with a 3D test particle (TP) approach. The consequent transport effects of particle propagation in the solar atmosphere were studied by testing flaring atmosphere parameters with simulated hydrodynamic models of flaring atmospheres heated by energetic particles (electrons, protons and their mixture) and resulting seismic signatures on the solar surface caused by these hydrodynamic shocks induced by accelerated particles.

1. We confirmed separation of electrons from ions/protons during acceleration in reconnecting current sheets with and without magnetic islands depending on a magnetic field topology, magnitude of guiding magnetic field, occurrence of single or multiple X-nullpoints (magnetic islands).

a) Explained a role of polarization electric field on velocity profiles of ions in the solar wind crossings of the HCS and other current sheets.

DISTRIBUTION A: Distribution approved for public release. Distribution unlimited

b) Explained formation of electron clouds about current sheets caused by slower acceleration of protons/ions and their longer presence in the current sheet midplanes that makes electrons to return to current sheets and become re-accelerated again. This mechanism explains the occurrences of loop top sources of hard X-Ray emission often observed in solar flares with CMEs.

c) Explained occasional full spatial separations into opposite loop legs of interacting magnetic loops of hard X-ray (electrons) and gamma-ray emission (protons/ions) observed in a few large solar flares.

d) argued about a natural presence of ions and electrons in most flares because of at partial separation of ions from electrons at the injection into different legs of interacting loops.

2. Discovered that magnetic islands in current sheets are much more effective accelerators than a current sheets with a single X-nullpoint and evaluated the key mechanisms of acceleration in different magnetic islands (squashed or coalescent).

a) Particles inside magnetic islands are accelerated at X-nullpoints creating Fermi type 2 acceleration.

b) Particles are accelerated to higher energies in squashed magnetic islands than in coalescent ones.

c) Electrons are shown to form clouds at X-nullpoints between magnetic islands.

3. We discovered that during passing current sheets there are the two populations (low and high energy) of energetic electrons, which have essentially different energy and pitch angle distributions. We confirmed this discovery with thee in-situ observations of solar wind particles obtained with payload of ACE, WIND and STEREO spacecrafts. This allowed to explain:

a) strahls (energetic electron jets) (transit electrons) often observed in the solar wind which can be seen moving either towards the Sun and perpendicular to the interplanetary magnetic field;

b) electron flux dropouts (bounced electrons) also often observed in the solar wind;

c) different pitch angle distributions revealed for strahls and dropouts and different directions of spacecraft crossings current sheets with single and multiple X-nullpoints.

4. We investigated the turbulence generated in current sheets by accelerated particles and evaluated the types of turbulence induced in different parts of current sheets.

5. We investigated the efficiency of particle acceleration during a CME ejection for breakout model and demonstrated:

a) Flare current sheets are more effecting particle accelerators than breakout current sheets formed at the front of a CME.

b) Flare current sheets forming helmet type magnetic structures which initiate flares and release the highest energy during impulsive phase of the flare.

c) The most effective acceleration mechanisms are found to be magnetic curvature in islands and betatron acceleration in helmet structures.

6. We investigated particle transport in flaring atmospheres in the Sun for two flares observed during solar maximum (2011) and minimum (2017) with rather different coverage of multi-wavelength observations. We discovered:

a) The flare occurred during a solar maximum (2011) agrees well with being ignited by the injection of powerful hard electron beam, while the flare occurred during solar minimum (2017) appeared to have strong mixed beam combining a contribution of ions/protons and electrons.

b) The heating produced by mixed beam was much stronger at the coronal level and formed a shock much deeper in the flaring atmosphere than that by electron beam.

c) Macrovelocities of upward motion in the corona and downward motion to the photosphere and solar interior were much higher if the flaring atmosphere is heated by a

DISTRIBUTION A: Distribution approved for public release. Distribution unlimited

mixed beam than by an electron one.

d) The different deposition momenta and depths of the shocks produced in flaring atmospheres by mixed and electron beams are shown to lead to rather different seismic signatures detected in the flare of 2011 and 2017. The 2011 flare had smaller ripples, which were even missed by previous studies, while in the flare of 2017 the ripples were the highest ever observed revealing also for the first time the occurrence of second bounce ripples.

e) These different signatures of particle transport in flaring atmospheres can indicate to more twisted magnetic loops interacting during solar minima thus creating favorable conditions for acceleration of ions/protons compared to solar maxima when magnetic field in the loops is less twisted according to dynamo models.

The comparison of the multiwavelength observations of eruptive flares with simulations with radiative hydrodynamic models for flaring atmospheres and hydrodynamic models of the acoustic wave generation in the solar interior and their detection as ripples on the solar surface allows to obtain an important breakthrough in understanding particle transport from reconnection sites where they are generated through the flaring atmosphere down to the solar interior.

DISTRIBUTION A: Distribution approved for public release. Distribution unlimited

6. References

Adhikari, L., Khabarova, O., Zank, G. P., & Zhao, L.-L. 2019, ApJ, 873, 72
Allred, J. C., Hawley, S. L., Abbett, W. P., & Carlsson, M. 2005, ApJ, 630, 573
Anderson, B. R., Skoug, R. M., Steinberg, J. T., & McComas, D. J. 2012, JGR, 117, 2011JA017269
Angelopoulos, V., McFadden, J. P., Larson, D., et al. 2008, Science, 321, 931
Antonucci, E., Gabriel, A. H., Acton, L. W., et al. 1982, Sol. Phys., 78, 107
Aptekar, R. L., Frederiks, D. D., Golenetskii, S. V., et al. 1995, Space Sci. Rev., 71, 265
Ball, D., Sironi, L., & Özel, F. 2018, The Astrophysical Journal, 862, 80
Bárta, M., Büchner, J., Karlický, M., & Skála, J. 2011, ApJ, 737, 24
Battaglia, M., & Kontar, E. P. 2012, ApJ, 760, 142
Baumann, G., & Nordlund, Å. 2012, ApJ, 759, L9 Benz, A. O. 2017, Living Reviews in Solar Physics, 14, 2
Bessho, N., & Bhattacharjee, A. 2012, The Astrophysical Journal, 750, 129
Birn, J., Battaglia, M., Fletcher, L., Hesse, M., & Neukirch, T. 2017, ApJ, 848, 116
Benz, A. O. 2017, Living Reviews in Solar Physics, 14, 2
Boris, J. P. 1970, Proceeding of Fourth Conference on Numerical Simulations of Plasmas
Bowers, K. J., Albright, B. J., Yin, L., Bergen, B., & Kwan, T. J. T. 2008, Physics of Plasmas, 15, 055703
Bradshaw, S. J. & Cargill, P. J. 2006, A&A, 458, 987
Brown, J. C. 1971, Sol. Phys., 18, 489
Buitrago-Casas, J., Martinez-Oliveros, J., Lindsey, C., et al. 2015, solphys, 290, 3151
Buneman, O. 1958, Phys. Rev. Lett., 1, 8
Canfield, R. C. & Gayley, K. G. 1987, ApJ, 322, 999
Cerutti, B., Werner, G. R., Uzdensky, D. A., & Begelman, M. C. 2013, ApJ, 770, 147
Cerutti, B., Werner, G. R., Uzdensky, D. A., & Begelman, M. C. 2014, ApJ, 782, 104
Chen, L.-J., Bhattacharjee, A., Puhl-Quinn, P. A., et al. 2008, Nature Physics, 4, 19
Chian, A. C.-L., & Muñoz, P. R. 2011, ApJ, 733, L34
Christensen-Dalsgaard, J., Dappen, W., Ajukov, S. V., et al. 1996, Science, 272, 1286
Cox, D. P. & Tucker, W. H. 1969, ApJ, 157, 1157
Crooker, N. U., Huang, C.-L., Lamassa, S. M., et al. 2004, JGR, 109, doi:10.1029/2003JA010170
Crooker, N. U., Larson, D. E., Kahler, S. W., Lamassa, S. M., & Spence, H. E. 2003, Geophys. Res. Lett., 30, 1619
Crooker, N. U., & Pagel, C. 2008, Journal of Geophysical Research: Space Physics, 113,
Culhane, J. L., Harra, L. K., James, A. M., et al. 2007, Sol. Phys., 243, 19
Dahlin, J. T., Drake, J. F., & Swisdak, M. 2014, Physics of Plasmas, 21, 092304
Dahlin, J. T., Drake, J. F., & Swisdak, M. 2015, Physics of Plasmas, 22, 100704
—. 2017, Physics of Plasmas, 24, 092110
Daughton, W. 1999, Physics of Plasmas, 6, 1329
Daughton, W., Roytershteyn, V., Karimabadi, H., et al. 2011, Nature Physics, 7, 539
Ding, M. D. & Fang, C. 1996, Sol. Phys., 166, 437
Dominique, M., Hochedez, J.-F., Schmutz, W., et al. 2013, Sol. Phys., 286, 21
Donea, A. 2011, Space Sci. Rev., 158, 451
Donea, A. & Lindsey, C. 2005, ApJ, 630, 1168
Donea, A.-C., Besliu-Ionescu, D., Cally, P. S., Lindsey, C., & Zharkova, V. V. 2006, Solar Physics, 239, 113
Donea, A.-C., Braun, D. C., & Lindsey, C. 1999, ApJ, 513, L143
Donea, A.-C., Lindsey, C., & Braun, D. C. 2000, Sol. Phys., 192, 321
Doschek, G. A., Kreplin, R. W., & Feldman, U. 1979, ApJ, 233, L157
Doschek, G. A., McKenzie, D. E., & Warren, H. P. 2014, ApJ, 788, 26
Drake, J. F., Kleva, R. G., & Mandt, M. E. 1994, Phys. Rev. Lett., 73, 1251
Drake, J. F., Opher, M., Swisdak, M., & Chamoun, J. N. 2010, ApJ, 709, 963
Drake, J. F., Swisdak, M., Cattell, C., et al. 2003, Science, 299, 873
Drake, J. F., Swisdak, M., Che, H., & Shay, M. A. 2006a, Nature, 443, 553
Drake, J. F., Cassak, P. A., Shay, M. A., Swisdak, M., & Quataert, E. 2009, Ap. J., 700, L16
Drake, J. F., Swisdak, M., & Fermo, R. 2012, The Astrophysical Journal, 763, L5
Drake, J. F., Swisdak, M., Schoeffler, K. M., Rogers, B. N., & Kobayashi, S. 2006b, Geophys. Res. Lett., 33, L13105
Druett, M., Scullion, E., Zharkova, V., et al. 2017, Nature Communications, 8, 15905
Druett, M. K. & Zharkova, V. V. 2018, A&A, 610, A68
Druett, M. K. & Zharkova, V. V. 2019, A&A, 623, A20
Duijveman, A., Somov, B. V., & Spektor, A. R. 1983, Sol. Phys., 88, 257
Egedal, J., Le, A., & Daughton, W. 2013, Physics of Plasmas, 20, 061201
Egedal, J., Øieroset, M., Fox, W., & Lin, R. P. 2005, Phys. Rev. Lett., 94, 025006
Eyink, G. L. 2015, ApJ, 807, 137
Fisher, G. H., Canfield, R. C., & McClymont, 1985a, ApJ, 289, 414
Fisher, G. H., Canfield, R. C., & McClymont, 1985b, ApJ, 289, 425
Fisher, G. H., Canfield, R. C., & McClymont, 1985c, ApJ, 289, 434
Feuerstein, W. M., Larson, D. E., Luhmann, J. G., et al. 2004, Geophys. Res. Lett., 31, L22805
Foullon, C., Lavraud, B., Wardle, N. C., et al. 2009, Sol. Phys., 259, 389
Fu, H. S., Khotyaintsev, Y. V., André, M., & Vaivads, A. 2011, Geophys. Res. Lett., 38, L16104
Fu, H. S., Khotyaintsev, Y. V., Vaivads, A., Retinò, A., & André, M. 2013, Nature Physics, 9, 426
Fujimoto, M., Nakamura, M. S., Shinohara, I., et al. 1997, Geophys. Res. Lett., 24, 2893
Gordovskyy, M., & Browning, P. K. 2012, Sol. Phys., 277, 299
Gordovskyy, M., Zharkova, V. V., Voitenko, Y. M., & Goossens, M. 2005, Advances in Space Research, 35, 1743
Green, L. M., Valori, G., Zuccarello, F. P., et al. 2017, ApJ, 849, 40
de Gouveia Dal Pino E. M., & Lazarian, A. 2005, A&A, 441, 845
Gosling, J. T., Baker, D. N., Bame, S. J., et al. 1987, JGR, 92, 8519

DISTRIBUTION A: Distribution approved for public release. Distribution unlimited

Gosling, J. T., McComas, D. J., Skoug, R. M., & Smith, C. W. 2006, GRL, 33, L17102
Gosling, J. T. 2007, ApJ, 671, L73
—. 2008, Proceedings of the International Astronomical Union, 4, 367–377
Gosling, J. T., de Koning, C. A., Skoug, R. M., Steinberg, J. T., & McComas, D. J. 2004a, JGR, 109, A05102
Gosling, J. T., Eriksson, S., & Schwenn, R. 2006, JGR, 111,
Gosling, J. T., & Phan, T. D. 2013, ApJ, 763, L39
Gosling, J. T., Skoug, R. M., McComas, D. J., & Mazur, J. E. 2004b, ApJ, 614, 412
Graham, G. A., Rae, I. J., Owen, C. J., et al. 2017, JGR, 122, 3858.
Guo, F., Li, H., Daughton, W., & Liu, Y.-H. 2014, Physical Review Letters, 113, 155005
Hesse, M., Kuznetsova, M., & Birn, J. 2001, J. Geophys. Res., 106, 29831
Holman, G. D., Aschwanden, M. J., Aurass, H., et al. 2011, Space Sci. Rev., 159, 107
Hochedez, J.-F., Schmutz, W., Stockman, Y., et al. 2006, Advances in Space Research, 37, 303
Horaites, K., Boldyrev, S., & Medvedev, M. V. 2018, MNRAS, 484, 2474
Hoshino, M. 2012, Phys. Rev. Lett., 108, 135003
Huang, Y.-M., & Bhattacharjee, A. 2010, Physics of Plasmas, 17, 062104
Huang, S. Y., Sahraoui, F., Retino, A., et al. 2016, GRL, 43, 7850.
Hudson, H., Fisher, G., & Welsch, B. 2008, in Astronomical Society of the Pacific Conference Series, Vol. 383, Subsurface and Atmospheric Influences on Solar Activity, ed. R. Howe, R. Komm, K. Balasubramaniam, & G. Petrie, 221
Hurford, G. J., Krucker, S., Lin, R. P., et al. 2006, ApJ, 644, L93
Hurford, G. J., Schwartz, R. A., Krucker, S., et al. 2003, ApJ, 595, L77
Jaroschek, C. H., Treumann, R. A., Lesch, H., & Scholer, M. 2004, Physics of Plasmas, 11, 1151
Ichimoto, K. & Kurokawa, H. 1984, Sol. Phys., 93, 105
Inoue, S., Shiota, D., Bamba, Y., & Park, S.-H. 2018, ApJ, 867, 83
Ivanov, V. V. & Serbin, V. M. 1984, Soviet Ast., 28, 405
Kahler, S., & Lin, R. P. 1994, Geophys. Res. Lett., 21, 1575
Kahler, S. W., & Lin, R. P. 1995, Sol. Phys., 161, 183
Kaempfer, N. & Magun, A. 1983, ApJ, 274, 910
Karimabadi, H., Dorelli, J., Roytershteyn, V., Daughton, W., & Chacón, L. 2011, Physical Review Letters, 107, 025002
Kennedy, M. B., Milligan, R. O., Allred, J. C., Mathioudakis, M., & Keenan, F. P. 2015, A&A, 578, A7
Khabarova, O., Zank, G. P., Li, G., et al. 2015, ApJ, 808, 181
Khabarova, O., Zharkova, V., Xia, Q. & Malandraki, Q., 2020, ApJL 849, L12
Khabarova, O. V., & Zank, G. P. 2017, ApJ, 843, 4
Khabarova, O. V., Zank, G. P., Malandraki, O. E., et al. 2017, Sun and Geosphere, 12, 23 Kliem, B. 1994, ApJS, 90, 719
Kliem, B. 1994, ApJS, 90, 719
Kobylinskii, V. A. & Zharkova, V. V. 1996, Advances in Space Research, 17, 129
Kosovichev, A. 2011, preprint arXiv:1103.1707
Kosovichev, A. G. & Zharkova, V. V. 1998, Nature, 393, 317
Kotrč, P., Procha´zka, O., & Heinzel, P. 2016, Sol. Phys., 291, 779
Kowal, G., Lazarian, A., Vishniac, E. T., & Otmianowska-Mazur, K. 2012, Nonlinear Processes in Geophysics, 19, 297
Kuridze, D., Mathioudakis, M., Simo˜es, P. J. A., et al. 2015, ApJ, 813, 125
Kurokawa, H., Takakura, T., & Ohki, K. 1988, PASJ, 40, 357
Kurth, W. S., Gurnett, D. A., Scarf, F. L., & Poynter, R. L. 1984, Nature, 312, 27
Lapenta, G. 2008, Phys. Rev. Lett., 100, 235001
Lapenta, G., & Brackbill, J. U. 1997, J. Geophys. Res., 102, 27099
Lapenta, G., Markidis, S., Goldman, M. V., & Newman, D. L. 2015, Nature Physics, 11, 690
Lazarian, A., Vlahos, L., Kowal, G., et al. 2012, Space Sci. Rev., 173, 557
Lemen, J. R., Title, A. M., Akin, D. J., et al. 2011, Sol. Phys., 241
le Roux, J. A., Zank, G. P., Webb, G. M., & Khabarova, O. 2015, ApJ, 801, 112
le Roux, J. A., Zank, G. P., Webb, G. M., & Khabarova, O. V. 2016, ApJ, 827, 47
Li, X., Guo, F., Li, H., Stanier, A., & Kilian, P. 2019, ApJ, 884, 118
Li, X., Guo, F., Li, H., & Birn, J. 2018, The Astrophysical Journal, 855, 80
Li, Y., & Lin, J. 2012, Sol. Phys., 279, 91
Li, Y., Wu, N., & Lin, J. 2017, A&A, 605, A120
Lin, R. P., Dennis, B. R., Hurford, G. J., et al. 2002, Sol. Phys., 210, 3
Lin, R. P., Krucker, S., Hurford, G. J., et al. 2003, ApJ, 595, L69
Lindsey, C. & Braun, D. 2000, solphys, 192, 261
Lindsey, C. & Braun, D. C. 1999, ApJ, 510, 494
Litvinenko, Y. E. 1996, ApJ, 462, 997
Liu, C., Deng, N., Lee, J., et al. 2014, Apj, 795, 128
Liu, W., Li, H., Yin, L., et al. 2011, Physics of Plasmas, 18, 052105
Loureiro, N. F., Cowley, S. C., Dorland, W. D., Haines, M. G., & Schekochihin, A. A. 2005, Physical Review Letters, 95, 235003
Lysenko, A. L., Anfinogentov, S. A., Svinkin, D. S., Frederiks, D. D., & Fleishman, G. D. 2019, ApJ, 877, 145
Macrae, C., Zharkov, S., Zharkova, V., et al. 2018, A&A, 619, A65
Manapat, M., Øieroset, M., Phan, T. D., Lin, R. P., & Fujimoto, M. 2006, Geophys. Res. Lett., 33, L05101
Manchester, W. B., Kozyra, J. U., Lepri, S. T., & Lavraud, B. 2014, JGR, 119, 5449
Markidis, S., Lapenta, G., Divin, A., et al. 2012, Physics of Plasmas, 19, 032119
Markidis, S., Henri, P., Lapenta, G., et al. 2012, Nonlinear Processes in Geophysics, 19, 145
Marťınez-Oliveros,J.-C.,Hudson,H.S.,Hurford,G.J.,etal. 2012, ApJ, 753, L26
Matthews, S. A., Harra, L. K., Zharkov, S., & Green, L. M. 2015, ApJ, 812, 35
Matthews, S. A., Zharkov, S., & Zharkova, V. V. 2011, ApJ, 739, 71
McComas, D. J., Gosling, J. T., Phillips, J. L., et al. 1989, J. Geo- phys. Res., 94, 6907
Milligan, R. O. 2015, Sol. Phys., 290, 3399
Milligan, R. O., Kerr, G. S., Dennis, B. R., et al. 2014, ApJ, 793, 70

DISTRIBUTION A: Distribution approved for public release. Distribution unlimited

Malandraki, O., Khabarova, O., Bruno, R., et al. 2019, ApJ, 881, 116
Matthaeus, W. H., Ambrosiano, J. J., & Goldstein, M. L. 1984, Phys. Rev. Lett., 53, 1449
Melzani, Mickaël, Walder, Rolf, Folini, Doris, Winisdoerffer, Christophe, & Favre, Jean M. 2014, A&A, 570, A111
Muñoz, P. A., & Büchner, J. 2018, Phys. Rev. E, 98, 043205
Nalewajko, K., Uzdensky, D. A., Cerutti, B., Werner, G. R., & Begelman, M. C. 2015, The Astrophysical Journal, 815, 101
Nishizuka, N., Cowley, & Shibata, K. 2013, Physical Review Letters, 110, 051101
Nishizuka, N., Karlický, M., Janvier, M., & Bárta, M. 2015, ApJ, 799, 126
Øieroset, M., Lin, R. P., Phan, T. D., Larson, D. E., & Bale, S. D. 2002, Phys. Rev. Lett., 89, 195001
Oka, M., Phan, T.-D., Krucker, S., Fujimoto, M., & Shinohara, I. 2010, ApJ, 714, 915
Oka, M., Phan, T.-D., Øieroset, M., & Angelopoulos, V. 2016, JGR, 121, 1955.
Olshevsky, V., Lapenta, G., & Markidis, S. 2013, Phys. Rev. Lett., 111, 045002
Owens, M. J., Crooker, N. U., & Lockwood, M. 2013, JGR, 118, 1868
Quinn, S., Reid, A., Mathioudakis, M., et al. 2019, ApJ, 881, 82
Pagel, C., Crooker, N. U., Larson, D. E., Kahler, S. W., & Owens, M. J. 2005, JGR, 110, A01103
Parker, E. N. 1957, Physical Review, 107, 924
Petrosian, V. 2012, Space Sci. Rev., 173, 535
Phan, T. D., Bale, S. D., Eastwood, J. P., et al. 2020, ApJS, 246, 34
Phan, T. D., Gosling, J. T., Paschmann, G., et al. 2010, ApJ, 719, L199
Poletto, G., Vaiana, G. S., Zombeck, M. V., Krieger, A. S., & Timothy, A. F. 1975, Sol. Phys., 44, 83
Polito, V., Reep, J. W., Reeves, K. K., et al. 2016, ApJ, 816, 89
Pontin, D. 2011, Advances in Space Research, 47, 1508
Priest, E., & Forbes, T. 2000, Magnetic Reconnection, Springer-Verlag, 612pp
Priest, E. R. 1984, Solar magneto-hydrodynamics, Springer-Verlag,
Pritchett, P. L. 2008, Physics of Plasmas, 15, 102105
Pritchett, P. L., & Coroniti, F. V. 2004, JGR, 109, A01220
Pritchett, P. L. 2006, JGR, 111, A10212
Radziszewski, K., Rudawy, P., & Phillips, K. J. H. 2011, A&A, 535, A123
Romano, P., Elmhamdi, A., Falco, M., et al. 2018, ApJ, 852, L10
Rouillard, A. P., Lavraud, B., Davies, J. A., et al. 2010, JGR, 115, A04104
Roux, J. A. L., Webb, G. M., Khabarova, O. V., Zhao, L.-L., & Adhikari, L. 2019, ApJ, 887, 77
Ripperda, B., Porth, O., Xia, C., & Keppens, R. 2017, MNRAS, 471, 3465
Sauvaud, J. A., Larson, D., Aoustin, C., et al. 2008, Space Sci. Rev., 136, 227
Sharykin, I. N. & Kosovichev, A. G. 2018, ApJ, 864, 86
Shay, M. A., Drake, J. F., Denton, R. E., & Biskamp, D. 1998, JGR., 103, 9165
Shelyag, S., Zharkov, S., Fedun, V., Erdélyi, R., & Thompson, M. J. 2009, A&A, 501, 735
Shmeleva, O. P. & Syrovatskii, S. I. 1973, Sol. Phys., 33, 341
Sironi, L., & Spitkovsky, A. 2014, ApJ, 783, L21
Siversky, T. V., & Zharkova, V. V. 2009, Journal of Plasma Physics, 75, 619
Somov, B. V., ed. 2000, Astrophysics and Space Science Library, Vol. 251, Cosmic Plasma Physics
Somov, B. V., Spektor, A. R., & Syrovatskii, S. I. 1981, Sol. Phys., 73, 145
Štverák, Š., Maksimovic, M., Trávníček, P. M., et al. 2009, JGR, 114, A05104
Syrovatskii, S. I. & Shmeleva, O. P. 1972, Soviet Astronomy, 16, 273
Takasao, S., Asai, A., Isobe, H., & Shibata, K. 2012, ApJ, 745, L6
Verboncoeur, J. P., Langdon, A. B., & Gladd, N. T. 1995, Computer Physics Communications, 87, 199
Vilmer, N., MacKinnon, A. L., & Hurford, G. J. 2011, Space Sci. Rev., 159, 167
Vocks, C., Salem, C., Lin, R. P., & Mann, G. 2005, ApJ, 627, 540.
Wan, W., & Lapenta, G. 2008, Phys. Rev. Lett., 100, 035004
Wang, H., Lu, Q., Huang, C., & Wang, S. 2016a, ApJ, 821, 84
Wang, R., Lu, Q., Nakamura, R., et al. 2016b, Nature Physics, 12, 263
Wang, S., Wang, R., Yao, S. T., et al. 2019, JGR, 124, 1753.
Werner, G. R., Uzdensky, D. A., Begelman, M. C., Cerutti, B., & Nalewajko, K. 2018, MNRAS, 4840
Wuelser, J.-P. & Marti, H. 1989, ApJ, 341, 1088
Yao, S. T., Shi, Q. Q., Liu, J., et al. 2018, Journal of Geophysical Research: Space Physics, 123, 5561.
Xia, Q., & Zharkova, V. 2018, A&A, 620, A121
Xia, Q., & Zharkova, V. 2020, A&A, 635, A116
Xia, Q., & Zharkova, V. 2021, JGR, subm
Xia Q., Dahlin J., Zharkova V. and Antiochos,S. 2020, ApJ, 894, N2, 89
Xu, X., Wei, F., & Feng, X. 2011, JGR, 116, JA016159
Zank, G. P., ed. 2014, Lecture Notes in Physics, Berlin Springer Verlag, Vol. 877, Transport Processes in Space Physics and Astrophysics
Zank, G. P., le Roux, J. A., Webb, G. M., Dosch, A., & Khabarova, O. 2014, ApJ, 797, 28
Zank, G. P., Hunana, P., Mostafavi, P., et al. 2015, ApJ, 814, 137
Zarro, D. M., Canfield, R. C., Metcalf, T. R., & Strong, K. T. 1988, ApJ, 324, 582
Zeiler, A., Biskamp, D., Drake, J. F., et al. 2002, JGR 107, 1230
Zenitani, S., & Hoshino, M. 2001, ApJ, 562, L63
Zenitani, S., & Hoshino, M. 2007, ApJ, 670, 702
—. 2008, ApJ, 677, 530
Zhang, Q., Drake, J. F., & Swisdak, M. 2019, Physics of Plasmas, 26, 072115
Zhang, S., Du, A. M., Feng, X., et al. 2014, Sol. Phys., 289, 1607
Zhao, J. & Chen, R. 2018, ApJ, 860, L29
Zharkov, S. 2013, Monthly Notices of the Royal Astronomical Society, 431, 3414
Zharkov, S., Green, L., Matthews, S., & Zharkova, V. 2011b, ApJ, 741, L35
Zharkov, S., Matthews, S., Zharkova, V., et al. 2020, A&A, 639, A78, Paper 1

DISTRIBUTION A: Distribution approved for public release. Distribution unlimited

Zharkov, S., Zharkova, V. V., & Matthews, S. A. 2011a, ApJ, 739, 70
Zharkova, V. V. 2008, Sol. Phys., 251, 641
Zharkova, V. V., & Agapitov, O. V. 2009, Journal of Plasma Physics, 75, 159
Zharkova, V. V., & Gordovskyy, M. 2004, ApJ, 604, 884
—. 2005, MNRAS, 356, 1107
Zharkova, V. V. & Gordovskyy, M. 2006, ApJ, 651, 553
Zharkova, V. V., & Khabarova, O. V. 2012, ApJ, 752, 35
Zharkova, V., & Khabarova, O. 2015, Annales Geophysicae, 33, 457
Zharkova, V. & Kobylinskii, V. 1993, Sol. Phys., 143, 259
Zharkova, V. V. and Xia, Q. , 2021a, A&A, in press
Zharkova, V. V. and Xia, Q. , 2021b, Frontiers, subm
Zharkova, V. & Zharkov, S. 2007, ApJ, 664, 573
Zharkova, V. & Zharkov, S. 2015, Sol. Phys., 290, 3163
Zharkova, V. V., Arzner, K., Benz, A. O., et al. 2011, Space Sci. Rev., 159, 357
Zharkova V., Zharkov, S., Druett, M, Matthews, S., et al. 2020, A&A, 639, A79, Paper 2
Zhdankin, V., Uzdensky, D. A., Werner, G. R., & Begelman, M. C. 2019, Phys. Rev. Lett., 122, 055101
Zhong, J. Y., Lin, J., Li, Y. T., et al. 2016, ApJ Supplement Series, 225, 30
Zong, Q.-G., Fritz, T. A., Pu, Z. Y., et al. 2004, Geophys. Res. Lett., 31, L18803

DISTRIBUTION A: Distribution approved for public release. Distribution unlimited

Dissemination of the results

The project results were published in 8 peer-reviewed papers in the leading scientific journals and in many conference proceedings.

The results were disseminated in the following seminars and meetings:

1. Annual International Astrophysics Conference, 2017 (Tampa, US), 2018 (Santa Fe, US) (2 oral talks)
2. UK-Ukraine Conference in ST plasma physics, September 2017 – 1 invited, 1 oral, 1 poster
3. ESPM, Hvar, October 2017 – 2 oral talks
4. NASA Goddard Space Flight Centre, 2018: “Particle acceleration in reconnecting current sheets with a single or multiple X-nullpoints” - invited talk
5. COSPAR 2018 – 4 talks: 3 orals, 1 poster
6. Workshop “Particle acceleration and Transport: from the Sun to Extragalactic Sources”, Italy, November 2018: “Particle acceleration in reconnecting current sheets with multiple magnetic islands of different topology” Oral talk by Q. Xia and Zharkova
7. The IAU Symposium Space weather of the heliosphere: processes and forecast’, Exeter, UK, June 2018, 2 oral talks
8. EGU2018 – 2 talks, 1 oral, 1 poster
9. NAM 2018 – 2 orals, 2 posters
10. EGU 2019, 2 orals, 1 poster
11. EGU 2020 – 1 invited, 2 orals and one poster talks at three different sessions
12. NAM 2019 – 3 orals
13. UK-Ukraine conference on solar-terrestrial plasmas, September 2019, Kiev, Ukraine – 1 invited, 1 oral
14. AGU2019 – 1 oral, 2 posters
15. AGU 2020 – 2 posters:
16. COSPAR 21 – 5 talks: 3 orals, 2 posters
17. EGU2021 – 2 orals

DISTRIBUTION A: Distribution approved for public release. Distribution unlimited

List of figures

Figure 1. The plasma inflow (green arrows) and outflow (black arrows) directions (left) and polarisation electric field (PEF) (right) in a magnetic islands chain 13
Figure 2. The trajectories of selected electrons (`E1', `E2'), and protons (`P1', and `P2') in different locations of current sheets 21
Figure 3. The test particle orbits (left column) and energy gains (right column) versus z-coordinate (in blue lines) obtained during the same running simulation time, $\Delta t = 8 \times 10^{-5}$ s 22
Figure 4. The energy spectra of electrons accelerated during t = 8×10^{-5} s in the coalescent islands 24
Figure 5. Particle acceleration in a breakout CME 25
Figure 6. The density, energy (in eV), velocity and PEF distributions of electrons and protons 27
Figure 7. The scheme of coalescent magnetic islands and the plasma flow direction 28
Figure 8. The density and energy distributions of particles in the coalescent magnetic islands at t = 560 Ω^{-1} 29
Figure 9. The density and energy distributions of particles in the coalescent magnetic islands at a later time t = 1120 Ω^{-1} 30
Figure 10. The polarization electric field E_x from the simulations previously presented in Fig.8 31
Figure 11. The density (top panel) and energy (bottom panel) distributions of particles in the coalescent magnetic islands 31
Figure 12. The density (top) and energy (bottom) distributions of particles in the coalescent magnetic islands at t = 560 Ω^{-1} with k = 0.015625. 31
Figure 13. The energy distribution of particles in squashed magnetic islands at t = 560 Ω^{-1} 32
Figure 14. The energy spectra of electrons in the simulations 33
Figure 15. The changes of electric and magnetic fields in the simulation ($n_0 = 10^{10}$ m^{-3}) 34
Figure 16. Power spectra of the normalised electric ($B_0^2V_A^2$) and magnetic fields (by B^2) 35
Figure 17. Phase-space distribution functions of the (b) ions and (c) electrons at difference locations at t = $36\Omega^{-1}$ 36
Figure 18. Local wavelet power spectrum of B_x using Morlet wavelet 37
Figure 19. The spectra of different E and B components at selected points as functions of the Frequency 38
Figure 20. The V_z vs x distributions in phase space and pitch-angle distributions for different B_y/B_0 40
Figure 21. The key solar wind parameters observed by different spacecraft during the passage of the SIR interrupted by the swirl on 2007 May 28–31 42
Figure 22. Electron PADs at different energies, the IMF, and the ambient density in the region filled with MIs of variable sizes as observed by the WIND spacecraft on 2007 May 29 43
Figure 23. Observations of particle parameters similar to Figure 22, but for STEREO A (a) and STEREO B (b) 45
Figure 24. Simulations of acceleration of solar wind electrons to suprathermal energies at the 3D RCS 46
Figure 25. PADs observed when a hypothetical spacecraft crosses two coalescent Mis 47
Figure 26. PSP observations: The electron PADs averaged over 253.3 − 934.2, 55 − 164.6, and 9.7 − 44.3 channels from top to bottom 49
Figure 27. Electron PADs observed when a hypothetical spacecraft crosses the RCS with a single X-nullpoint 50
Figure 28. PADs observed by a virtual spacecraft in the simulation starting with a strong guiding field (b_g = 1) at t = $33\Omega_i$ 50
Figure 29. Left: The AIA 94 Å images at 22:10 UT and magnetograms with an s-shaped sigmoid and flux rope prior to flare onset 54
Figure 30. *L*ight curves of RHESSI 100300 keV HXR (*HXR*), GOES (1.08.0 Å) SXR (*SXR*), integrated HMI LOS magnetogram (*LOS B*), WL continuum (*WL*) and egression power (*EGR*) 55

DISTRIBUTION A: Distribution approved for public release. Distribution unlimited

Figure 31. Sunquake of flare 6 September 2011. Directional egression and time-distance Diagram 57
Figure 32. Magnetic flux ropes formed during the X2.2 flare just prior to the 9.3 flare derived from NLFFF magnetic field reconstruction 58
Figure 33. The light curves of the X9.3 flare 59
Figure 34. HMI white light image marked with the egression maps of the seismic sources 1-4 (left) and directivity maps of seismic sources 1-3 (right) 59
Figure 35. Time–distance diagram for the seismic sources SQ2 (left) and SQ1 (right) 61
Figure 36. Flaring event 1 (>11:55 UT): Series of EIS spectrograms in the Fe XXIII 263.76 Å line taken during the onset phase of the X9.3 flare on 6 September 2017 62
Figure 37. H-alpha line observations of flare 6 September 2017 64
Figure 38. White light emission of flare 6 September 2017 65
Figure 39. Hydrodynamic models of flaring atmospheres 68
Figure 40. Velocity versus linear depth profiles of the simulated hydrodynamic shocks in the seismic event 2 of flare 6 September 2017 (left column) and sunquake of 6 September 2011 (right column) 70
Figure 41. The observed Hα-line profiles in kernels 1-3 overplotted on the Hα line profiles simulated with HYDRO2GEN code 73
Figure 42. Simulated variations of the contribution functions of Paschen continuum (white light emission) derived from a radiative hydrodynamic model 74
Figure 43. The individual acoustic rays travelling to the bottom of the plot generated in the interior by a moving supersonic source with average speed of v = 175 km s^{-1} 76
Figure 44. The individual acoustic rays generated in the interior by a moving supersonic source with average speed of v = 100 km s^{-1} depositing a momentum below the photosphere under +30 $^{\circ}$ angle from the local vertical 76

List of tables

Table 1 – Comparison of hydrogen non-thermal ionisation and excitation rates in flaring atmospheres

DISTRIBUTION A: Distribution approved for public release. Distribution unlimited